Vol. 299, No. 3, January 10, 1995
Completing Volume 299

ISSN 0003-2670

Special Issue
LASER SPECTROSCOPY
(Guest Editor: T. Sawada)

ANALYTICA CHIMICA ACTA

An international journal devoted to all branches of analytical chemistry

ELSEVIER

ANALYTICA CHIMICA ACTA

Scope. *Analytica Chimica Acta* publishes original papers, rapid publication letters and reviews dealing with every aspect of modern analytical chemistry. Reviews are normally written by invitation of the editors, who welcome suggestions for subjects. Letters can be published within **four months** of submission. For information on the Letters section, see inside back cover.

Submission of Papers

Americas

Prof. Harry L. Pardue
Department of Chemistry
1393 BRWN Bldg, Purdue University
West Lafayette, IN 47907–1393
USA

Tel:(+1-317) 494 5320
Fax:(+1-317) 496 1200

Computer Techniques

Prof. J.T. Clerc
Universität Bern
Pharmazeutisches Institut
Baltzerstrasse 5, CH-3012 Bern
Switzerland

Tel:(+41-31) 6314191
Fax:(+41-31) 6314198

Prof. Sarah C. Rutan
Department of Chemistry
Virginia Commonwealth University
P.O. Box 2006
Richmond, VA 23284-2006
USA
Tel:(+1-804) 367 7517
Fax:(+1-804) 367 8599

Other Papers

Prof. Alan Townshend
Department of Chemistry
The University
Hull HU6 7RX
Great Britain

Tel:(+44-482) 465027
Fax:(+44-482) 466410

Prof. Willem E. van der Linden
Laboratory for Chemical Analysis
Department of Chemical Technology
Twente University of Technology
P.O. Box 217, 7500 AE Enschede
The Netherlands
Tel:(+31-53) 892629
Fax:(+31-53) 356024

Prof. Paul Worsfold
Dept. of Environmental Sciences
University of Plymouth
Plymouth PL4 8AA
Great Britain

Tel:(+44-752) 233006
Fax:(+44-752) 233009

Submission of an article is understood to imply that the article is original and unpublished and is not being considered for publication elsewhere. *Anal. Chim. Acta* accepts papers in English only. There are no page charges. Manuscripts should conform in layout and style to the papers published in this issue. See inside back cover for "Information for Authors".

Publication. *Analytica Chimica Acta* appears in 18 volumes in 1995 (Vols. 297–314). *Vibrational Spectroscopy* appears in 2 volumes in 1995 (Vols. 8 and 9). Subscriptions are accepted on a prepaid basis only, unless different terms have been previously agreed upon. It is possible to order a combined subscription (*Anal. Chim. Acta* **and** *Vib. Spectrosc.*).
Our p.p.h. (postage, packing and handling) charge includes surface delivery of all issues, except to subscribers in the U.S.A., Canada, Australia, New Zealand, China, India, Israel, South Africa, Malaysia, Thailand, Singapore, South Korea, Taiwan, Pakistan, Hong Kong, Brazil, Argentina and Mexico, who receive all issues by air delivery (S.A.L.–Surface Air Lifted) at no extra cost. For Japan, air delivery requires 25% additional charge of the normal postage and handling charge; for all other countries airmail and S.A.L. charges are available upon request.

Subscription orders. Subscription prices are available upon request from the publisher. Subscription orders can be entered only by calendar year and should be sent to: Elsevier Science B.V., Journals Department, P.O. Box 211, 1000 AE Amsterdam, The Netherlands. Tel: (+31-20) 4853 642, Telex: 18582, Telefax: (+31-20) 4853 598, to which requests for sample copies can also be sent. Claims for issues not received should be made within six months of publication of the issues. If not they cannot be honoured free of charge. Readers in the U.S.A. and Canada can contact the following address: Elsevier Science Inc., Journal Information Center, 655 Avenue of the Americas, New York, NY 10010, U.S.A. Tel: (+1-212) 633 3750, Telefax: (+1-212) 633 3990, for further information, or a free sample copy of this or any other Elsevier Science journal.
Advertisements. Advertisement rates are available from the publisher on request.

US mailing notice – Analytica Chimica Acta (ISSN 0003-2670) is published 3 times a month (total 54 issues) by Elsevier Science B.V. (Molenwerf 1, Postbus 211, 1000 AE Amsterdam). Annual subscription price in the USA US$ 3677.75 (valid in North, Central and South America), including air speed delivery. Second class postage paid at Jamaica, NY 11431. *USA Postmasters*: Send address changes to Anal. Chim. Acta, Publications Expediting, Inc., 200 Meacham Av., Elmont, NY 11003. Airfreight and mailing in the USA by Publication Expediting.

ANALYTICA CHIMICA ACTA

An international journal devoted to all branches of analytical chemistry

(Full texts are incorporated in CJELSEVIER, a file in the Chemical Journals Online database available on STN International; Abstracted, indexed in: Aluminum Abstracts; Anal. Abstr.; Biol. Abstr.; BIOSIS; Chem. Abstr.; Curr. Contents Phys. Chem. Earth Sci.; Engineered Materials Abstracts; Excerpta Medica; Index Med.; Life Sci.; Mass Spectrom. Bull.; Material Business Alerts; Metals Abstracts; Sci. Citation Index)

VOL. 299 NO. 3 CONTENTS JANUARY 10, 1995

Special issue on Laser Spectroscopy

SPECIAL ISSUE

LASER SPECTROSCOPY

ELSEVIER

Analytica Chimica Acta 299 (1995) 299

ANALYTICA
CHIMICA
ACTA

PREFACE

In the past few years much progress has been made in the use of lasers. In many fields such as chemistry, physics, and medicine, lasers have played important roles in revolutionary innovations. Many believe that lasers are indispensable tools for science.

In analytical chemistry, lasers have enabled high-sensitivity determinations, high-resolution spectroscopy, and extreme diagnostics. Concerning the analytical applications of lasers, some researchers still think that lasers cost too much and their maintenance is troublesome. They therefore believe it will need more time for spectrometers (except Raman spectrometers) to be commercially available. Of course, it is agreed that a laser has such problems, but recent great progress in advanced materials such as semiconductor devices has stimulated the development of innovative optical evaluation techniques. Particularly the use of laser spectroscopy for these problems is now being exploited.

This special issue has been planned from the above-mentioned scientific view point. I think this plan is quite timely. I hope that many analytical chemists working in other fields are interested by the articles in this issue.

Finally I would like to thank the many contributors from several countries who have helped to make this issue successful.

Tsuguo Sawada
University of Tokyo
Japan

SSDI 0003-2670(94)00543-5

ELSEVIER

Analytica Chimica Acta 299 (1995) 301–308

ANALYTICA CHIMICA ACTA

Pump-probe laser photolytic fragmentation fluorescence spectrometry of methyl vinyl ketone, methacrolein and crotonaldehyde

Bobby J. Stanton, E.T. Monroe, E.L. Wehry *

Department of Chemistry, University of Tennessee, Knoxville, TN 37996-1600, USA

Received 5 January 1994; revised manuscript received 9 March 1994

Abstract

The two-laser "pump-probe" photolytic fragmentation fluorescence spectrometry of methyl vinyl ketone, methacrolein and crotonaldehyde is described. Probe laser induced C_2 ($C^1\Pi_g \rightarrow A^1\Pi_u$, Deslandres–d'Azambuja band system) fluorescence is detected. The relative C_2 fluorescence intensity and spectral patterns exhibited by each C_4H_6O isomer are dependent upon the probe laser wavelength employed. The dependence of the fragment fluorescence signal intensity on the probe laser fluence implies that the "probe" laser induces photofragmentation of intermediate specie(s) produced by the "photolysis" laser. The vinyl radical (C_2H_3) is believed to be an important intermediate produced from the C_4H_6O isomers by the photolysis laser, which can subsequently be converted to C_2 via the absorption of probe laser photons.

Keywords: Fluorimetry; Photolytic fragmentation; Probe lasers

1. Introduction

The principal shortcoming of molecular fluorescence spectrometry is the fact that most compounds do not exhibit sufficiently high fluorescence quantum efficiencies to be detected under analytically realistic conditions [1]. The analytical applicability of molecular fluorescence spectrometry can be extended to virtually any compound by converting that compound to small emissive fragments via photolysis, using intense laser radiation [2–10]. This approach has been termed laser photolytic fragmentation fluorescence spectrometry (LP-FFS). Examples of emissive fragments which can be formed in this manner are NH, OH, CN, CH, CCl, C_2, C, H and metal atoms. Most of these luminescent molecular fragments formed are neutrals; thus, the information obtained in LP-FFS is complementary to that obtained in mass spectrometry.

LP-FFS experiments can be conducted using either one or two lasers [6,7,10]. In a one-laser experiment, the photolysis laser (usually operating at 193 nm) must produce fragments in emissive excited electronic states. If the photofragmentation process produces fragments primarily in the ground electronic state, or in dark (non-emissive) excited states, the sensitivity of one-laser LP-FFS will be relatively low. Moreover, discrimination of individual analytes in the presence of structurally similar compounds is virtually impossible via one-laser LP-FFS [7,8].

Alternatively, one may employ a second, probe, laser to induce fluorescence from fragments formed in the ground or non-emissive excited electronic states by the

* Corresponding author.

Elsevier Science B.V.
SSDI 0003-2670(94)00311-4

photolysis laser. The probe laser may also conceivably induce photofragmentation of highly excited parent molecules and/or relatively large intermediate fragments formed by 193 nm photolysis of the parent compounds. In pump-probe LP-FFS, selective detection is achieved via 193 nm photolysis of all (or nearly all) of the constituents in a multicomponent sample, then relying on the probe laser to produce differences in the two-laser fragment fluorescence spectral features, as well as observing differences for the dependence of the fluorescence signal of a particular fragment (such as C_2) upon the photolysis or probe laser fluence (=energy/unit cross-sectional area) for the various sample components.

We have recently reported the selective detection of structurally similar organic compounds via pump-probe LP-FFS of acrolein and propargyl alcohol [7], C_4H_5N nitriles [8], alkene isomers [11], and allylamine and its derivatives [8], for which the possibility of selective detection of the compounds was partially attributed to photolytic processes induced by the probe laser. In the present work, pump-probe LP-FFS was applied to three C_4H_6O isomers: methacrolein ($H_2C=C(CH_3)CHO$), methyl vinyl ketone ($H_2C=CHCOCH_3$) and crotonaldehyde ($CH_3CH=CHCHO$).

2. Experimental

Fig. 1 is a schematic diagram of the apparatus used in this work. Radiation from a Questek 2210 ArF excimer laser operating at 193 nm (10 Hz repetition rate, 10 ns pulse duration, 5–60 mJ/pulse energy) is focused by a 15.2-cm plano-convex lens into a vacuum chamber of ca. 2.5 l. The vacuum chamber pressure is typically 10^{-7} torr in the absence of sample. Probe laser radiation (derived from a Questek 2210 XeCl excimer-pumped Lambda Physik FL-2000 dye laser) is counterpropagated 180° relative to the photolysis laser. The probe laser is triggered at a 10 Hz repetition rate and the pulse duration is 10 ns. The photolysis and probe laser cross-sectional areas are 1 and 7 mm^2, respectively at the point of overlap. The temporal delay of the probe laser pulses relative to the photolysis laser pulses is 350 ns.

Each sample is inserted as a vapor into a stagnation reservoir via a heated transfer line, where it is subsequently mixed with argon. The typical reservoir pres-

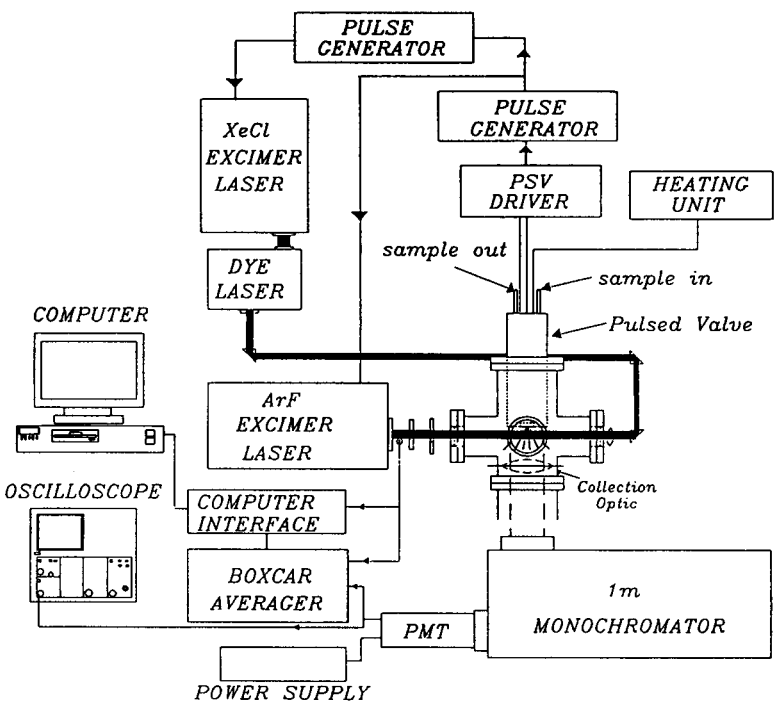

Fig. 1. Schematic diagram depicting the instrumentation used in pump-probe LP-FFS. PSV = pulsed supersonic valve.

sure is 400 torr; the argon to sample mole ratio is generally 10:1. The sample–argon mixture is expanded through an 0.5-mm orifice via a R.M. Jordan (C-211SS) pulsed supersonic valve into the vacuum chamber. The pulsed valve is triggered at a 10 Hz repetition rate and produces 200 μs gas pulses. The pulsed valve power supply triggers the pulsed valve, as well as the firing of the photolysis and probe lasers.

Fluorescence is collected at 90° relative to the laser beam paths and 90° relative to the pulsed molecular beam. The fluorescence is collimated with a 15.2-cm cylindrical lens onto the entrance slit of a 1-m Jobin/Yvon (HR-100) grating monochromator. The spectral bandpass of the monochromator is typically 0.1 nm. The fluorescence is detected with a Burle 8850 photomultiplier tube and the signal is processed via a Stanford Research System SR-250 boxcar integrator/averager. Data collection is managed by an IBM PS/2 50Z laboratory computer.

Methyl vinyl ketone, crotonaldehyde and methacrolein were used as received from Aldrich. Each sample was subjected to a liquid nitrogen freeze–thaw cycle prior to being introduced into the pulsed valve reservoir.

3. Results and discussion

Fig. 2 depicts one-laser LP-FFS spectra for methyl vinyl ketone, crotonaldehyde and methacrolein. The

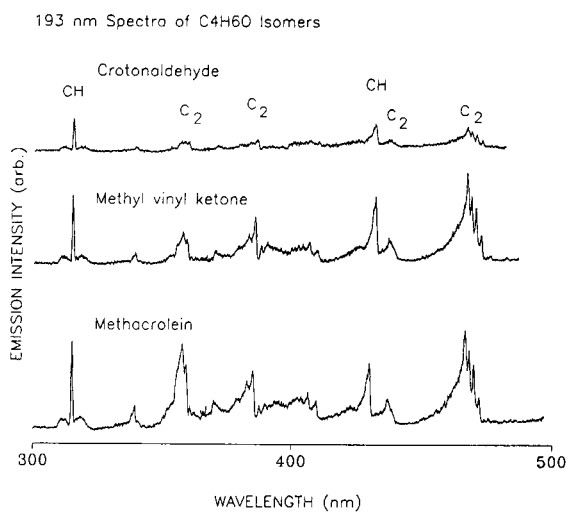

Fig. 2. One-laser LP-FFS spectra of methacrolein, methyl vinyl ketone and crotonaldehyde produced by 193 nm photolysis.

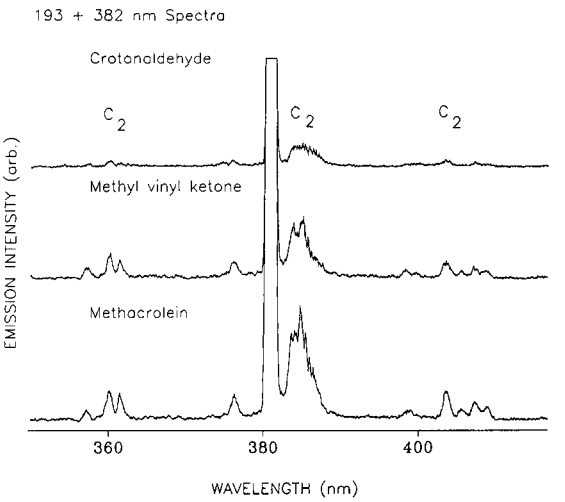

Fig. 3. Pump-probe LP-FFS spectra of methacrolein, methyl vinyl ketone and crotonaldehyde using 382 nm as the probe laser wavelength. The intense spectral feature at 382 nm is due to scattered probe laser radiation.

emissive fragments identified were CH and C_2. C_2 emission at ≤ 410 nm is from the Deslandres–d'Azambuja ($C^1\Pi_g \rightarrow A^1\Pi_u$) band system, which corresponds to fluorescence from the third spin-allowed (singlet) excited state of C_2 ($C^1\Pi_g$) to the first spin-allowed excited electronic state ($A^1\Pi_u$) [8]. C_2 emission at ≥ 434 nm is from the Swan ($d^3\Pi_g \rightarrow a^3\Pi_u$) band system. Although small differences in the relative fragment fluorescence intensities were noted (i.e., the CH/C_2 intensity ratio was greater for crotonaldehyde than for methacrolein or methyl vinyl ketone at 431 and 470 nm, respectively), the one-laser spectral patterns observed for the isomers were sufficiently similar that discrimination of one isomer in the presence of the others is difficult, at best.

Fig. 3 shows 193+382 nm pump-probe LP-FFS spectra for the C_4H_6O isomers. The 382 nm probe laser wavelength excited the $C(\nu'=1) \leftarrow A(\nu''=1)$ absorption transition in C_2 and the probe laser pulse energy was 2.0 mJ/pulse. Three C_2 emission bands were detected for the isomers at 358–366, 378–386 and 403–412 nm which were assigned to vibronic transitions within the C_2 ($C \rightarrow A$) Deslandres–d'Azambuja band system. Anti-Stokes fluorescence (energy of emission greater than the energy of excitation) was detected in the 358–366 nm region, which was indicative of probe laser excitation of hot fragments (fragments residing in a vibrationally excited level of the ground electronic

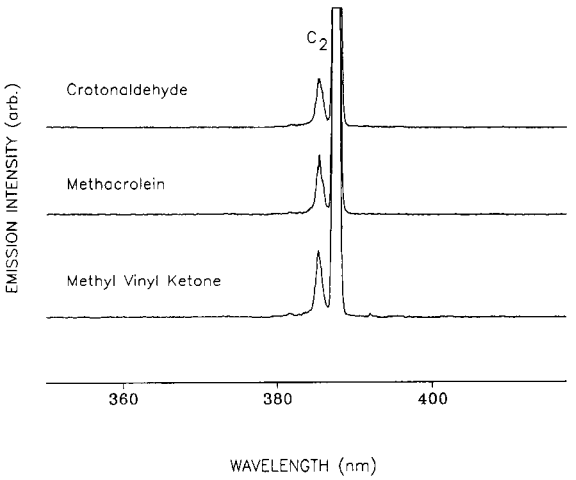

Fig. 4. Pump-probe LP-FFS spectra of methacrolein, methyl vinyl ketone and crotonaldehyde using 387 nm as the probe laser wavelength. The intense spectral feature at 387 nm is due to scattered probe laser radiation.

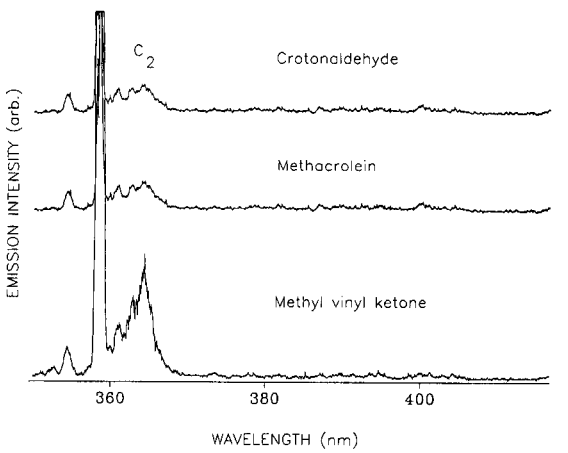

Fig. 5. Pump-probe LP-FFS spectra of methacrolein, methyl vinyl ketone and crotonaldehyde using 358.5 nm as the probe laser wavelength. The intense spectral feature at 358.5 nm is due to scattered probe laser radiation.

state or in a low-lying excited electronic state). The anti-Stokes fluorescence observed in the pump-probe LP-FFS spectrum of crotonaldehyde was weak, as was the fluorescence in the 403–412 nm region. The spectral patterns exhibited by methyl vinyl ketone and methacrolein in the 193+382 nm spectra were virtually indistinguishable. However, anti-Stokes fluorescence in the 355–366 nm region was virtually undetectable for crotonaldehyde, as was C_2 fluorescence at >400 nm.

Fig. 4 depicts 193+387 nm pump-probe LP-FFS spectra for the isomers. The 387 nm probe laser wavelength excited the $C(\nu'=0) \leftarrow A(\nu''=0)$ absorption transition in C_2 and the probe laser energy was 2.3 mJ/pulse. C_2 anti-Stokes fluorescence was detected at 385 nm for each isomer which corresponded to the $C \rightarrow A$ (0,0) transition in C_2. Fig. 5 shows 193+358.5 nm pump-probe LP-FFS spectra for the isomers. The 358.5 nm probe laser wavelength excited the $C(\nu'=1) \leftarrow A(\nu''=2)$ absorption transition in C_2 and the probe laser pulse energy was 2.0 mJ/pulse. C_2 anti-Stokes fluorescence was detected at 355 nm for each isomer. Broad band C_2 fluorescence centered at 364 nm was also detected for the isomers. The pump-probe LP-FFS spectral features observed for methacrolein, methyl vinyl ketone and crotonaldehyde when 382, 387 and 358.5 nm probe laser radiation was used were sufficiently similar that discrimination of one isomer in the presence of the others is difficult.

Significant differences in the C_2 fragment fluorescence signal intensities, however, were noted for the isomeric compounds when the various probe laser wavelengths were used (see Table 1). For example, when 382 nm was used as the probe laser wavelength, methacrolein produced the most intense C_2 fluorescence at 385 nm for either isomer studied. When 387 or 358.5 nm probe laser radiation was employed, methyl vinyl ketone produced the most intense C_2 flu-

Table 1
Relative C_2 fragment fluorescence intensities for C_4H_6O isomers

Probe λ, nm	Fluorescence transition	Fluorescence λ, nm	Relative intensity [a]
382	$C(\nu'=0) \rightarrow A(\nu''=0)$	385	1.0:2.6:3.4
382	$C(\nu'=1) \rightarrow A(\nu''=0)$	360.5	1.0:3.4:3.4
387	$C(\nu'=0) \rightarrow A(\nu''=0)$	385	1.0:1.2:1.1
358.5	$C \rightarrow A$ [b]	364	1.0:4.9:1.2

[a] Relative fragment fluorescence intensities, at the indicated wavelength, for crotonaldehyde (normalized to 1):methyl vinyl ketone:methacrolein.
[b] Overlapping vibronic transitions within this region.

orescence signal. For any of the three probe laser wavelengths, crotonaldehyde produced the least intense C_2 fluorescence at any emission wavelength monitored. Thus, the spectral patterns and relative C_2 fragment fluorescence signal intensities observed were highly dependent upon the probe laser wavelength used.

The role of the probe laser in two-laser multiphoton ultraviolet photolytic processes of organic compounds has thus far received little attention. The general assumption has been that the probe laser detected the results of photolysis induced by the photolysis laser, but did not significantly perturb product or electronic state distributions produced by the photolysis laser. One useful measure of the complexity of a photolytic process is the fluence dependence for the process. The fluence dependence information is obtained in a so-called power-dependence study, in which one monitors the change in fluorescence intensity as the probe laser energy is varied, while maintaining constant photolysis laser pulse energy. The slope of a log(fluorescence signal) versus log(probe laser pulse energy) plot identifies the fluence dependence. This information is useful because the fluence dependence is an indication of the *minimum* number of photons that must be absorbed to generate the fragment fluorescence in question. If the dependence of the fluorescence signal on the probe laser fluence is linear (i.e., first-order), then it is presumed that the only function of the probe laser is to promote fragments, formed by the photolysis laser, to emissive excited states. However, if the fluence dependence is non-linear (greater than first-order), it can be concluded that the role of the probe laser is more complex.

We have previously reported unanticipated non-linear probe laser fluence dependence data for compounds such as acrolein, methacrylonitrile, allylamine, and 1-, 2- and 4-octene [7,8,11]. These data suggested that the probe laser altered the C_2 electronic state distributions generated by the photolysis laser and/or induced photofragmentation of highly excited parent molecules and/or relatively large intermediate fragments formed by the 193 nm photolysis of the parent compounds.

In the present work, an effort was undertaken to improve our understanding of the role that the probe laser plays in multiphoton photolytic phenomena subsequent to 193 nm photolysis. Methyl vinyl ketone and acrolein (a compound that is structurally similar to methacrolein) were selected for study because there have been numerous reports on their UV photochemistry in the literature, and their UV photolysis mechanisms appear to be reasonably well established.

It appears (based on reports in the literature) that 193 nm photolysis of methyl vinyl ketone and acrolein (at relatively low photolysis laser pulse energies, ≤ 10 mJ/pulse) generates two primary fragments (C_2H_3 and C_2H_4) capable of serving as major sources of C_2 [12–14]:

$$H_2C{=}CHCOCH_3 + h\nu \rightarrow C_2H_3 + HCO \quad (1)$$

$$H_2C{=}CHCHO + h\nu \rightarrow C_2H_4 + CO \quad (2)$$

$$\text{or} \rightarrow C_2H_3 + HCO \quad (3)$$

$$\text{or} \rightarrow H_2C{=}CHCO + H \quad (4)$$

The $H_2C{=}CHCO$ fragment (formed from acrolein with excess internal energy, Reaction 4) is thought to decompose to $C_2H_3 + CO$. Thus, both methyl vinyl ketone and acrolein are thought to produce the vinyl radical (C_2H_3) as a major product of 193 nm photolysis. The vinyl radical absorbs in the 360–490 nm region (all probe laser wavelengths used in this work are in this wavelength range), while C_2H_4 is transparent in the same region [15].

It is postulated in this work that C_2H_3, formed by 193 nm photolysis (≤ 10 mJ/pulse energy) of acrolein and methyl vinyl ketone, may undergo conversion to C_2 via absorption of probe laser photons. To test the feasibility of this hypothesis, methyl vinyl ketone and acrolein were photolyzed with low 193 nm photolysis laser pulse energies (≤ 10 mJ/pulse) to generate C_2H_3 with nearly unit efficiency [16]. It was necessary to employ relatively low 193 nm pulse energies; if higher pulse energies are used, C_2H_3 could be photolyzed further, to C_2, by the tail of the relatively long (10 ns) photolysis laser pulse [12]. The objective of this experiment was to avoid producing detectable quantities of C_2 in the absence of probe laser photons. It was assumed that the subsequent addition of probe laser photons could induce conversion of C_2H_3 (formed by the photolysis laser) to C_2.

Fig. 6 depicts one-laser LP-FFS spectra of methyl vinyl ketone at different 193 nm pulse energies. It was necessary to reduce the photolysis laser pulse energy to 5 mJ/pulse before one-laser C_2 fluorescence was undetectable. When two-laser experiments were carried out (using 5 mJ/pulse at 193 nm), significant C_2

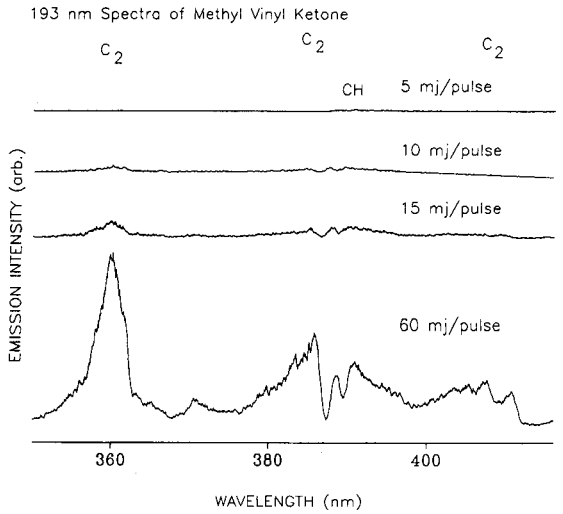

Fig. 6. One-laser LP-FFS spectra of methyl vinyl ketone using 5, 10, 15 and 60 mJ/pulse photolysis laser energies.

($C \rightarrow A$) fluorescence was detected at 385 nm (0,0 transition).

The dependence of the C_2 fluorescence signal (385 nm) on the probe laser fluence (for probe laser wavelengths of 382 or 387 nm) was examined as a function of the photolysis laser pulse energy for methyl vinyl ketone and acrolein. The data compiled in Table 2 demonstrate that, as the photolysis laser pulse energy is decreased, the C_2 fragment probe laser fluence dependence drastically increases. The strongly non-linear probe laser fluence dependence for C_2, when the photolysis laser energy was ≤ 10 mJ/pulse, strongly implies that probe laser photolysis of some intermediate specie(s) formed by the 193 nm photolysis of methyl vinyl ketone and acrolein occurred, leading to the formation of emissive C_2 fragments, and that the relative contribution of probe-laser produced C_2 fluorescence increases as the photolysis laser pulse energy is decreased. Based on the findings of Lessard and Rosenfeld [14], Huber et al. [12] and Fahr et al. [13], the most likely intermediate fragment formed by the photolysis laser was C_2H_3.

The spectral and probe laser fluence dependence data are consistent with the hypothesis that the C_2H_3 radical, formed via 193 nm photolysis of methyl vinyl ketone and acrolein, is converted to C_2 via the absorption of at least two, and probably more, probe laser photons. Of course, the results do not preclude the possibility that the photolysis laser also generates C_2 fragments in the $A^1\Pi_u$ excited electronic state which could be excited by the probe laser to the $C^1\Pi_g$ excited electronic state, with the subsequent production of C_2 ($C \rightarrow A$) fluorescence. However, that scenario necessitates the absorption of at least two 193 nm photons by methyl vinyl ketone and acrolein, a process that must decrease in significance as the photolysis laser fluence decreases; at the lowest photolysis laser pulse energy employed in this work, the photolysis laser fluence is only 5×10^{17} photons/cm^2.

It is important to recall that a laser fluence dependence experiment can only reveal the *minimum* number of photons needed to induce the production of fluorescence from a particular fragment. The actual number of photons needed to induce the fragment fluorescence in question will be greater (perhaps substantially greater) than the observed fluence dependence whenever saturation, or partial saturation, of any of the successive electronic absorption transitions takes place in

Table 2
Dependence of C_2 fluorescence signal at 385 nm on probe laser fluence

Parent	193 nm mJ/pulse	Probe λ, nm	Probe laser fluence dependence [a]	Probe laser fluence [b] (Range 10^{16} photons/cm^2)
Methyl vinyl ketone	60	387	0.34 ± 0.08	2.2–3.6
	10	382	0.69 ± 0.12	0.7–1.8
	10	387	0.56 ± 0.08	2.2–3.6
	5	382	2.13 ± 0.12	0.7–1.8
	5	387	3.47 ± 0.50	2.2–3.6
Acrolein	5	387	1.77 ± 0.18	0.6–1.1

[a] Slope of linear plot of log(fluorescence signal) vs. log(laser pulse energy) ± S.D.
[b] Based upon a 7 mm^2 probe laser beam area.

the "ladder-climbing" process that ultimately leads to formation and excitation of the fragment to an emissive excited state. Non-integral fluence dependencies (such as those observed in this work) are generally considered as diagnostic criteria indicating the importance of saturation effects in multiphoton photolytic processes [16–18]. Thus, as an example (cf. Table 2), all that can be said for acrolein, when 5 mJ photolysis laser pulse energy was used and 387 nm was used as the probe-laser wavelength, is that a minimum of 2 probe-laser photons was required to induce the observed C_2 fluorescence. The actual number of probe-laser photons required to produce the observed fluorescence may well have been 3 or more. Likewise, non-integral fluence dependences of less than unity (cf. Table 2 for examples) indicate only that saturation effects were clearly significant in the experiments in question and that at least one photon was required to produce C_2 fluorescence; again, it is virtually certain that the actual number of probe-laser photons required in these cases was two or greater.

Relative standard deviations for replicate pump-probe LF-FFS measurements carried out under the conditions described herein were in the 3–8% range. This may appear to constitute unexpectedly high precision, in view of the non-linear dependence of the fluorescence signals on the laser fluences, as discussed above. However, it must be noted that, in our apparatus, by far the most important source of imprecision is pulse-to-pulse fluctuation (and drift) in the photolysis laser power. It is frequently observed that the dependence of the observed fragment fluorescence signal on the *photolysis* laser power is smaller in a pump-probe (two-laser) measurement than in a one-laser experiment (wherein one relies on the photolysis laser both to form the fragments and excite fragment fluorescence). Consequently, one often encounters the apparently anomalous result that the more complex measurement (pump-probe) produces significantly higher precision than the experimentally simpler one-laser measurement [10].

4. Conclusions

Selective detection of individual isomers in a mixture is possible via pump-probe LP-FFS based on differences in the observed fragment fluorescence spectral patterns, differences in the relative fragment fluorescence signal intensities and differences for the fragment signal dependences on the photolysis and probe laser fluence dependences. These differences are highly dependent on the probe laser wavelength used. The differences in the spectral features and laser fluence dependences for the C_4H_6O isomers were attributed to alteration, by the probe laser, of the C_2 fragment electronic state distributions and/or photofragmentation by the probe laser of intermediate specie(s). Based on literature data and the results presented in this work, the C_2H_3 radical is the most likely intermediate, produced via 193 nm photolysis of the C_4H_6O isomers, which can be subsequently photolyzed to C_2 via the absorption of probe laser photons. Since most of the compounds studied to date in this laboratory [7,8,11] contain C=C double bonds, the C_2H_3 radical or analogous species (e.g., allyl radical, C_3H_5) may be important intermediates produced by the 193 nm photolysis of many of the parent compounds studied to date.

Acknowledgements

This work was supported by the National Science Foundation under grant CHE-8822722 and the Science Alliance, a State of Tennessee Center of Excellence at the University of Tennessee, Knoxville.

References

[1] J.D. Ingle and S.R. Crouch, Spectrochemical Analysis, Prentice Hall, Englewood Cliffs, NJ, 1988, p. 340.
[2] J.B. Halpern, E.B. Koker and W.M. Jackson, Anal. Chem., 55 (1983) 2000.
[3] M.O. Rodgers, K. Asai and D.D. Davis, Appl. Opt., 19 (1980) 3597.
[4] S.R. Long, R.C. Sausa and A.W. Miziolek, Chem. Phys. Lett., 117 (1985) 505.
[5] T. Papenbrock and F. Stuhl, Atmos. Environ., 25A (1991) 2223.
[6] J.B. Jeffries, G.A. Raiche and L.E. Jusinski, Appl. Phys., B55 (1992) 76.
[7] S.C. Lee, B.J. Stanton and E.L. Wehry, Anal. Chem., 63 (1991) 744.
[8] S.C. Lee, B.J. Stanton, B.A. Eldridge and E.L. Wehry, Anal. Chem., 64 (1992) 268.

[9] R.C. Oldenburg and S.L. Baughcum, Anal. Chem., 58 (1986) 1430.
[10] J. Schendel and E.L. Wehry, Anal. Chem., 60 (1988) 1759.
[11] B.J. Stanton, E.T. Monroe and E.L. Wehry, Appl. Spectrosc., 48 (1994) 616.
[12] B.M. Haas, T.-K. Mitton, P. Felder and J.R. Huber, J. Phys. Chem., 95 (1991) 5149.
[13] A. Fahr, W. Braun and A.H. Laufer, J. Phys. Chem., 97 (1993) 1502.
[14] P.C. Lessard and R.N. Rosenfeld, J. Phys. Chem., 96 (1992) 4615.
[15] H.E. Hunziker, K. Kneppe, A.D. McLean, P. Siegbahn and H.R. Wendt, Can. J. Chem., 61 (1988) 993.
[16] R.C. Sausa, A.J. Alfano and A. Miziolek, Appl. Opt., 26 (1987) 3588.
[17] J.G. Jinkins and E.L. Wehry, Appl. Spectrosc., 43 (1989) 861.
[18] S. Desmukh, J.L. Brum and B. Koplitz, Chem. Phys. Lett., 176 (1991) 198.

ELSEVIER

Analytica Chimica Acta 299 (1995) 309–318

ANALYTICA CHIMICA ACTA

Time-resolved fluorescence and absorption microspectroscopy of a single microparticle

Hiroshi Masuhara [1], Keiji Sasaki[1] *

Microphotoconversion Project [2], ERATO, Research Development Corporation of Japan, 15 Morimoto-cho, Shimogamo, Sakyo-ku, Kyoto 606, Japan

Received 21 April 1994; revised manuscript received 16 June 1994

Abstract

Time-resolved fluorescence and transient absorption spectroscopy systems have been developed for elucidating photophysical and photochemical processes occurring in μm-sized volumes. The fluorescence measurement is based on a confocal fluorescence microscope and single photon timing, which enables the fluorescence dynamics to be observed with both sub-μm three-dimensional space- and ps time resolutions. For transient absorption spectroscopy, excitation and monitoring laser pulses are coaxially and confocally introduced into a microscope. This optical arrangement provides the longitudinal resolution in addition to the lateral resolution. By combining a laser trapping technique we have succeeded in measuring primary photoprocesses of a single manipulated particle in solution. Fluorescence analysis of individual microcapsules in solution gave information on solute concentration distribution between capsules. The viscosity of a single oil droplet dispersed in aqueous solution was estimated by analyzing the T–T annihilation of Zn–tetraphenylporphyrin.

Keywords: Fluorimetry; Lasers; Microparticles; Microspectroscopy; Photoprocesses; Zn–tetraphenylporphyrin

1. Introduction

Laser light has superior properties such as coherency, monochromaticity, focusability, and short pulse, hence its utilization has opened new research areas in chemistry. The first example of such laser chemistry is state-to-state chemistry. This is based on high-resolution spectroscopy due to the monochromaticity of the laser. Reactions can be initiated from particular electronic and vibrational as well as rotational energy levels of reactants and lead to products with specific energy levels. The reaction path can be elucidated in detail for isolated molecules and clusters in the gas phase. Multiphoton absorption, vibrational energy re-distribution, and photodecomposition are fundamental processes frequently studied in laser chemistry. In the second example, laser chemistry has been attained by introducing pulsed lasers. High time-resolution in spectroscopy is being improved to the fs scale, and primary photoprocesses such as electron transfer, proton transfer, energy transfer, isomerization, dissociation, and so forth are studied as an important field called chemistry of ultra-fast phenomena.

Among the superior characteristics of laser light, spatial properties such as focusability and interference have not been utilized in chemistry, since most of chemical systems are homogeneous solutions, gases, solid films, and crystals. Quite recently, fabricated

* Corresponding author.

[1] Permanent address: Department of Applied Physics, Osaka University, Suita, Osaka 565, Japan.

[2] Five-year term project: October 1988–September 1993.

SSDI 0003-2670(94)00324-6

microstructures such as patterned resists and quantum wires, microdroplets, microcapsules, microelectrodes, and micromachined components have received much attention as interesting inhomogeneous chemical systems, in addition to Langmuir–Blodgett films, biological tissues, cells, and so forth. In these systems it is necessary to elucidate physical and chemical properties as a function of the position in three-dimensional space. Thus, focusability and interference properties of laser light become important in chemistry.

Furthermore, by focusing the laser beam onto a small particle under a microscope, it is now possible to manipulate a particle, since radiation force is exerted on the particle. By arranging an optical set up, it is demonstrated to catch, transfer, and fix a single microparticle at a certain position in solution against its Brownian motion; i.e. laser trapping. The particle can be decomposed, evaporated, fused, and fabricated photochemically by focusing an additional UV laser pulse onto the particle. Combining the trapping technique with dynamic microspectroscopy and microelectrochemistry systems, which we have developed separately, various versions of laser trapping methods have been proposed [1]. Spectroscopic and electrochemical analysis, photochemistry, and fabrication of individual particles in solution have been made possible just as in the bulk. Thus, our approach is now considered to open a new aspect of analytical chemistry, which is presented in this article.

2. Time-resolved fluorescence microspectroscopy

The most popular tool for the space-resolved measurement with a μm scale is an optical microscope, which has been widely applied to various sciences and industries, especially to biological studies and recent semiconductor technology. The optical microscope, however, has some difficulties in combining with time-resolved laser spectroscopy. One is the influence of speckle and interference fringes due to the high spatial coherence of laser. Invisibly small dusts and slight distortion of optical systems cause irregular patches and/or periodic intensity distribution. These coherent noises disturb the image formation with laser light, so that the quantitative information on the spatial distribution is lost in the observed image. The other problem concerns longitudinal (depth) resolution. The conventional optical microscopes provide only two-dimensional images. The observed image does not correspond to the structure only on the focal plane, but include all the distribution along the depth direction. Contamination by out-of-focus contributions makes it difficult to accurately analyze the spectroscopic information on the inhomogeneous systems.

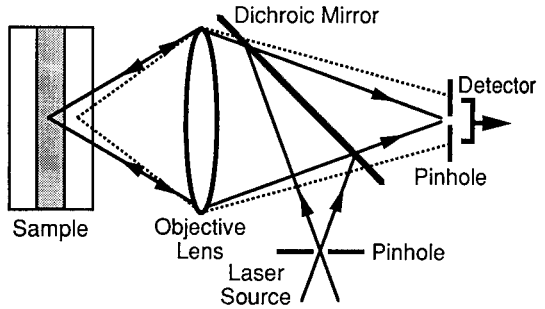

Fig. 1. Optical system of a confocal fluorescence microscope.

These problems can be solved by introducing a confocal microscope which has recently received much attention in the field of optics [2]. This microscope is based on point-excitation (illumination) and point-detection systems combined with a scanning mechanism. The sample or laser beam is mechanically or optically scanned so that fluorescence, reflection, and absorption are measured point by point. The detected signal is sequentially processed on a digital or analog computer to form the images. In contrast with the conventional optical microscopes, the confocal fluorescence and reflection ones have the capability of three-dimensional imaging. Furthermore, the confocal microscopes provide clear images free from speckle and interference fringe. Flare and scattered light are also negligibly weak due to the use of a pinhole in the detection system.

The time-resolved fluorescence microspectroscopic system developed is based on single-photon timing and the confocal fluorescence microscope [3]. Fig. 1 shows the optical diagram of this microscope. The difference between this system and a conventional fluorescence microscope is the use of two pinholes. The first pinhole is set in front of a light source (usually a laser) to limit it to a small spot. Excitation light from this minute source is reflected by a dichroic mirror and focused onto a sample by an objective lens. Fluorescence emitted from the sample is collected by the same objective lens and imaged on the second pinhole, and only the fluorescence passing through the pinhole is detected.

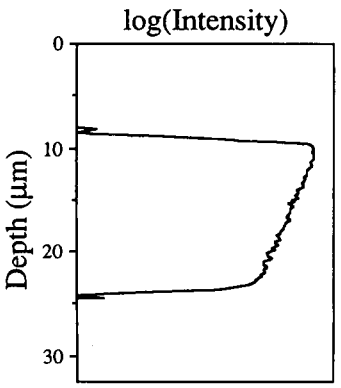

Fig. 2. Fluorescence depth-profile of a pyrene-doped PMMA film.

This optical arrangement is a key to providing three-dimensional space resolution. Since fluorescence from the focal spot is condensed on the second pinhole, most of its energy goes through. On the other hand, as fluorescence from out-of-focus positions is defocused on the pinhole plate as shown by dotted lines in Fig. 1, most of its energy is cut off. Therefore, the observed fluorescence is ascribed to the minute volume so that the longitudinal resolution is obtained besides the lateral resolution. The sample is set on an *XYZ* scanning stage and moved for measuring the three-dimensional structure.

As one of the applications of the system, the quantitative concentration estimation of dye molecules in small volumes is described [3]. Fig. 2 shows a fluorescence depth profile of pyrene in a poly(methyl methacrylate) (PMMA) film. Pyrene fluorescence at 385 nm was observed along the longitudinal axis perpendicular to the films. The fluorescence intensity varies inside the films, which can be explained in terms of attenuation of the excitation light in the films. The intensity of the excitation light decreases as the light penetrates deeper, because it is absorbed by pyrene. The logarithmic plots of the fluorescence intensities are well fitted to linear lines, which indicates that pyrene was homogeneously distributed, and the Lambert–Beer law held for the attenuation in the films. The pyrene concentration determined based on the homogeneous distribution has a good relation to the gradient of the logarithmic curves, so that the molar absorptivity at 293 nm (excitation wavelength) can be calculated.

Fig. 3 shows a depth profile of a PMMA latex particle with a diameter of 7.2 μm. The PMMA latex was soaked in a methanol solution of pyrene, washed with cold water, and then dispersed in pure water. The use of the molar absorptivity given by the curves in Fig. 2 makes it possible to estimate the pyrene concentration in the latex particle. The concentration obtained was 4.9×10^{-2} M. It is noteworthy that this concentration estimation is very powerful, since it is not affected by surrounding materials even if the surroundings absorb or scatter the light.

Here, some problems with the present system are pointed out and considered. The most serious problem with microspectroscopy is chromatic aberration. Since the focal length of an objective lens depends on the wavelength, the depth coordinates on fluorescence images observed at different wavelengths are shifted away from each other. Therefore, the chromatic aberration causes distortion of spectra obtained at small volumes. In the developed system, the chromatic aberration is automatically compensated by varying the position of both the sample stage and the pinhole of the excitation system as a function of wavelength [3]. The other problem is damage of a sample caused by the high-intensity excitation. The laser beam is condensed onto the sub-μm spot, so that the excitation pulse energy often rises to over tens mJ cm^{-2}. Such an intense light may damage most of the molecular materials. Therefore, the intensity of the excitation laser has to be attenuated and adjusted to be below the damage threshold of the sample. Under the latter condition, the observed fluorescence usually becomes weak. Fortunately, the developed system has the advantage of high detection efficiency due to the high numerical aperture of the objective lens, which overcomes the weakness of the fluorescence intensity.

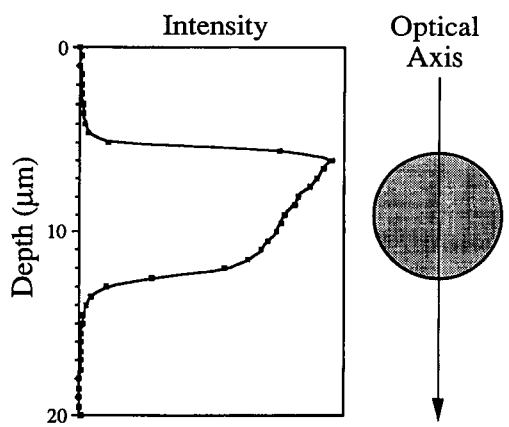

Fig. 3. Depth profile of pyrene concentration in the PMMA latex particle (diameter 7.2 μm).

3. Fluorescence analysis of a single microcapsule in solution

As the excimer dynamics of aromatic molecules in solution are dependent on the concentration and solvent viscosity, the precise excimer fluorescence measurement and analysis of a single microparticle are expected to give information on properties of individual microparticles. We describe here excimer formation kinetics in a microcapsule containing a toluene solution of pyrene [4]. Microcapsules possess unique geometrical structures with solvents being encapsulated by the thin polymer resin walls, and are widely used for industrial applications. Their physical and chemical nature are determined by the chemical composition of the polymer, the contained molecules, and their concentration. The microcapsules were dispersed in pure water, and pyrene fluorescence was measured by the time-resolved fluorescence microspectroscopic system.

First, we summarize the pyrene fluorescence dynamics of the solution obtained by spatially unresolved (conventional) spectroscopy. The concentration of the mother toluene solution was adjusted to be 8.1×10^{-3} M. Both monomer and excimer fluorescence emissions of pyrene were observed, with maxima at 475 nm and 384 nm, respectively, and their fluorescence intensity ratio (I_E/I_M) was 2.4. The I_E/I_M value is determined by the concentration of pyrene, and was estimated to be 1.14×10^{-2} M by referring to the concentration dependence of I_E/I_M in air-saturated toluene. This was slightly higher than that of the mother solution. Since the sample solution was not deaerated, the excited pyrene is quenched by oxygen, showing relatively fast decay. Actually the excited pyrene monomer showed a decay of 17.5 ns in diluted solution.

In homogeneous solution, pyrene excimer formation is known to proceed via the Birks kinetics model [5] as shown in Scheme 1. where k_{DM} and k_{MD} are the rate constants of the excimer ($^1D^*$) formation and the dissociation of $^1D^*$ to the excited ($^1M^*$) and ground state

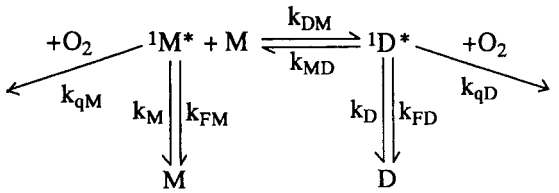

Scheme 1.

pyrene (M), respectively; k_{FM} and k_{FD} are the radiative rate constants of $^1M^*$ and $^1D^*$, respectively; k_D and k_M are the non-radiative decay rate constants of $^1D^*$ and $^1M^*$, respectively; and k_{qM} and k_{qD} are the quenching rate constants by O_2. According to this scheme, the time response of the monomer [$i_M(t)$] and excimer fluorescence [$i_D(t)$] can be expressed as in Eqs. 1 and 2, respectively.

$$i_M(t)=\frac{k_{FM}(\lambda_2-X)}{(\lambda_2-\lambda_1)}(e^{-\lambda_1 t}+Ce^{-\lambda_2 t}) \quad (1)$$

$$i_D(t)=\frac{k_{FD}k_{DM}[^1M]}{(\lambda_2-\lambda_1)}(e^{-\lambda_1 t}-e^{-\lambda_2 t}) \quad (2)$$

where

$$\lambda_{1,2}=\frac{1}{2}[X+Y\mp\{(Y-X)^2+4k_{MD}k_{DM}[^1M]\}^{(1/2)}]$$

$$C=(X-\lambda_1)/(\lambda_2-X)$$

$$X=k_M+k_{FM}+k_{qM}[O_2]+k_{DM}[^1M]$$

$$Y=k_{FD}+k_D+k_{MD}+k_{qD}[O_2]$$

Eqs. 1 and 2 indicate that both curves of the monomer decay and excimer decay/rise are characterized by the same time constants of λ_1 and λ_2 if the Birks model prevails for the pyrene excimer formation in the capsules. For the data obtained by spatially unresolved spectroscopy, however, $i_M(t)$ and $i_D(t)$ did not obey double-exponential functions and the excimer fluorescence showed a relatively slow rise. Phenomenologically, it is clear that the pyrene excimer formation observed for the microcapsules by spatially unresolved spectroscopy cannot be explained based on the Birks kinetic model.

The fluorescence spectrum and its dynamics for pyrene in a single microcapsule are now measured by time-resolved fluorescence microspectroscopy. Fluorescence spectra as well as $i_M(t)$ and $i_D(t)$ for three different microcapsules are shown in Fig. 4. It is clearly demonstrated that the efficiency of the excimer formation is quite different between the capsules. The microcapsule with relatively large I_E/I_M show faster monomer decay as well as faster excimer rise as compared with that showing smaller I_E/I_M. In contrast to the results on an ensemble of microcapsules, furthermore, $i_M(t)$ and $i_D(t)$ for individual microcapsules were fitted by double-exponential functions. Analo-

gous results were obtained for a number of microcapsules. These results clearly indicate that the pyrene excimer formation in an individual microcapsule can be explained by the Birks kinetic model as found in homogeneous solutions. The origin of the multi-exponential behavior in the dispersed solution is due to the observation of the sum of various microcapsules with different fluorescence dynamics.

Before discussing excimer formation dynamics in individual microcapsules, possible origins for the variation of the excimer formation efficiency (I_E/I_M) with the capsules are to be considered. The factors influencing excimer formation are viscosity of the inner solution and concentration of pyrene in each capsule. The viscosity of the inner toluene solution might increase with decreasing the size of the capsule owing to an increase in the contribution of the surface forces between the melamine-resin wall and toluene to the viscosity. To test such possibilities, we selected various sizes of the microcapsules and determined I_E/I_M of each capsule as shown in Fig. 5. I_E/I_M was not correlated to the size of the capsule, indicating that the viscosity of the inner toluene solution is not a factor governing I_E/I_M of each capsule. The most probable explanation for the variation of I_E/I_M and the fluorescence dynamics with the capsules will be a scatter of the pyrene concentration. I_E/I_M of 1.9 ~ 2.9 in Fig. 5 correspond to distributions of the pyrene concentration of $8.5\times10^{-3} \sim 1.3\times10^{-2}$ M.

Knowing that the variation of I_E/I_M with the capsules can primarily be ascribed to that of the pyrene concentration, we analyzed the $i_M(t)$ and $i_D(t)$ profiles in Fig. 4 based on Eqs. 1 and 2, respectively. Double exponential fittings of $i_M(t)$ and $i_D(t)$ were not fortuitous

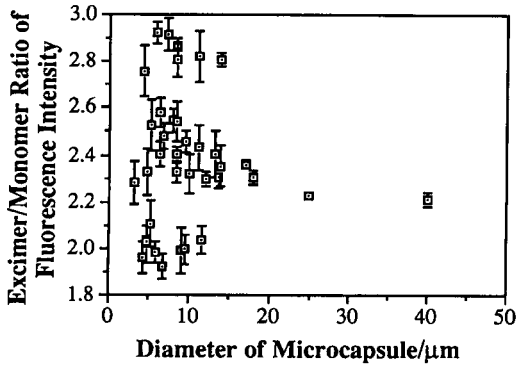

Fig. 5. Excimer and monomer fluorescence intensity ratio of microcapsules as a function of the diameter.

and the excimer formation in every single capsule was analyzed by using Eqs. 1 and 2. λ_1 and λ_2, and their pre-exponential factors A_1 and A_2, respectively, were thus obtained for three microcapsules. λ_1 and λ_2 determined at 384 nm (monomer) coincide fairly well with the corresponding values observed for the excimer fluorescence at 475 nm for a given capsule. Furthermore, A_1 and A_2 are also in good agreement with the expectations from Eqs. 1 and 2; $(A_1+A_2) \sim 1.0$ and $(A_1-A_2) \sim 0$ for $i_M(t)$ and $i_D(t)$, respectively.

The rate parameters for the excimer dynamics, k_{DM} and k_{MD}, in the capsule could be obtained from Eqs. 1 and 2 as in Table 1, since the concentration of pyrene was estimated and $(k_M+k_{FM}+k_{qM}[O_2])$ in each capsule was measured. $(k_M+k_{FM}+k_{qM}[O_2])$ was determined to be 5.7×10^6 s^{-1} in a diluted toluene solution of pyrene (1.0×10^{-5} M) in air. k_{DM}, k_{MD}, and $(k_D+k_{FD}+k_{qD}[O_2])$ were thus determined to be $(5.8 \sim 6.7)\times10^9$ M^{-1} s^{-1}, $(5.4 \sim 7.1)\times10^6$ s^{-1}, and $(6.7 \sim 7.7)\times10^7$ s^{-1}, respectively, as listed in Table

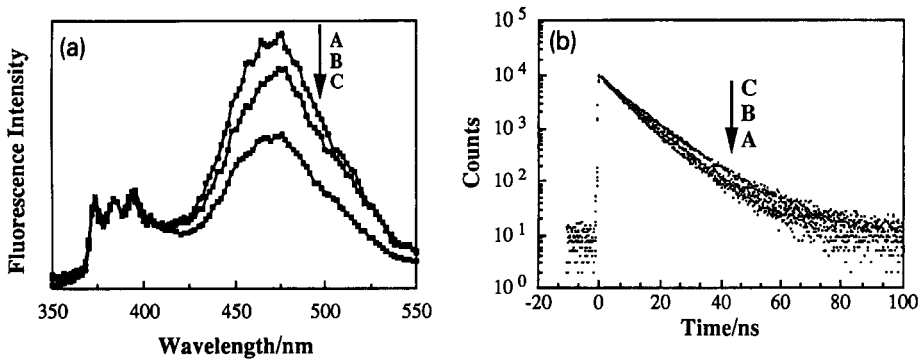

Fig. 4. (a) Fluorescence spectra of three different microcapsules (A, B, and C) containing a toluene solution of pyrene, and (b) the corresponding decay curves of the pyrene monomer.

Table 1
Rate parameters for pyrene excimer formation in a single microcapsule

Sample [a]	I_E/I_M	Concentration (10^{-2} M)	k_{DM} ($\times 10^9$ M^{-1} s^{-1})	k_{MD} ($\times 10^6$ s^{-1})	$k_D+k_{FD}+k_{qD}[O_2]$ ($\times 10^7$ s^{-1})
A	2.8	1.34 [b]	6.3	7.1	7.7
B	2.5	1.18 [b]	5.8	5.4	7.3
C	1.7	0.82 [b]	6.7	5.7	6.7
Solution	1.3	0.64	6.4	6.6	6.9

[a] Samples A, B and C are the same as those in Fig. 4.
[b] The concentration was estimated from its dependence of I_E/I_M in toluene (separate experiments).

1. The value estimated for each capsule is comparable to that determined for a homogeneous toluene solution of pyrene (6.4×10^{-3} M, see Table 1). The variation of I_E/I_M with the capsules are therefore reasonably explained by that of the pyrene concentration in the capsule, and the excimer formation dynamics in each microcapsule is concluded to be similar to that in a homogeneous bulk solution.

One possible origin of the concentration distribution between the capsules may be inhomogeneous location of pyrene. Its precipitation in inner toluene solution and adsorption/incorporation in the polymeric capsule wall are denied on the basis of data for $i_M(t)$ and $i_D(t)$. The concentration distribution could be determined during the synthesis of the microcapsules. Evaporation of toluene during vigorous stirring of a pyrene–toluene solution in water will account for the higher I_E/I_M values than the average (>2.3). For the capsules with $I_E/I_M<2.3$, on the other hand, we suspect that partition of water into the toluene droplets, leading to microcrystallization of pyrene followed by its exclusion from the droplets, is responsible. The evaporation rate of a toluene droplet and partition of water into the toluene layer will also be influenced by the polymerization rate and wall thickness of the capsule. It is worth noting that the polymerization rate and the thickness of the capsule wall will be scattered among the capsules, since emulsion polymerization of the reactions proceeds in inhomogeneous toluene–water solution. All these factors should be related to each other and result in the present fluorescence characteristics of microcapsules.

4. Time-resolved absorption microspectroscopy

Absorption spectroscopy is indispensable for identifying non-luminescent excited states, chemical intermediates, and hot molecules, and for analyzing their behaviors. Unfortunately, the absorption (transmission)-mode confocal microscope is not applicable to the three-dimensional measurement, since an optical transfer function of this microscope is angularly band-limited so that the depth resolution is degraded, especially for laterally structureless samples such as films and stacking layers. This difficulty is common for conventional absorption microscopes. In order to obtain three-dimensional resolution, we developed a new confocal microscope [6].

Fig. 6 shows an optical diagram of the microscope. Excitation light from a point source is focused on a sample by an objective lens, as in the case of the fluorescence excitation system. This light excites molecules so that the concentration is proportional to the photon density. An absorption-monitoring laser is

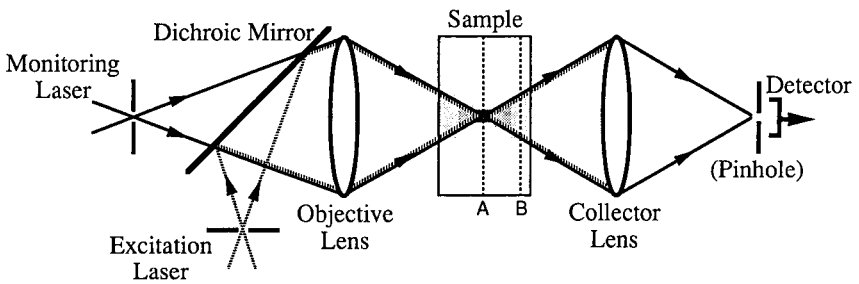

Fig. 6. Optical diagram of a confocal transient absorption microscope.

introduced coaxially and condensed confocally with the excitation system. The transient absorption in the object is imaged by a collector lens and observed by an incoherent detector. Here, let us consider the imaging of a thin film doped with absorptive molecules. When the film is set on the focal plane denoted as A in Fig. 6, the excitation light is condensed to a diffraction-limited spot on the film so that the molecules should be excited densely. Since the monitoring light is transmitted only through the excited area, the film works as a dense attenuation filter. A larger area of the film at an out-of-focus plane (B in Fig. 6) is irradiated with much weaker intensity compared to the position A, so that the density in the excited state is decreased. Since the transient absorption is proportional to the concentration of the excited molecules, the absorbance is much smaller than that of the film at position A. Therefore, the observed transient absorption is mainly contributed by the focal spot. This shows that the present confocal transient absorption microscope has three-dimensional space resolution. In contrast with this microscope, the conventional confocal absorption microscope, which measures ground-state absorption without the excitation system, has no depth resolution, because the ground-state concentration is independent of the position.

We developed a time-resolved absorption microspectroscopic system based on the present microscope and a pump-probe method. The system utilized the same laser source and microscope as those of the fluorescence system. Second harmonic and fundamental pulses of the dye laser were used as the excitation and monitoring lights, respectively. Since the laser power is highly intensified by condensing a beam at the focal spot, a nJ excitation pulse is enough for the transient absorption measurement under the microscope, which has been normally performed by mJ pulse lasers such as Q-switched YAG and amplified dye lasers. The monitoring pulse was optically delayed with respect to the excitation pulse, and the delay time was scanned so that the temporal variation of the transient absorption could be observed. The detected signal was processed by a lock-in amplifier with a chopping signal of 1 kHz to precisely measure the transient absorption.

Fig. 7a shows the result of a depth-profile measurement of $S_n \leftarrow S_1$ absorption of *p*-terphenyl in cyclohexane solution layer with a thickness of ~ 100 μm. The $S_n \leftarrow S_1$ transition of *p*-terphenyl molecules was measured along the longitudinal axis perpendicular to the layer. The depth resolution of this system could be determined from the profile to be 1.5 μm, which was defined as the FWHM of a differential curve at the interface between the quartz plate and the solution. Fig. 7b shows a decay curve of the transient absorption observed at the middle of the solution layer. The time resolution was determined from this curve to be 10 ps. To the best of our knowledge, this is the first demonstration of a depth-resolved absorption measurement under a microscope.

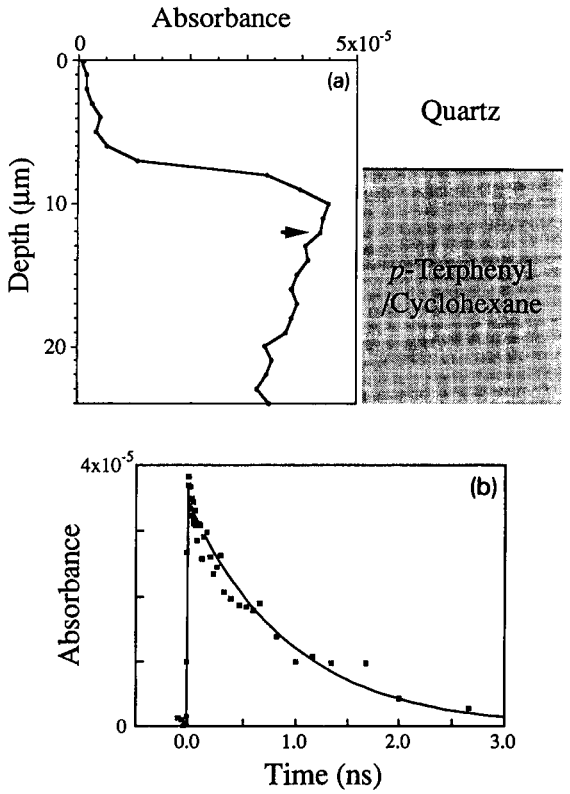

Fig. 7. (a) Depth profile and (b) decay curve of $S_n \leftarrow S_1$ absorption of *p*-terphenyl in a cyclohexane liquid layer.

5. Laser manipulation of a single microparticle in solution

Time-resolved fluorescence and absorption microspectroscopy is an excellent method for characterizing physical properties and analyzing chemical dynamics of minute sites of surfaces and small materials. If the microparticles are dispersed in solution, they undergo

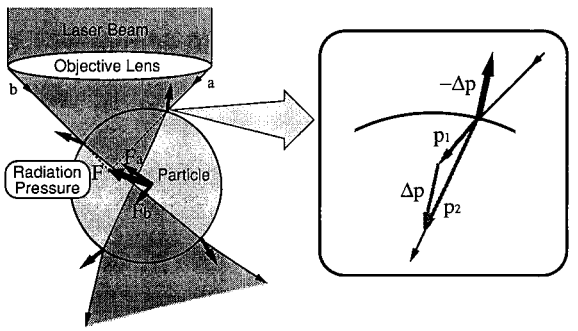

Fig. 8. Principle of laser trapping.

Brownian motion, disturbing precise measurement of time-resolved fluorescence and absorption. We have proposed that laser trapping due to radiation pressure is an extremely fruitful means of catching, transferring, and fixing the particle at a certain position, thus overcoming the problem [7,8].

Although light has no mass, a single photon possesses the momentum given by Planck's constant divided by the wavelength of light (h/λ). When a photon flux is reflected by a mirror, the momentum of each photon is changed in its direction. Based on the conservation law of momentum, the photon momentum is transferred from the incident light to the mirror, which causes the force on the mirror surface. This force is called radiation pressure. The net force of a photon flux (F), which is given as the product of the photon momentum change and the number of photons colliding on the mirror, is also expressed as a function of the laser power P, as follows,

$$F = \frac{P}{c}\cos\theta \qquad (3)$$

where c and θ are the velocity of light and the incident angle, respectively. For example, a 1 m laser beam perpendicularly incident on a mirror exerts a force of 7×10^{-12} N.

The radiation pressure exerted on a microparticle under irradiation by a focused laser beam is schematically illustrated in Fig. 8. The laser light incident on a particle is refracted twice at the boundary when it goes in and out of the particle. As in the case of reflection, refraction of light induces the photon momentum change, since the propagation direction and the wavelength are changed in the different refractive index media. The momentum change, $\Delta\mathbf{P} = \mathbf{P}_1 - \mathbf{P}_0$, where $\mathbf{P}_1$ and $\mathbf{P}_0$ are momentums before and after refraction, respectively, is transferred to the particle, so that the radiation pressure is exerted in the direction opposite to that of $\Delta\mathbf{P}$ (i.e., $-\Delta\mathbf{P}$), as shown in Fig. 8. If the refractive index of the particle (n_p) has no imaginary part (no absorption) and a real part larger than that of the surrounding medium (n_m), the sum of forces at each point of the particle irradiated by the laser beam is directed to the high intensity region at the focal point. Hence, the particle is attracted to the focused beam and three-dimensionally trapped in the vicinity of the focal point against the thermal Brownian motion, gravity, and convection [9].

Maxwell's equations show that radiation pressure is extremely weak, and is comparable to attractive forces between single atoms or molecules. Although macroscopic objects cannot be moved by such a weak force, the motion of μm-sized particles is appreciably influenced by the radiation pressure. The gravity force exerted on a 1-μm water droplet is $\sim5\times10^{-15}$ N, and the viscous resistance on a 1-μm particle moving at a velocity of 1 μm s^{-1} in water is $\sim9\times10^{-15}$ N, which are much smaller than the radiation pressure. Hence, we can observe a small object being levitated and transferred by light under a microscope. When the trapping technique is combined with the above described microspectroscopic systems, fluorescence and absorption spectral measurements of a single manipulated particle are made possible.

6. Viscosity analysis of a single manipulated oil droplet

Measurement of transient absorption spectra of a microparticle was made possible by introducing a C flash lamp as a probe. It was confirmed that the depth resolution was about 8 μm and the diameter of a single droplet was regarded as the optical path length. A Brownian particle of oil droplet was trapped by a 1064 nm CW YAG laser beam and measured by the time-resolved absorption microspectroscopy. We present an investigation on a triplet–triplet (T–T) annihilation process, which is limited by molecular diffusion, and demonstrates the inner viscosity of microdroplets. In view of its spectroscopic characteristics and solubility zinc–tetraphenylporphyrin (ZnTPP) was dissolved in tri-*n*-butyl phosphate (TBP) microdroplets, which gave a broad T–T absorption band at 465 nm and a

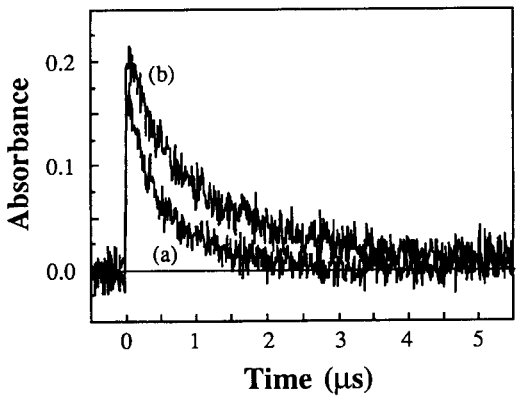

Fig. 9. Decay curves of ZnTPP $T_n \leftarrow T_1$ absorption in (a) a TBP droplet and (b) TBP film.

depletion at 556 and 597 nm upon excitation [10]. The decay profiles of ZnTPP $T_n \leftarrow T_1$ absorbance in a microdroplet and the reference TBP solution are shown in Fig. 9. Although the lifetime of the ZnTPP triplet state was reported to be 3 ms, the present decay was completed in a few μs. The inverse plot of $T_n \leftarrow T_1$ absorbance with time showed a linear relation, meaning that the bimolecular decay of T–T annihilation was confirmed. Using molar absorptivity of the ZnTPP $T_n \leftarrow T_1$ transition ($\epsilon = 9000\ M^{-1}\ cm^{-1}$ at 465 nm) and assuming the diameter as the path length, the T–T annihilation rate constant (k_{TT}) was estimated to be $(2.9 \pm 0.7) \times 10^9\ M^{-1}\ cm^{-1}$ for a droplet of 20 μm diameter. Systematically, k_{TT} was measured as a function of the droplet diameter and plotted. It is interesting that k_{TT} for the droplet is always larger than that of the solution and increases with decreasing diameter.

The T–T annihilation process in solution is a diffusion-controlled process, and its rate constant is expressed as follows.

$$k_{TT} = k_{diff} = \frac{8RT}{3000\eta} \quad (4)$$

Here k_{diff} is the rate constant of the diffusion-controlled reactions, R is the gas constant, T is the temperature, and h the viscosity. The viscosity of a single microdroplet with a diameter of 20 μm was found to be 1.8 ~ 3.2 cP at 20°C. Thus, the interesting dependence of k_{TT} upon the diameter is now ascribed to the difference in viscosity, and the viscosity is considered to increase as the droplet diameter is decreased. One possible explanation of the difference is to assume water penetration into the droplet. This was confirmed directly by measuring k_{TT} of the thick (60 μm) TBP solution film saturated with aqueous sodium dodecyl sulfate solution. The obtained value of $(2.1 \pm 0.3) \times 10^9\ M^{-1}\ s^{-1}$ is larger than that of the TBP film. Furthermore, it was already reported that the water solubility in TBP droplets was as large as 23%, and the TBP droplet was swollen by water. The μm size effect on the viscosity in TBP droplets is an extremely interesting result that should be examined in detail.

7. Conclusions

Time-resolved fluorescence and absorption microspectroscopic systems were developed by combining pulsed lasers, microscopes and a flash lamp. The μm space- and ps time-resolutions were simultaneously satisfied, enabling the elucidation of photophysical and chemical processes occurring in small domains. Furthermore, the laser trapping method was introduced to fix a Brownian particle in solution at a focal point. Fluorescence and absorption spectroscopy are extremely useful to characterize physical and chemical properties of a single microparticle. The concentration distribution between individual microparticles and diameter dependence of viscosity in individual oil droplets can thus be discussed.

Acknowledgements

Collaboration and discussion with Drs. N. Kitamura, H. Misawa, M. Koshioka, and S. Funakura are greatly acknowledged.

References

[1] H. Masuhara, Proceedings of the JRDC–KUL Joint International Symposium on Spectroscopy and Chemistry in Small Domains, Elsevier, Amsterdam, in press.
[2] T. Wilson, (Ed.), Confocal Microscopy, Academic Press, London, 1990.
[3] K. Sasaki, M. Koshioka and H. Masuhara, Appl. Spectrosc., 45 (1991) 1041.
[4] M. Koshioka, H. Misawa, K. Sasaki, N. Kitamura and H. Masuhara, J. Phys. Chem., 96 (1992) 2909.
[5] J.B. Birks, Photophysics of Aromatic Molecules, Wiley Interscience, New York, 1970.

[6] K. Sasaki, M. Koshioka and H. Masuhara, J. Opt. Soc. Am. A, 9 (1992) 932.
[7] H. Masuhara, Pure Appl. Chem., 64 (1992) 1278.
[8] K. Sasaki, Proc. SPIE, 1711 (1992) 99.
[9] A. Ashkin, J.M. Dziedzic, J.E. Bjorkholm and S. Chu, Opt. Lett., 11 (1986) 288.
[10] S. Funakura, K. Nakatani, H. Misawa, N. Kitamura and H. Masuhara, J. Phys. Chem., submitted for publication.

ELSEVIER

Analytica Chimica Acta 299 (1995) 319–326

ANALYTICA CHIMICA ACTA

Use of 3-(*p*-carboxybenzoyl)quinoline-2-carboxaldehyde to label amino acids for high-sensitivity fluorescence detection in capillary electrophoresis

Edgar A. Arriaga, Yanni Zhang, Norman J. Dovichi *

Department of Chemistry, University of Alberta, Edmonton, T6G 2G2 Alberta, Canada

Received 15 January 1994; revised manuscript received 17 February 1994

Abstract

Detection of amino acids by laser-induced fluorescence capillary electrophoresis can be achieved by using a fluorogenic reagent, 3-(*p*-carboxybenzoyl)quinoline-2-carboxaldehyde (CBQ). This reagent does not fluoresce unless it has reacted with a primary amine to form an isoindole derivative. Using a sheath flow cuvette as a post-column detector and excitation by the 488-nm argon ion laser line we obtain a limit of detection of 9.0 zeptomoles (1 zeptomol = 10^{-21} mol) for the CBQ–arginine derivative, which is 150 times better than previously reported. We also investigate and optimize the derivatization reaction by successfully labeling arginine concentrations as low as 10^{-7} M. CBQ–arginine derivatives from lower concentrations of this amino acid cannot be detected due to secondary reactions of CBQ and cyanide, which generate background peaks that swamp the CBQ-amino acid peak.

Keywords: Electrophoresis; Fluorimetry; Amino acids; Labeling; Lasers

1. Introduction

Free amino acids are vital in many physiological functions as neurotransmitters, regulators of metabolic pathways, transport mechanisms, and building blocks for peptide and protein synthesis by ribosomes. Also, amino acid analysis of the hydrolysate of proteins and peptides is an important step in protein characterization. Understanding the role of amino acids in different biological disciplines such as physiology, cell biology, molecular biology, and biotechnology would require the detection of extremely low concentrations of these biomolecules in usually microscopic volumes (i.e. single-cell physiological studies). These requirements can only be fulfilled with the development of extremely sensitive analytical techniques. A similar situation is found in other disciplines such as forensic medicine, astronomy, palaeontology, and archaeology, which usually depend on analysis of scarce or extremely valuable samples.

A promising technology for the analysis of such samples is laser-induced fluorescence (LIF) detection combined with capillary electrophoresis (CE). Routinely, this laboratory can detect fluorescent compounds below the zeptomole level (1 zeptomol = 10^{-21} mol = 600 molecules); we have reported limits of detection as low as 30 molecules of tetramethylrhodamine [1]. Using various labeling schemes fluorescent amino acid derivatives have been detected in the zeptomole range [1–4].

* Corresponding author.

SSDI 0003-2670(94)00315-7

There are certain cases where detection of minute amounts of dye-labeled compounds is of interest; for example, enzyme assays can be developed based on a fluorescent substrate. Similarly, enzymes are used in Sanger's DNA sequencing technology where a fluorescent primer is extended to synthesize labeled nucleotides. Also, tracer studies can be based on fluorescent compounds. In each of those cases, the fluorescent precursor can be synthesized and purified at high concentrations and diluted before use. However, it is much more common to detect minute amounts of substances, such as amino acids, that must be derivatized before analysis. Labeling chemistry then becomes problematic because relatively high concentrations of reagent (greater than 10^{-5} M) are usually required for the derivatization step.

For LIF detection of amino acids, several strategies have been investigated to attach a fluorescent tag to an amino group. Some investigators use pre-column derivatization, while others have used post-column derivatization [5]. Post-column derivatization has been used for fast-forming short-lived fluorescent derivatives of labeling reagents, such as *o*-phthalaldehyde (OPA) and fluorescamine. These reagents (called fluorogenic reagents) do not fluoresce unless they have reacted with an amine function. This property offers the advantage of a non-fluorescent background. However, the sensitivity is low due to a low yield reaction and dilution with the fluorogenic reagent. The limit of detection for post-column derivatization of amino acids is usually in the picomole range.

Pre-column derivatization is preferred when maximum sensitivity is desired. The derivative needs to be stable longer than the time required to complete the separation. Usually these derivatives are fluorescent per se, which imposes the need of a highly efficient separation of fluorescently labeled products and the fluorescent reagent. In general, CE offers excellent separation and will be compatible with the detection requirements. Some of these reagents are isothiocyanates, succinimidyl esters, or sulfonyl chlorides of fluorescein or tetramethylrhodamine, and 9-fluorenylmethyloxycarbonyl chloride. While detection limits for amino acid derivatives of these reagents are in the low zeptomole range [2–4,6], these derivatives are difficult to form when the concentration of amino acids is low ($< 10^{-5}$ M). One disadvantage is the need of high concentration of the reagent to obtain a high reaction yield. Another disadvantage is hydrolysis of the reagent that results in fluorescent byproducts. Unreacted reagent and hydrolysis fluorescent products show peaks that could overlap amino acid peaks, interfering with the determination of minute amounts of amino acids.

An alternative to fluorescent reagents in pre-column derivatization has been the development of stable fluorogenic (non-fluorescent) reagents. They allow the use of high concentrations without interfering with the derivative peaks, resulting in higher yields, and allowing detection of extremely diluted samples. For example, OPA can be used for pre-column derivatization, but its amino acid derivatives show poor stability, low yield, and short excitation wavelength (maximum absorption at 334 nm) [7]. Another fluorogenic reagent, 2,3-naphthalenedicarboxaldehyde (NDA), has an excitation maximum at 462 nm, which makes it more attractive for LIF detection. The NDA amino acid derivatives show improved stability when using cyanide as nucleophile [8,9]. NDA derivatives are unstable when the nucleophile is a thiol. The most recent generation of fluorogenic reagents are quinolines. They are very stable, show high fluorescent yields, and offer different options for excitation/emission in LIF detectors [10–13].

In the present work, ultrasensitive detection of amino acids is based on the use of the fluorogenic reagent 3-(*p*-carboxybenzoyl)quinoline-2-carboxaldehyde (CBQ). The maximum excitation and emission of its glycine derivative are at 466 and 544 nm, respectively. The use of CBQ to generate fluorescent amino acid derivatives has been demonstrated previously [10]. In addition to its improved stability, this reagent offers the advantage of being non-fluorescent unless it has reacted with an amino group. As a consequence, it is very attractive for LIF-CE because a high concentration could be used to favor the kinetics of formation of the fluorescent derivative. We examine parameters that affect the labeling reaction in order to improve the reaction yield and eliminate secondary reactions.

In terms of the detection scheme, matching of the maximum absorption of the derivative to a laser line does not necessarily assure better response of the detector. In a well designed optical system, Raman and Raleigh scattering contribute significantly to the background signal, degrading limits of detection [6,14]. We explore the use of alternative laser lines and inter-

ference filters combined with a sheath flow cuvette post-column detector to obtain zeptomole limits of detection of CBQ derivatives.

2. Experimental

2.1. Capillary electrophoresis

The capillary electrophoresis system for micellar electrokinetic capillary chromatography (MECC) consists of a capillary with one end immersed into the running buffer or sample along with a Pt wire electrode, which supplies high voltage from a high-voltage power supply (CZE1000R, Spellman, Plainview, NY), Fig. 1. This end of the capillary is enclosed inside a Plexiglas box provided with a safety interlock to avoid risk of electric shocks. The other end of the capillary (from which the polyimide coating has been removed by a gentle flame) is inserted inside a sheath flow cuvette, which is part of the fluorescence detector. The power supply is controlled through the input/output board.

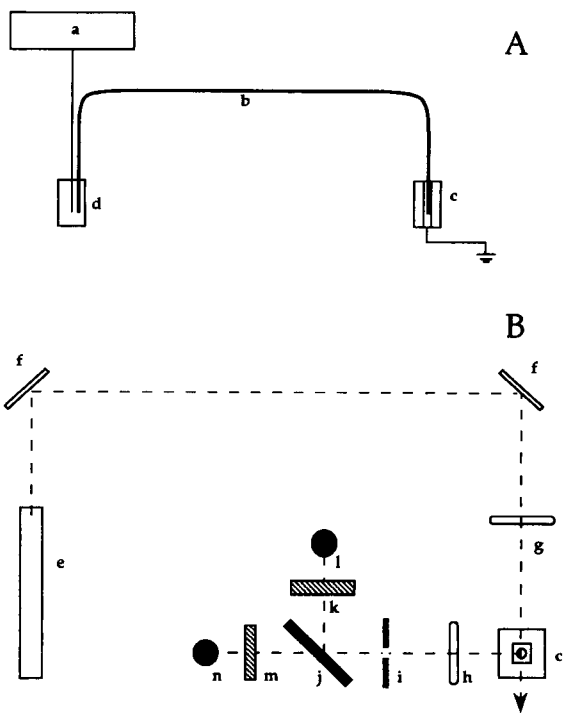

Fig. 1. Schematic diagram of capillary electrophoresis system and detector. (A) Electrophoresis system: (a) high-voltage power supply, (d) sample or running buffer vial, (b) capillary, (c) virtual grounded sheath flow cuvette. (B) Detector: (e) multi-wavelength argon-ion laser, (f) mirrors, (g) focusing objective, (c) sheath flow cuvette, (h) collecting objective, (i) adjustable slit, (j) dichroic beam splitter @ 590 nm, (k) 535DF45 interference filter for reflected channel, (m) 630DF55 interference filter for transmitted channel, (l,n) photomultiplier tubes.

Samples are diluted in 10 mM borate and 10 mM sodium dodecyl sulfate buffer (BS buffer), pH 9.4, prior to injection. Electrokinetic injection of diluted samples is controlled using the input/output board mentioned above. Time and injection voltage are adjusted to introduce less than 1% of the total capillary volume (i.e. 5 s at 100 V cm^{-1}). Elution using BS buffer at 400 V cm^{-1} is typical.

2.2. Detector

Details of the detector have been published previously [6]. Briefly, a sheath flow cuvette (200×200 μm inner bore) is used as post-column detector (Fig. 1). The 488 nm line from the multi-wavelength argon-ion laser (Innova 90-4, Coherent, Palo Alto, CA) is focused by a 6.3× microscope objective (Melles Griot, Nepean, Ontario) and excites fluorescent eluting species. The laser beam is focused about 20 μm from the tip of the capillary. The fluorescence is collected at 90° from the direction of excitation by a 60× (N.A. 0.70) microscope objective (Model 60×-LWD, Universe Kogaku, Japan) and imaged onto an adjustable slit in order to eliminate scattered light. Fluorescence is then directed to a 590DRLP@45° XF40 dichroic mirror (Omega Optical, Brattleboro, VT). Fluorescence below 590 nm is reflected at 90° toward a 535DF45 bandpass filter (Omega Optical, Brattleboro, VT), followed by an R1477 photomultiplier tube (PMT) (Hamamatsu, Middlesex, NJ); this portion of the optical system is called the reflected channel. Light above 590 nm is transmitted toward a 630DF55 bandpass filter (Omega Optical) followed by a second R1477 PMT; this portion of the optical system is called the transmitted channel. We did not use the transmitted channel for the present study.

PMT currents are converted to appropriate signals for data acquisition using a 1 MΩ resistor and a 10 Hz bandwidth filter. Data are collected at 10 Hz in the Macintosh IISI via an NB-MIO-16×-18 input/output board (National Instruments, Austin, TX).

2.3. Alignment

Positions of the sheath flow cuvette and the focusing objective are controlled respectively by a combination of three and two axes translation stages (Newport Instruments Canada Corporation, Mississauga, Ontario). We use a microscope equipped with a 10× objective and 10× eyepiece and fitted with a colored glass filter to block scattered laser light to observe the illuminated sample region. Alignment is adjusted so that the fluorescence produced while continuously injecting fluorescein (Molecular Probes, Eugene, Oregon) is visually superimposed with the image of the slit produced by a light emitting diode (LED) placed behind the slit [6]. For fine alignment, the LED is removed and the ratio of the fluorescent signal to square root of background signal is maximized. During alignments, the PMT voltage is kept low to avoid damage to the photomultiplier tube. After alignment, the capillary is flushed by electrokinetically flowing BS buffer from two fresh vials in succession, and the PMT voltage is increased to 1200 V.

2.4. Labeling reaction

A stock solution of CBQ (Molecular Probes) is prepared by sonicating the reagent in methanol. The final concentration is 10.0 mM CBQ. The solution is stored at −20°C. A cyanide stock solution is prepared by dissolving KCN (Molecular Probes) in distilled water. The final concentration was 0.2 M. This solution was kept at −20°C. A working cyanide solution was prepared by dilution to 50 mM in distilled water. This solution was kept at 4°C and discarded after one week. Arginine (Sigma Diagnostics Canada, Mississauga, Ontario) stock solution was prepared in distilled water, (1.0×10^{-2} M). This solution was stored at 4°C. Fresh dilutions of the amino acid solution for labeling reactions were prepared daily.

Typical labeling reactions were carried out in a 25 μl total volume: 2.5 μl of amino acid solution, 11.5 μl of methanol or an aqueous buffer, 1 μl of 50 mM CN^- (final concentration is 2 mM), and 10 μl of CBQ stock solution (final concentration is 4.0 mM). The reaction was allowed to proceed for 2–5 h and then quenched by dilution with BS buffer or storage at 4°C. For temperature studies, the reaction vial was placed in a water bath at 50°C during the reaction. Aliquots (5 μl) were taken at different time intervals, diluted, and injected in the LIF-CE system to obtain a reaction profile.

3. Results and discussion

3.1. Detection scheme

The use of the sheath flow cuvette for post-column detection has been described previously [6]. The main advantages of this detector are the reduction of light scattering and hydrodynamic focusing of fluorescent species coming from the capillary. Selective transmission of fluorescence to the photomultiplier is obtained by blocking Raleigh and Raman scattering with interference filters. CBQ labeled amino acids have maximum absorption at 466 nm. At first glance, it seems that the 465.8 nm argon ion laser line is ideally suited for excitation. However, the strongest Raman band for the 465.8-nm argon ion line spans from 544 to 563 nm, which overlaps the fluorescence emission spectrum of CBQ derivatives. Raman scatter will produce a high background signal for these derivatives when excited at the absorbance maximum. Instead, we excite the CBQ derivative with the 488.0-nm argon ion laser line. With this line, the main Raman band (575–596 nm) is shifted to the red with respect to the fluorescence emission. By selecting an appropriate interference filter, Raman scattering is nearly eliminated, producing a low background signal and allowing detection of minute amounts of CBQ derivatives.

Using the detection scheme mentioned above and an optimized labeling reaction (discussed below) we find that the limit of detection (3σ) of the CBQ–arginine derivative is 9 ± 4 zeptomoles ($n = 5$). In terms of concentration, the detection limit is $(2.6 \pm 1.0) \times 10^{-11}$ M. The variation in detection limits represents a realistic situation because it is based on measurements performed over a three-month period, with different capillaries and injecting different amounts of the CBQ–arginine derivative (from 0.35 to 3.5 amol).

These detection limits are at least 150 times better than the previously reported value of 1.4 amol for a CBQ–amino acid derivative [10]. The detection limits calculated here assume that the yield of the labeling reaction is 100%, which is not expected to be the case. These detection limits must be taken as a conservative value.

3.2. Labeling reaction

The second aspect to consider for LIF-CE detection of CBQ–amino acid derivatives deals with the labeling reaction. Standard protocols are devised for relatively high amino acid concentrations, (i.e. 10^{-2} M to 10^{-6} M). If the concentration of an amino acid to be analyzed is extremely low, use of the standard protocol results in the formation of undetectable amounts of CBQ derivatives. Factors involved in the labeling reaction such as reaction mechanism, kinetics, secondary reactions, temperature dependence, pH dependence need to be considered.

The optimum pH for the formation of the CBQ derivative is related to the pK_a of the amino group, since the latter has to be unprotonated for the reaction to occur. The reaction efficiency is highest at high pH. For arginine, the labeling reaction efficiency was compared for phosphate buffer pH 9.0, pH 8.0 and methanol. The best pH seems to be 9.0, as shown in Table 1.

Despite the fact that pH 9 is better for CBQ labeling of arginine, it was decided to use methanol as the solvent for the labeling reaction. If pH 9 buffer was selected for the labeling reaction, the solution will a require high ionic strength to counteract pH changes due to cyanide hydrolysis. For concentrations close to the detection limit of the CBQ–amino acid derivative, the corresponding fluorescent signal would be weak; little or no dilution is possible prior to injection into the capillary. An electrokinetic injection of a sample having much higher ionic strength than the buffer would have an electropherogram showing anomalous baseline variations around the elution window.

Fig. 2 shows an example of an electropherogram of the derivatization of arginine with CBQ when 10^{-7} M arginine was used in the labeling reaction. After a 100-fold dilution, 0.35 amol was injected. Several peaks are noticed. Peak a is the CBQ–arginine derivative, peak d is associated with underivatized CBQ (0.4 mM). Other peaks result from secondary reactions of CBQ and cyanide.

Table 1
Effect of pH on CBQ–arginine derivative signal

pH	Peak height (average ± S.D.) ($n=4$)
9.0	0.051 ± 0.005
8.0	0.034 ± 0.004
Methanol	0.018 ± 0.003

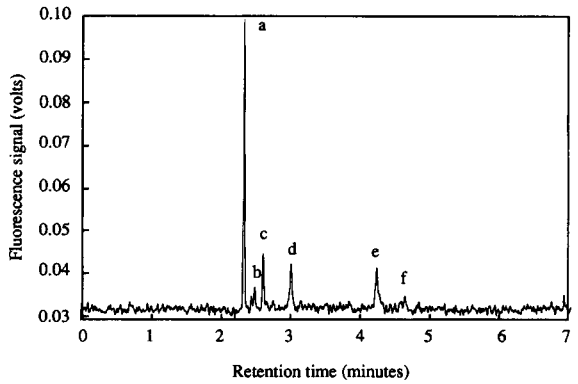

Fig. 2. Electropherogram of the CBQ derivative of arginine. Peak a corresponds to the CBQ–arginine derivative; peak d corresponds to CBQ alone; other peaks correspond to products of the secondary reactions between CBQ and CN^-. Labeling reaction: 10^{-7} M arginine, 2.0 mM CN^-, 4.0 mM CBQ; 5.5 h. Injection: 0.35 amol (5 s, 5000 V, 100-fold dilution of reaction preparation). Separation: 10 mM borate + 10 mM SDS, pH 9.3 buffer; 400 V cm^{-1}; 10 μm I.D., 49.3 cm long capillary.

At 50°C, the yield of the labeling reaction improves slightly and the reaction time to reach a maximum signal shortens compared with room temperature reaction. At 50°C, the fluorescence signal reaches a plateau in less than 1 h. At room temperature, the same reaction takes about 5 h to produce a similar response, Fig. 3.

Understanding the mechanism for the labeling reaction of an amino acid with CBQ could suggest ways of improving the reaction yield and eliminate secondary reactions. In Fig. 4, a mechanism is proposed for the CBQ labeling reaction of an amino acid based on reaction mechanisms of OPA and NDA [7–9]. First, CBQ (I) and the amino acid react to form an imino intermediate (II). In principle, the reaction is of first order with respect to CBQ and amino acid. Second, the imino intermediate is attacked by a nucleophile, CN^- in this case. Elimination of water leads to the formation of an isoindole ring (III) responsible for the fluorescent properties of the derivative. If the reaction is considered first order with respect to CBQ, high concentrations of CBQ should increase the rate of formation of the imine intermediate, which would increase its concentration. It is found that the fluorescent signal increased up to 4

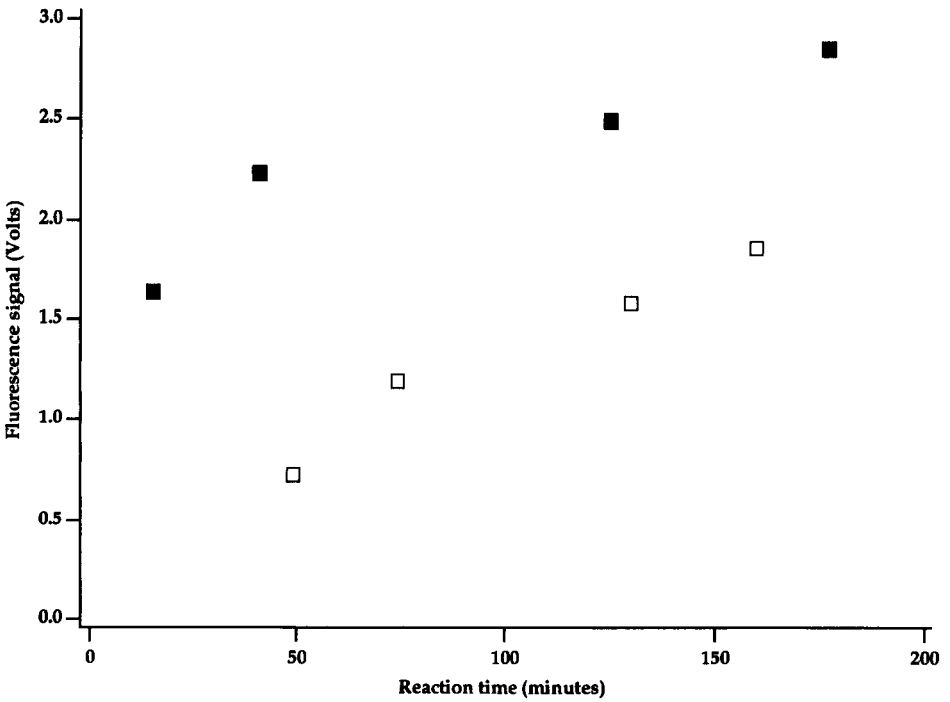

Fig. 3. Comparison of the CBQ labeling reaction at (■) 50°C and (□) room temperature. Labeling reaction: 10^{-4} M arginine, 2.0 mM CN^-, 4.0 mM CBQ, pH 9.0. Injection: 5 s, 1000 V, 500-fold dilution of reaction preparation. Separation as in Fig. 2.

mM CBQ; higher concentrations of CBQ resulted in weaker fluorescence. If the nucleophilic attack by cyanide shows first order kinetics, then the formation of the next two intermediates would be favored by increasing the concentration of cyanide. Using 2 mM CN^- the fluorescence signal reaches a plateau and higher concentrations do not improve the yield.

Using those optimized conditions, 10^{-7} M arginine can be labeled and detected, Fig. 2. The log of standardized fluorescent signal (corrected for dilution) versus the log of arginine concentration shows a linear behavior over the range 10^{-3}–10^{-4}, with a log–log slope of 0.95 and correlation coefficient of 0.985. An extrapolation of the curve predicts that 1.8×10^{-11} M arginine would produce a fluorescent signal equal to three times the standard deviation of the background.

This optimistic prediction could not be realized due to the presence of other fluorescent species resulting from the reaction between CN^- and CBQ, Fig. 5. Under alkaline conditions, aldehydes and ketones react rapidly with cyanide to form cyanohydrins [15]. Fig. 4 shows one of the possible products of CBQ and cyanide. The existence of this secondary reaction is confirmed by reacting cyanide and CBQ prior to the addition of the amino acid. No amino acid derivative is observed if this order of addition of reagents is followed. Another explanation for the fluorescent species could be the presence of impurities with amino groups in the water used for the preparations. However, we found no difference between different sources of water or when all reagents used in the labeling reaction were prepared in methanol.

The association of cyanide with the various peaks in the electropherogram was confirmed by reducing the cyanide concentration in the labeling reaction. The result, as expected, were background peaks of decreased intensity. The intensity of these background peaks also decreases when the concentration of amino acid is increased, which suggests a competition between the amino acid and the CN^- ion. Still it is not understood if cyanohydrins fluoresce in the range of our detector even without having an isoindole ring, or if they are intermediates to the formation of other cyclic products that would fluoresce.

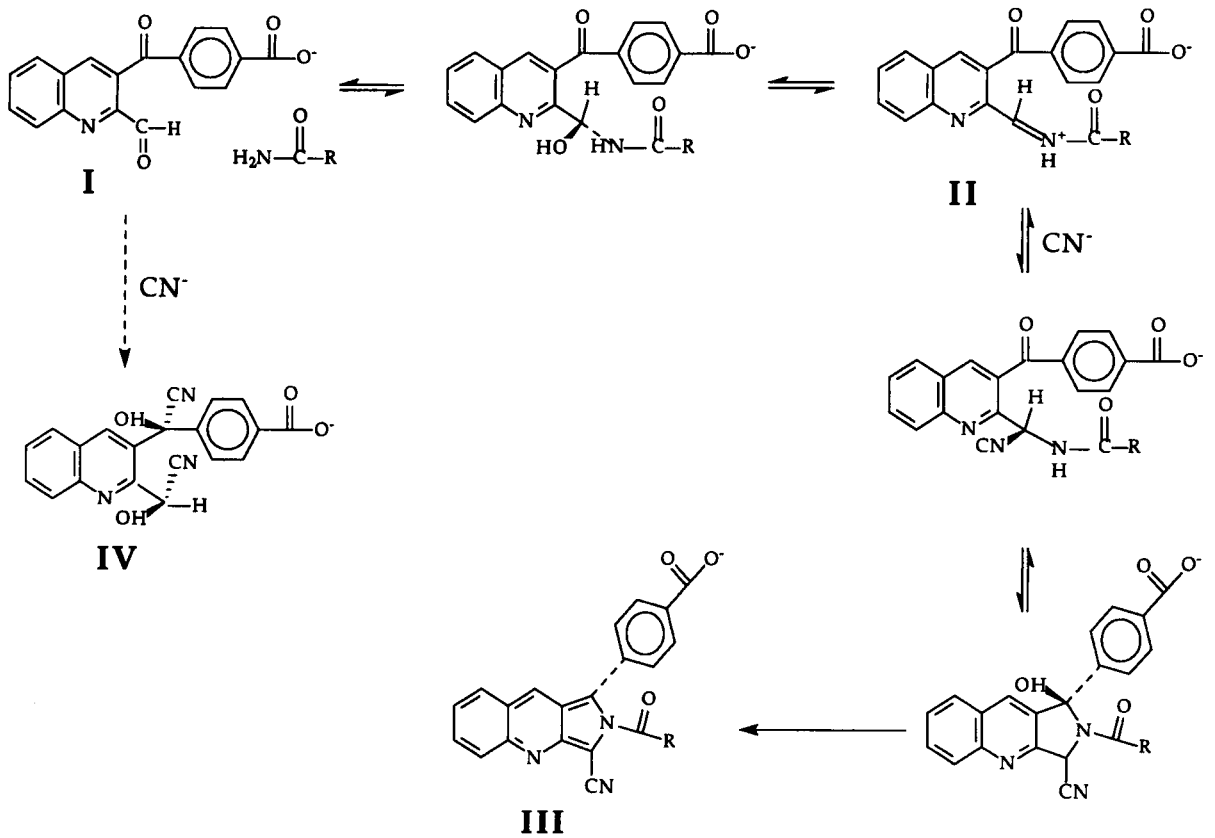

Fig. 4. Mechanisms for CBQ labeling reaction of amino acids and CBQ direct reaction with cyanide. CBQ (I) forms the imine intermediate (II); the formation of the intermediate is favored by slightly acidic conditions; (II) reacts with cyanide (basic conditions) to form the CBQ derivative (III). Direct reaction of CBQ with cyanide would favor the formation of a cyanohydrin (IV); different degrees of substitutions and orientations could be expected.

3.3. *Future directions*

LIF-CE detection of CBQ–amino acid derivatives and other biomolecules with amine functionalities could benefit from further improvements in both the detection scheme and the labeling reaction.

The detection scheme could be improved by taking full advantage of our two-channel instrument. A simpler filter system consisting of a single spectral channel would allow the collection of fluorescence in a wider wavelength range while still blocking the 575–595 nm water Raman band. A second approach to improve the sensitivity would be to optimize the laser power for the CBQ–arginine derivative; the photobleaching properties of these derivatives have not been reported.

The derivatization reaction could be improved by considering the sequence of events in the reaction mechanism. For example, the formation of the imine intermediate is favored under slightly acidic conditions, while its attack by cyanide is favored in an alkaline medium. We would expect fewer secondary reaction products and possibly higher yields if the derivatization is done in two steps: an incubation step in an acidic medium (formation of the imine intermediate), and a controlled nucleophilic (cyanide) attack at higher pH.

In conclusion, we have been able to lower the detection limits of CBQ-derivatized amino acid by using a sheath flow cuvette as a post column detector with 488 nm excitation wavelength. This is the first report of an amino acid labeled with a fluorogenic reagent that shows a detection limit comparable to the amino acid

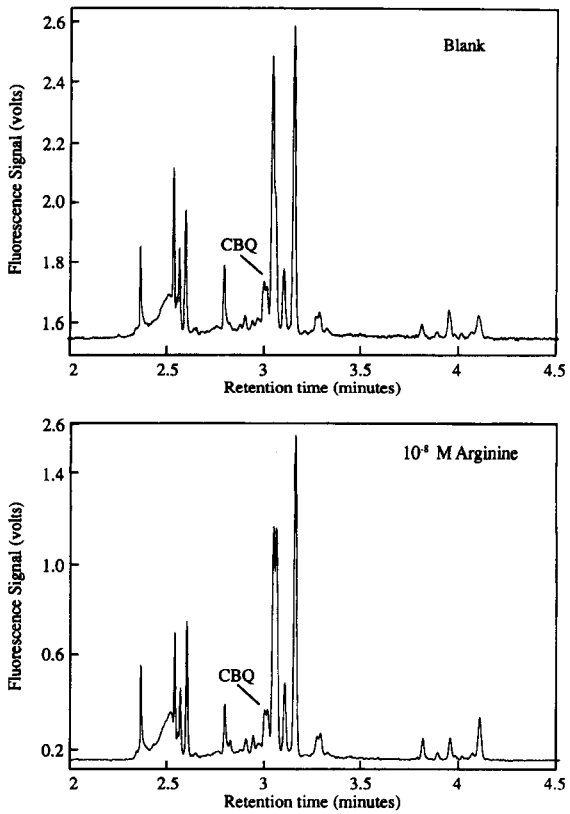

Fig. 5. Electropherograms of the CBQ labeling reaction of 10^{-8} M arginine and its corresponding blank. All peaks are related to cyanide secondary reactions between CBQ and cyanide. The exception is the peak labeled CBQ that corresponds to 0.4 mM CBQ, the concentration expected in a 10 fold diluted sample. Labeling reaction: 10^{-8} M arginine, 2.0 mM CN^-, 4.0 mM CBQ; 5.5 h. (In blank arginine was replaced by deionized water). Injection: 5 s, 2000 V, 10 fold dilution). Separation: 10 mM Borate + 10 mM SDS, pH 9.3 buffer; 400 V cm^{-1}; 50 μm i.d., 41.5 cm long capillary.

derivatives of tetramethylrhodamine and fluorescein. Most importantly, we have improved the minimum concentration of an amino acid that could be derivatized.

Acknowledgements

This project was supported by the Natural Sciences and Engineering Research Council of Canada (NSERC). YZ acknowledges a graduate fellowship from the Alberta Heritage Foundation for Medical Research. NJD acknowledges a Steacie Fellowship from NSERC.

References

[1] D.Y. Chen and N.J. Dovichi, J. Chromatogr., 657 (1994) 265–269.
[2] Y.F. Cheng and N.J. Dovichi, Science, 242 (1988) 562–564.
[3] J.Y. Zhao, D.Y. Chen and N.J. Dovichi, J. Chromatogr., 608 (1992) 117–120.
[4] K.C. Waldron, S. Wu, C.W. Earle, H.R. Harke and N.J. Dovichi, Electrophoresis, 11 (1990) 777–780.
[5] G. Ogden and P. Földi, LC·GC, 5 (1987) 28–40.
[6] S. Wu and N.J. Dovichi, J. Chromatogr., 21 (1989) 143–155.
[7] L.A. Sternson, J.F. Stobaugh and A.J. Repta, Anal. Biochem., 144 (1985) 233–246.
[8] B.K. Matuszewski, R.S. Givens, K. Srinivasachar, R.G. Carlson and T. Higuchi, Anal. Chem., 59 (1987) 1102–1105.
[9] P.D. Montigny, J.F. Stobaugh, R.S. Givens, R.G. Carlson, K. Srinivasachar, L.A. Sternson and T. Higuchi, Anal. Chem., 59 (1987) 1096–1101.
[10] J. Liu, Y.Z. Hsieh, D. Wiesler and M. Novotny, Anal. Chem., 63 (1991) 408–412.
[11] J. Liu, O. Shirota and M. Novotny, Anal. Chem., 63 (1991) 413–417.
[12] S.C. Beale, Y.Z. Hsieh, D. Wiesler and M. Novotny, J. Chromatogr., 499 (1990) 579–587.
[13] S.C. Beale, J.C. Savage, D. Wiesler, S.M. Wieststock and M. Novotny, Anal. Chem., 60 (1988) 1765–1769.
[14] E.S. Yeung and M.J. Sepaniak, Anal. Chem., 53 (1980) 1465A–1481A.
[15] J. McMurry, Organic Chemistry, Brooks/Cole, Monterey, 1984.

ELSEVIER

Analytica Chimica Acta 299 (1995) 327–332

ANALYTICA CHIMICA ACTA

Application of the glass slab optical waveguide to the spectrophotometric determination of the iron(II)–1,10-phenanthroline complex by flow analysis

Kin-ichi Tsunoda *, Hiromitsu Itabashi, Hideo Akaiwa

Department of Chemistry, Gunma University, Tenjin-cho, Kiryu, Gunma 376, Japan

Received 17 January 1994; revised manuscript received 16 June 1994

Abstract

A slab optical waveguide (SOWG) absorption detector was applied to the determination of the orange-red Fe(II)–1,10-phenanthroline complex $\{[Fe(phen)_3]^{2+}\}$ by flow analysis. When a sample solution containing $[Fe(phen)_3]^{2+}$ was introduced into a flow of sodium dodecylbenzene sulphate (DBS^-) solution, an ion pair of $[Fe(phen)_3]^{2+}$ and DBS^- was formed in a mixing coil, and was then adsorbed on the glass SOWG. The adsorbed ion pair caused the attenuation of light of a green He–Ne laser (543.5 nm) or of an Ar ion laser (multi-line, mainly 488 nm and 515 nm). The best sensitivity was obtained with a glass SOWG fabricated by a radio frequency sputtering method, which was 9.5 times higher than that with a conventional spectrophotometer (1-cm cell) for a 0.5-ml sample solution.

Keywords: Flow analysis; Glass slab optical waveguide; Iron(II); Lasers; 1,10-Phenanthroline; Spectrophotometry

1. Introduction

A slab optical waveguide (SOWG), which is one of the most important devices in opto-electronics, has also been recognized by spectroscopists as a useful tool for highly sensitive spectroscopic measurement of a thin film and its surface [1–4]. Moreover, the SOWG has been applied recently to opto-chemical sensors [5–8] and opto-biosensors [9–11].

We have been studying the application of the SOWG as an absorption cell for flow analysis. In principle, the SOWG absorption detector responds only to chromophores adsorbed on the SOWG surface, while the sample matrix scarcely interferes with the SOWG measurements. Thus, the SOWG could be a highly sensitive and selective absorption detector. In previous studies, a potassium ion doped glass SOWG provided one to two orders of magnitude higher sensitivity than conventional absorption measurements of an analyte on the SOWG surface in which perpendicular irradiation of source light is applied. Moreover, the surface of the SOWG was modified with octadecylsilane (ODS) to concentrate analytes on the SOWG through hydrophobic interaction between the analytes and ODS. The ODS–SOWG was applied to the spectrophotometric detection of the blue dyes Coomassie Brilliant Blue G-250 and Methylene Blue by flow analysis [12,13].

In this paper, the above approach was extended to the spectrophotometric detection of the orange-red iron(II)–1,10-phenanthroline complex $\{[Fe(phen)_3]^{2+}\}$ by flow analysis for the purpose of eval-

* Corresponding author.

SSDI 0003-2670(94)00323-8

uating its applicability to spectrophotometric determination of trace $[Fe(phen)_3]^{2+}$ in solution.

2. Experimental

2.1. Fabrication of glass SOWG

Potassium ion doped glass SOWG. Potassium ion doped SOWGs (K^+SOWG) were fabricated by an ion-exchange process on commercial soda-lime slide glasses in molten potassium nitrate at 673 K for 30 min [3,12,13]. The SOWG supported only one mode of the guiding light [13]. Octadecylsilane was then introduced onto the surface of the SOWG by the procedure of Kingston and Gerhart, with minor modification [12,14].

Radiofrequency-sputtered glass SOWG. A Corning 7059 glass target was sputtered and the film was deposited on a quartz glass substrate (25 mm×75 mm×2 mm, refractive index (RI): $n_D = 1.459$) with an ordinary radiofrequency (RF) sputtering method [15–17]. The Corning 7059 glass, $n_D = 1.530$, was purchased as a polished 80 mm diameter, 1.1 mm thick circular target, installed in a custom-made RF sputtering apparatus (Vieetech Japan) and sputtered at 200 W forward RF power (27.13 MHz) for 10 h. The partial pressures of the working gases, oxygen and argon, were 5 and 15 mTorr, respectively. The deposition rate was estimated to be ca. 6.3 nm min^{-1}. This SOWG supported four modes of the guiding light.

2.2. Measurement system

The schematic diagram of the flow system is shown in Fig. 1. The SOWG detector used in this study was basically the same as that in the previous papers [12,13], except that a green He–Ne laser (543 nm, 0.75 mW, and random polarization) or an argon ion laser (multi-line, Model GLG3100, NEC, Japan) was used as a light source. The flow cell was placed on the SOWG with a polytetrafluoroethylene (PTFE) block and a PTFE spacer (0.2 mm thick). The physical cell length was 1.5 cm, and the cell volume was 9 μl, unless otherwise stated. Distilled water as a carrier and a sodium dodecylbenzene sulphate (DBS^-) solution (0.4 mmol l^{-1}) were pumped with an SNK DMX-2300T double plunger pump (Sanuki Industry, Japan) at 0.75 ml min^{-1}. Five hundred microliters of the color-developed $[Fe(phen)_3]^{2+}$ solution were introduced into the carrier stream via a Rheodyne 5020 loop injector (Cotati, CA). The mixing coil was ca. 50 cm long.

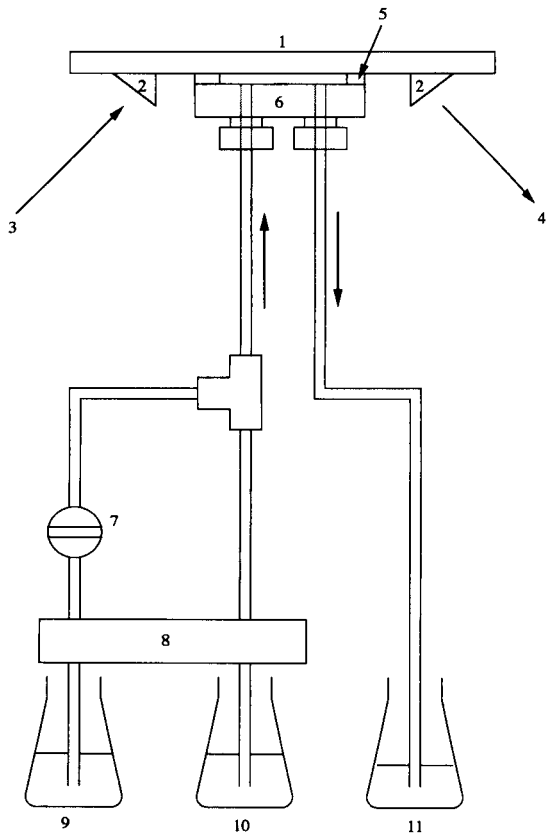

Fig. 1. Schematic diagram of the experimental system. (1) Glass slab optical waveguide; (2) coupling prism; (3) laser light; (4) detector; (5) spacer; (6) PTFE cell block; (7) sample injector; (8) pump; (9) distilled water; (10) DBS^- solution (0.4 mmol l^{-1}); (11) mixing coil; (12) waste.

2.3. Preparation of $[Fe(phen)_3]^{2+}$ solution

Twenty-five milliliters of a standard iron(III) solution (from 0.4 to 3.2×10^{-4} mol l^{-1}), 1 ml of a 10% hydroxylamine solution, 10 ml of a 10% sodium acetate solution and 10 ml of a 0.1% 1,10-phenanthroline solution were mixed in a 100-ml volumetric flask. The mixture was allowed to stand for 5 min, and then diluted to the mark.

2.4. Calculation of relative sensitivity (S)

The relative sensitivity (S) is a ratio of the sensitivity of the SOWG technique (physical cell length 1 cm) to that of light absorption with perpendicular irradiation for adsorbed analytes onto the SOWG surface [1,13]. In order to obtain the S value of the SOWG for each mode of the guiding light, the vertical RI profile of the rf-sputtered glass SOWG was estimated with an inverse WKB method [18], then the penetrating depth (d_p) of the evanescent wave from the SOWG surface into the solvent was calculated with the RI profile and the incident angle of the guiding light to the SOWG [19]. Moreover, the effective path length (L_{eff}) was experimentally obtained with a standard bromothymol blue solution [4,13]. The S value was obtained from $S = L_{eff}/d_p$.

3. Results and discussion

3.1. Optimization of the measurement system for $[Fe(phen)_3]^{2+}$ detection

The optimization of the experimental conditions was made with the K^+SOWG and the green He–Ne laser as a light source. Although the surface of the SOWG is negatively charged due to slightly dissociated silanol groups, adsorption of $[Fe(phen)_3]^{2+}$ was not observed at all with the standard $[Fe(phen)_3]^{2+}$ solution alone. Thus, the utilization of the ion-pair formation between $[Fe(phen)_3]^{2+}$ and an anion surfactant was investigated as well as in the case of the Methylene Blue measurement [13]. Sodium dodecylbenzene sulphate (DBS^-) and sodium lauryl sulphate (LS^-) were tested as counter ions. When the $[Fe(phen)_3]^{2+}$ solution (8×10^{-5} mol l^{-1}, 0.5 ml) and the anion surfactant solution were mixed in a syringe and injected into a carrier stream of distilled water (0.75 ml min^{-1}) via a silicone-rubber septum (the same flow system as that in [12] and [13]), considerable amounts of the ion pair were adsorbed onto the SOWG. As DBS^- gave slightly better sensitivity than LS^-, DBS^- was used throughout the following experiments. The formation of an 1:2 ion pair between $[Fe(phen)_3]^{2+}$ and DBS^- was confirmed by the mole-ratio method with a conventional spectrophotometer. The best sensitivity was obtained with about 0.2 mmol l^{-1} of DBS^-. A slight decrease in the absorption signal was observed in the higher concentration range of DBS^-, which might be due to the formation of charged species such as 1:3 or 1:4 ion associates. Thus, the DBS^- concentration of the stream was set at 0.2 mmol l^{-1} in the following experiments. The effects of flow-rate, cell volume, and sample volume on the absorption signal with the SOWG detector were also examined. The greater the flow-rate and the smaller the cell volume the higher the sensitivity, although these effects were not very marked. The absorption signal (peak hight) increased almost proportionally along with increasing sample volume (Fig. 2). This means that the analyte is concentrated and detected on the SOWG at the same time. Although 0.5 ml of sample was applied in the following experiments, further concentration of the ion pair should easily be achieved.

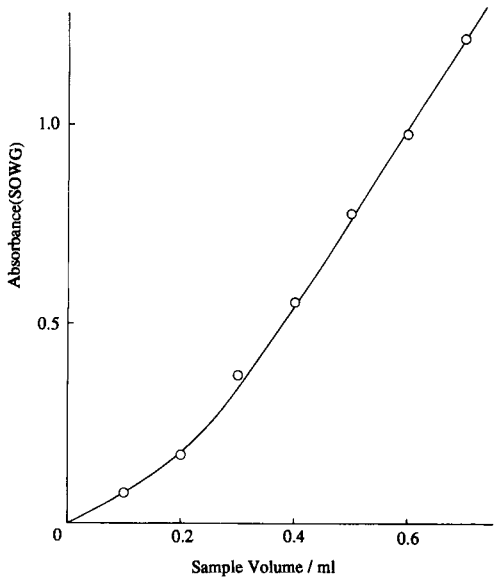

Fig. 2. Dependence of absorbance upon sample volume. $[Fe(phen)_3]^{2+}$: 8×10^{-5} mol l^{-1}; DBS^-: 0.2 mmol l^{-1}. Absorbance (SOWG) means the peak height absorbance of $[Fe(phen)_3]^{2+}$ by the SOWG detector in flow analysis.

3.2. Flow analysis of $[Fe(phen)_3]^{2+}$ with the SOWG detector

The relation between two values of absorbance for $[Fe(phen)_3]^{2+}$ solution measured by conventional spectrophotometry and the present method is shown in Fig. 3. The green He–Ne laser was used as a light

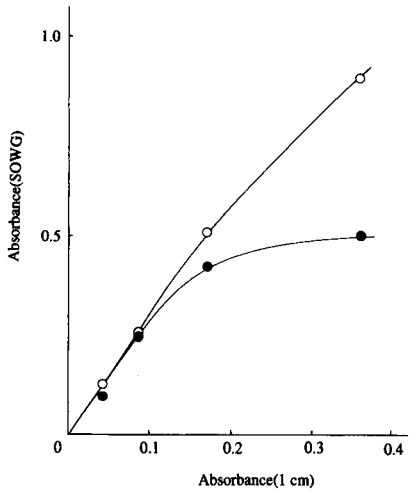

Fig. 3. Relation between two values of absorbance for $[Fe(phen)_3]^{2+}$ solution with conventional spectrophotometer and SOWG detector. (●) K^+SOWG; (○) ODS-K^+SOWG. A green He–Ne laser (543 nm) is used as a light source. Samples are the same as those in Fig. 4. Absorbance (1 cm) means the absorbance of the samples obtained with a conventional spectrophotometer. See Experimental section for further details.

source. The octadecylsilane-coated K^+-doped SOWG (ODS-K^+SOWG) was also applied to the measurement of $[Fe(phen)_3]^{2+}$. Although almost the same sensitivity was obtained by the K^+SOWG and the ODS-K^+SOWG in the lower concentration range, the ODS-K^+SOWG was superior to the K^+SOWG in the linearity of the plot in Fig. 3. Similar results have also been observed in previous work on the detection of blue dyes [12,13]. The ion pair of $[Fe(phen)_3]^{2+}$ and DBS^- might be partitioned to the ODS phase of the SOWG as in ion-pair reversed phase liquid chromatography. Fig. 4 shows the signal profiles of the $[Fe(phen)_3]^{2+}$ measurements with the ODS-K^+SOWG. The light is absorbed when the sample solution passes through the SOWG detector. Then the adsorbed ion pair was desorbed and the signal returned to the baseline.

3.3. Application of an RF-sputtered glass SOWG

An RF sputtering method is one of the most common methods of fabricating glass SOWGs, in which the thickness and the RI value of the guiding layer can be easily controlled [15–17]. As SOWGs with a thinner guiding layer and a greater Δn (difference in RI between guiding layer and substrate) would provide higher sensitivity in absorption measurements [13], this method was applied to fabricate glass SOWGs to improve the sensitivity. Because Corning 7059 glass has a relatively high RI and shows minimal background fluorescence, it has often been used as a target, and this glass SOWG has been applied to Raman and fluorescence spectroscopy by several researchers [16,17]. However, as it has not been evaluated as an absorption detector, the Corning 7059 SOWG was fabricated and applied to the $[Fe(phen)_3]^{2+}$ measurements.

As the attenuation of the guiding light was considerably greater in the Corning 7059 SOWG than in the K^+SOWG probably due to light scattering by the guiding layer, an Ar ion laser (mainly 488 nm and 515 nm, total output 10 mW) was used as a light source, and the physical cell length was set at 1.0 cm. Table 1 summarizes both the characteristics of the K^+SOWG and the Corning 7059 SOWG as an absorption cell, and the analytical data on the $[Fe(phen)_3]^{2+}$ measurements. In this SOWG, four modes of the guiding light can be observed: the TM_3 mode gave the best sensitivity, which was 9.5 times higher than the conventional method with 0.5 ml of sample. Further enhancement of the signals will easily be achieved with increase in the sample volume, as shown in Fig. 2. Although the TM_3 mode of the Corning 7059 SOWG should be 12.3 times as sensitive as the K^+SOWG according to their relative sensitivities (S), the former showed 7.7 times higher sensitivity than the latter for the $[Fe(phen)_3]^{2+}$ measurements as shown in this table. This discrepancy might

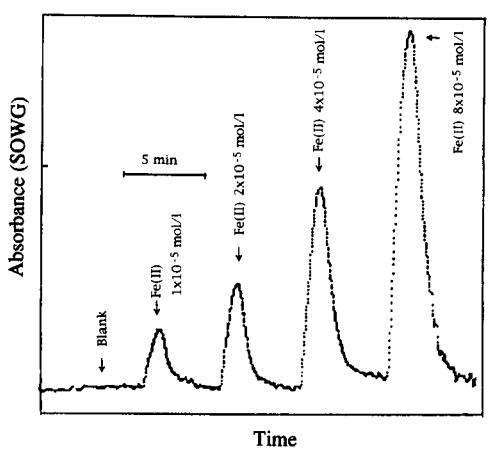

Fig. 4. Signal profile of $[Fe(phen)_3]^{2+}$ measurements. The ODS-K^+SOWG was used for the measurement. The experimental conditions are the same as those in Fig. 3.

Table 1
The characteristics of glass slab optical waveguides (SOWG) as an absorption cell, and the analytical data [a] for the $[Fe(phen)_3]^{2+}$ measurements

SOWG	Mode	S [b]	Sensitivity			N_a/N_s (%)
			C_s [c] (mol l^{-1})	N_s [d] (mol)	N_a [e] (mol)	
K^+SOWG	TM_0	160 (1.0)	5.3×10^{-7}	2.7×10^{-10} (1.0)	1.3×10^{-12}	0.47
Corning 7059	TM_0	–	8.8×10^{-7}	4.4×10^{-10} (0.6)	–	–
SOWG	TM_1	200 (1.3)	3.4×10^{-7}	1.7×10^{-10} (1.6)	1.0×10^{-12}	0.59
	TM_2	960 6.0)	1.9×10^{-7}	0.9×10^{-10} (3.0)	2.1×10^{-13}	0.23
	TM_3	1960 (12.3)	0.7×10^{-7}	3.5×10^{-11} (7.7)	1.0×10^{-13}	0.29
Conventional method [f]			6.7×10^{-7}	3.3×10^{-10}		

[a] The argon ion laser (488 nm and 515 nm) was used as a light source, and the physical cell length was 1 cm. The other experimental conditions were the same as those in Fig. 3.
[b] Relative sensitivity (S) (see text). Values in parentheses are normalized by the S value of K^+SOWG.
[c] The concentration of $[Fe(phen)_3]^{2+}$ in the sample solution (0.5 ml) which gives 1% absorption.
[d] The absolute amounts of $[Fe(phen)_3]^{2+}$ in the sample solution (0.5 ml) which gives 1% absorption. Values in parentheses are inversely normalized by the N_s value of K^+SOWG.
[e] The absolute amounts of $[Fe(phen)_3]^{2+}$ adsorbed onto the SOWG surface which gives 1% absorption. This value is calculated from $N_a = 0.0044a_s/(\epsilon S)$ in which a_s = area of the SOWG surface in the flow cell (3 mm × 10 mm = 3.0×10^{-4} dm^3 cm^{-1}), ϵ = molar absorptivity of the analyte (dm^3 mol^{-1} cm^{-1}) and S = relative sensitivity [12].
[f] With a conventional spectrophotometer (1-cm cell). A sample volume of 0.5 ml was postulated.

be ascribed to the difference in the surface nature between these glass SOWGs. Moreover, only $<1\%$ of $[Fe(phen)_3]^{2+}$ in the sample solution seems to be adsorbed onto the SOWG surface. Similar results were obtained for the blue dyes in previous work [12,13]. Thus, further improvement in the sensitivity (C_s and N_s in the table) could be achieved if greater adsorption of analytes was achieved.

4. Conclusions

The glass SOWG can be a useful tool for the spectrophotometric determination of trace substances in solution samples. Theoretically, the fabrication of an SOWG which shows more than ten times higher sensitivity than the present SOWGs is supposed to be possible [13]. Moreover, the chemical modification of the SOWG surface will be effective for enhancing the adsorption efficiency of analytes. Thus, further improvement of the sensitivity is promised.

References

[1] J.D. Swalen, M. Tacke, R. Santo, K.E. Rieckhoff and J.F. Fischer, Helv. Chim. Acta, 61 (1978) 960.
[2] P.W. Bohn, Prog. Anal. Spectrosc., 12 (1989) 41.
[3] K. Itoh and A. Fujishima, J. Phys. Chem., 92 (1988) 7043.
[4] N.F. Fell, Jr., and P.W. Bohn, Anal. Chem., 65 (1993) 3382.
[5] M.D. Degrandpre, L.W. Burgess, P.L. White and D.S. Goldman, Anal. Chem., 62 (1990) 2012.
[6] S.S. Saavedra and W.M. Reichert, Anal. Chem., 62 (1990) 2251.
[7] C. Piraud, E. Mwarania, G. Wylangowski, J. Wilkinson, K. O'Dwyer and D.J. Schiffrin, Anal. Chem., 64 (1990) 651.
[8] K.J. Kuhn and L.W. Burgess, Anal. Chem., 65 (1993) 1390.
[9] P.M. Nellen, K. Tiefenthaler and W. Lukosz, Sensors Actuators, 15 (1988) 285.
[10] T. Hara, K. Hashimoto, K. Itoh, M. Murabayashi and A. Fujishima, in Abstracts of the 61st Annual Meeting of the Chemical Society of Japan, Yokohama, 1991, Part I, p. 3.
[11] S.J. Choquette, L. Locascio-Brown and R.A. Durst, Anal. Chem., 64 (1992) 55.
[12] K. Tsunoda, H. Itabashi and H. Akaiwa, Bull. Chem. Soc. Jpn., 65 (1992) 1581.
[13] K. Tsunoda, H. Itabashi and H. Akaiwa, Anal. Chim. Acta, 276 (1993) 133.

[14] D.G.I. Kingston and B.B. Gerhart, J. Chromatogr., 116 (1992) 82.
[15] M.C. Gupta, Appl. Opt., 29 (1990) 4310.
[16] D.S. Walker, W.M. Reichert and C.J. Berry, Appl. Spectrosc., 46 (1992) 1437.
[17] J.F. Rabolt and J.D. Swalen, in R.J. Clark and R.E. Hester (Eds.), Spectroscopy of Surfaces, Wiley, New York, 1988, pp. 1–36.
[18] J.M. White and P.F. Heidrich, Appl. Opt., 15 (1976) 151.
[19] N.J. Harrick, Internal Reflection Spectroscopy, Harrick, New York, 1987.

ELSEVIER

Analytica Chimica Acta 299 (1995) 333–336

ANALYTICA CHIMICA ACTA

Thermooptical flow-injection determination for hydrogen peroxide based on an enzymic reaction heat-induced optical beam deflection

Xing-Zheng Wu *, Hiroaki Shindoh, Toshiyuki Hobo

Department of Industrial Chemistry, Faculty of Technology, Tokyo Metropolitan University, Minami-Ohsawa, Hachioji, Tokyo 192-03, Japan

Received 27 December 1993; revised manuscript received 15 February 1994

Abstract

A novel thermooptical flow-injection method for hydrogen peroxide determination is proposed, based on immobilized enzymic (catalase) reaction heat-induced optical beam deflection. A glass tube, whose one end is attached with a thin gold film on which the catalase is immobilized, is used as a reaction cell. The reaction cell is immersed into a CCl_4 phase where a probe beam is passed through. Hydrogen peroxide solution is injected into the stream of sodium phosphate buffer solution (pH 7.4) flowing into the reaction cell. The reaction heat of the decomposition reaction of H_2O_2 catalyzed by the immobilized catalase induces a deflection of the probe beam. The immobilization of catalase by crosslinking with bovine serum albumin is optimized to obtain a maximum beam deflection signal. The deflection signal is linear over the concentration range of 0.025–0.5 mol l^{-1} (40 μl injected) for H_2O_2 and the detection limit is ca. 0.025 mol l^{-1}. This thermooptical flow-injection detection system has good stability and reproducibility. The noise source is discussed and the improvements on the experimental setup are also discussed.

Keywords: Enzymatic methods; Flow injection; Hydrogen peroxide; Optical beam deflection; Lasers

1. Introduction

Various methods have been used as the detection means for enzymic analytical systems. Also, various types of sensor and biosensor have been developed by immobilization of an enzyme on a support [1]. Among them, the thermometric or calorimetric method is a universal method for monitoring and/or analyzing enzymic reaction processes, since enzymic reactions are accompanied by the enthalpy change or reaction heat. In the conventional thermometric or calorimetric method, a sample and a thermistor are usually enclosed in a temperature-controlled container [2–6]. Recently, a thermoelectric enzyme probe method where enzyme is immobilized directly on a thermopile has been developed and applied as a new type of biosensor [1,7]. Compared to the conventional thermometric or calorimetric method, the thermoelectric enzyme probe method is being paid more attention to since it needs no environmental temperature control.

* Corresponding author.

SSDI 0003-2670(94)00465-X

Very recently, we have proposed a novel thermooptical detection method based on the optical beam deflection induced by reaction heat [8]. In our proposed method, a probe beam is passed through a CCl_4 phase, above which a chemical reaction occurs in the water phase. The reaction heat is propagated to the CCl_4 phase and induces a temperature gradient. This temperature gradient generates a refractive index gradient which, in turn, deflects the probe beam. The magnitude of the deflection signal has been demonstrated to be proportional to the amount of the reactant in a batch experiment [8] as well as a flow-injection analysis (FIA) experiment [9]. It is also possible to obtain kinetic information such as the reaction rate of a chemical reaction by monitoring and analyzing the deflection signal [10]. This method has also been proved to be applicable to enzymic reaction systems by a batch experiment [11]. Coupled with the immobilization of the enzyme, it has the potential to become a novel thermooptical biosensor. Our aim here is to develop such a new type of thermooptical biosensor. As a first step, we investigate the combination of this method with an immobilized enzyme reaction. In this paper, we report a thermooptical flow-injection determination of hydrogen peroxide using immobilized catalase on a thin gold film.

2. Experimental

2.1. Experimental setup

The experimental setup is similar to that reported in our previous papers [8,9,11]; its central part is illustrated in Fig. 1. A He–Ne laser (wavelength 632.8 nm, output 1 mW) provided a probe beam. The probe beam was passed through a CCl_4 phase in a spectrophotometric cell (1 cm × 1 cm × 5 cm), and its deflection was measured by a knife-edge and a photodiode detection system. A glass tube (7 mm o.d., 6 mm i.d.), whose one end was attached with a thin gold film (thickness 0.01 mm) on which catalase was immobilized, was used as a reaction cell. The reaction cell was immersed into the CCl_4 phase, on which a water layer was placed to prevent the evaporation of the CCl_4 (Fig. 1). The distance between the probe beam and the gold film was about 1 mm. In

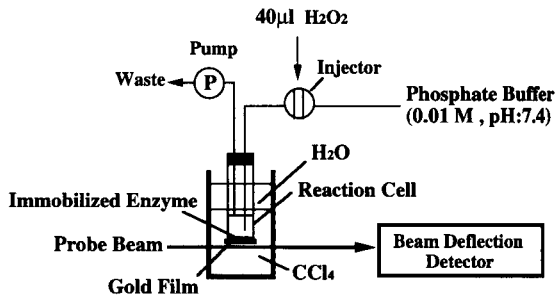

Fig. 1. Illustration of the thermooptical flow-injection determination system for hydrogen peroxide.

the batch experiment, 40 μl of H_2O_2 solution was directly introduced into the reaction cell by syringe. In the FIA experiment, the sodium phosphate buffer solution (0.01 mol/l, pH 7.4) was pumped through the reaction cell by a peristaltic pump, and H_2O_2 solution was injected into the flow line using a 40-μl injector. The distance between the injector and the flow cell was about 14 cm. A PTFE tube of 1 mm i.d. was used as the flow line.

2.2. Enzyme immobilization

10 mg of commercial bovine liver catalase and 10 mg of bovine serum albumin were first dissolved in 1 ml distilled water. Then 10 μl of 30% aqueous glutaraldehyde solution was added, and mixed rapidly. 80 μl of the resultant mixture solution was introduced into the reaction cell, which was placed under a nitrogen atmosphere. After 1 h, a thin enzyme membrane was formed on the gold film surface. The thickness of the enzyme membrane was measured by calipers, after removing the enzyme immobilized gold film from the reaction cell.

2.3. Reagents

Stock solutions of H_2O_2 were prepared by dilution of a commercial 30% solution and standardized by titration with potassium permanganate solution. Commercial bovine liver catalase (activity: 19,900 U mg^{-1} and 1000 U mg^{-1}, Sigma) and bovine serum albumin (Sigma) were used as received. All other reagents were reagent grade and used as received.

3. Results and discussions

In our previous batch experiments [11], the reaction media of the H_2O_2 decomposition reaction catalyzed by catalase was initially directly in contact with the CCl_4 phase. In that case, the reaction heat and the diffusion of the reaction product O_2 respectively induced a temperature gradient and a concentration gradient in the CCl_4 phase. Both the temperature and the concentration gradients generated deflection signals. In order to obtain only the reaction heat-induced deflection signal, the reaction medium was separated from the CCl_4 phase by a thin gold film. A quantitative relation between the reaction heat-induced deflection signal and the enzyme activity or the concentration of H_2O_2 was proved. A simple crosslinking method for immobilization of catalase on a gold film was also investigated, and the stability of the resultant enzyme biomembrane was found to be dependent on the immobilization conditions.

3.1. Optimization of catalase immobilization

Catalase is crosslinked with the protein bovine serum albumin by the bifunctional reagent glutaraldehyde [1,7]. Experimental results show that the optimum mixing weight ratio of catalase and bovine serum albumin is 1:1, at which the maximum deflection signal is obtained. The optimum thickness of the resultant enzyme biomembrane, which is proportional to the volume of the mixture solution of catalase–albumin–glutaraldehyde added into the reaction cell, is about 20 μm (corresponding to 80 μl mixture solution). The deflection signal is also affected by the activity of catalase. Fig. 2A, B shows the deflection signal obtained in a batch experiment for the immobilized catalases with 19,000 and 1000 activity U mg^{-1}, respectively. For the catalase with the higher activity, the deflection signal reaches the maximum soon after the addition of H_2O_2. In contrast, the deflection signal reaches the maximum at about 20 s after the addition of H_2O_2 for the lower activity catalase. Fig. 2 suggests that the reaction rate of the enzymic H_2O_2 decomposition with the higher activity enzyme is faster than that with the lower one [10].

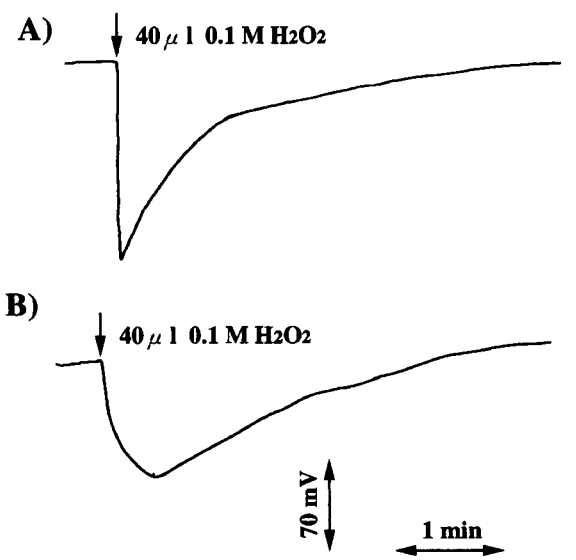

Fig. 2. Deflection signals obtained in a batch experiment with enzyme immobilized on a gold film. Activities of the immobilized enzyme are 19,000 and 1000 U mg^{-1} for A and B, respectively.

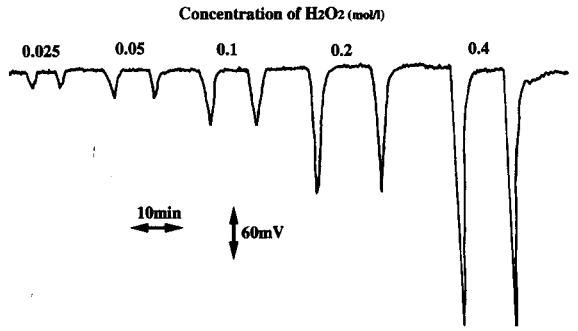

Fig. 3. Relation between the deflection signal and the injected concentration of H_2O_2. The injected volume is 40 μl.

3.2. Detection limit and sensitivity

In FIA experiments, since the noise caused by the flow pulsations of the peristaltic pump increases with the flow rate, the signal-to-noise (S/N) ratio is better at low flow rates. At a flow rate of 1.6 ml min^{-1}, the relation between the deflection signal and the concentration of H_2O_2 is investigated, and the results are shown in Fig. 3. The signal has a good linear relation with the concentration of H_2O_2. The detection limit (2a) is about 0.025 mol l^{-1}, and the linear dynamic range is about 0.025–0.5 mol l^{-1}.

Because the volume of the reaction cell (about 1 ml) and the noise in the flow system are larger, a rather high detection limit is obtained. The smaller the volume of the reaction cell, the larger the temperature rise of the reaction medium heated by the reaction heat. Therefore, the detection limit can be lowered by using a smaller reaction cell. The larger noise caused by the flow pulsations of peristaltic pump could be decreased by using another type of pump such as a syringe pump. The fluctuation of the CCl_4/H_2O interface and the instability of the laser power are also sources of noise. A double laser beam deflection detection system, where one laser beam is used as a reference, is expected to be able to eliminate the noise. This work is in progress and the results will be reported later.

3.3. Stability and reproducibility

The stability and reproducibility of the present thermooptical flow-injection system is also investigated. In order to examine the stability and reproducibility of the system, H_2O_2 solutions were injected successively at 8 injections h^{-1} into the sodium phosphate buffer flow line (flow rate 1.6 ml min^{-1}). The signals obtained for the first injection and the 100th injection after 13 h were identical. The relative standard derivation for 20 injections of 0.5 M H_2O_2 solution was 0.93%. The activity of the immobilized catalase on the gold film was stable at least for two weeks.

4. Conclusions

A novel thermooptical FIA method for hydrogen peroxide is developed with the combination of enzyme immobilization and the reaction heat induced beam deflection. A simple immobilized method of enzyme catalase on a gold film is established. The immobilized catalase is stable in the thermooptical FIA system. The enzymic reaction heat induced deflection signal has a good linear relation with the concentration of H_2O_2 over the range 0.025–0.5 mol l^{-1}. This technique is expected to be developed as a novel thermooptical biosensor.

Acknowledgements

The present work was partially supported by a Grant-in Aid for Scientific Research No. 05855120 from the Ministry of Education, Science and Culture of Japan.

References

[1] P.W. Carr and L.D. Bowers, Chemical Analysis, Vol. 56: Immobilized Enzymes in Analytical and Clinical Chemistry, Wiley Interscience, New York, 1980.
[2] I. Satoh, S. Arakawa and A. Okamoto, Sensors Actuators, B5 (1991) 245.
[3] B. Danielsson, L. Flygare and T. Velev, Anal. Lett., 22 (1989) 1417.
[4] A. Johansson, J. Lundberg, B. Mattiasson and K. Mosbach, Biochim. Biophys. Acta, 304 (1973) 217.
[5] S. Fujieda and J. Kawahito, Thermochim. Acta, 183 (1991) 153.
[6] J. Kawahito and S. Fujieda, Thermochim. Acta, 215 (1993) 1.
[7] M.J. Muehlbauer, E.J. Guilbeau and B.J. Towe, Anal. Chem., 61 (1989) 77.
[8] X-Z. Wu, H. Shindoh, M. Yamada and T. Hobo, Anal. Chem., 65 (1993) 834.
[9] X-Z. Wu, H. Shindoh, M. Yamada, E. Kobayashi and T. Hobo, Anal. Sci., 10 (1994) 203.
[10] X-Z. Wu and T. Hobo, Anal. Chem., submitted for publication.
[11] X-Z. Wu, H. Shindoh and T. Hobo, Microchem. J., 49 (1994) 213.

ELSEVIER

Analytica Chimica Acta 299 (1995) 337–342

ANALYTICA CHIMICA ACTA

Diode laser-based concentration gradient imaging detector for capillary isoelectric focusing

Jiaqi Wu, Janusz Pawliszyn *

Department of Chemistry, University of Waterloo, Waterloo, Ontario N2L 3G1, Canada

Received 30 August 1993; revised manuscript received 5 January 1994

Abstract

A diode laser-based, real-time, universal concentration gradient imaging detector was constructed and tested for capillary isoelectric focusing (CIEF). The detector indicates sample zones by measuring refractive index gradients created by the concentration gradients of samples. An imaging detection system is the best detection approach for CIEF because all samples are focused inside the capillary column after separation. A diode laser was found to be an ideal light source for the imaging detector because of its small size, low cost, and light beam characteristics. The detector can be operated at any wavelength and does not need a high-intensity light beam. In order to focus the non-circular, non-Gaussian diode laser beam through the capillary, the optical geometry of the imaging detector was optimized. Because of the short analysis time (2–4 min), good reproducibility for determining isoelectric points, and the universality of the detector, the CIEF-imaging detector system has many possible applications, such as analysis of human hemoglobin variants and peptide mapping. This is the first report of a diode laser-based imaging detection system for analytical chemistry.

Keywords: Capillary isoelectric focusing; Diode laser; Universal imaging detection

1. Introduction

The recent rapid development of a near-infrared (IR) and visible red diode laser (670 nm) offers a promising light source for atomic and molecular spectrometry [1]. Diode lasers have many advantages over other laser devices. They are inexpensive, and have small sizes (on the order of centimetres) and a long life time (10^5 h). Diode lasers already have many applications in spectrometry, including direct and indirect absorption spectrometry [2,3], molecular fluorescence spectrometry [4], and atomic absorption and fluorescence spectrometry [5,6]. The diode laser is especially advantageous compared with conventional light sources for some instruments that require good beam-focusing capability, small size and low cost for the light source. Detectors for micro-column chromatography and capillary electrophoresis are such instruments. Capillary electrophoresis (CE) is a miniaturized separation technique performed in narrow capillaries (2–200 μm I.D.) that can separate small amounts of sample (in the pico- to nanoliter range) in only a few minutes.

A diode laser-based fluorescence detector recently developed for CE demonstrated detection limits of 0.1–100 fmol for amino acids [7]. Diode lasers do have disadvantages for use in fluorescence and absorption detectors. Their wavelength is restricted to the near-IR range. The current shortest practical wavelength is 670 nm. Few molecules are fluorescent in this region. The

* Corresponding author.

SSDI 0003-2670(94)00312-2

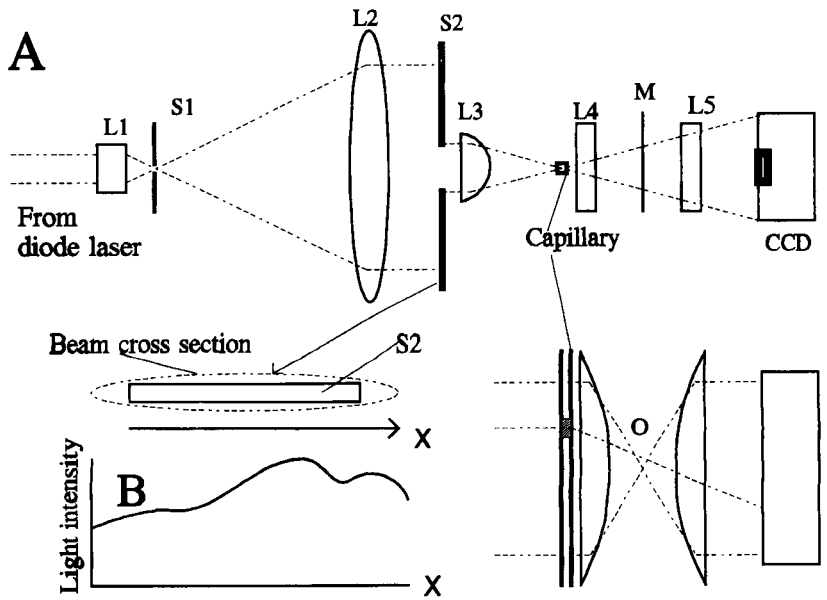

Fig. 1. (A) Optical alignment of the diode laser-based concentration gradient imaging detector. L1 is a ten-fold magnification microscopic objective lens, L2 is a 25-cm focal length lens, L3 is a 5-cm focal length cylindrical lens, L4 and L5 are 8-cm focal length cylindrical lens, S1 is a 50-μm-diameter pinhole and S2 is a 27 mm × 10 mm slot. O is the focal point of the L4 lens. (B) Diode laser beam intensity profile at S2.

power of a diode laser is lower than that of other lasers, which results in lower sensitivity for fluorescence detectors with a diode laser [7] because the sensitivity is proportional to the intensity of the light source. The sensitivities of fluorescence and absorption detectors also depend on the wavelength of the light source, so the temperature of a diode laser must be strictly controlled in the detectors because its wavelength may change with temperature.

Diode lasers may be ideal, however, for applications in which beam intensity and stability of wavelength of the light source are not critical. A concentration gradient detector, which detects samples by measuring the refractive index gradients created by sample concentration gradients, can work at any wavelength, and does not require a high-intensity light source. A diode laser-based concentration gradient on-column detector has been successfully applied to CE detections [8,9]. Its detection limit was good (low-femtomole level) [10] because of the low pointing noise of a diode laser [8].

Capillary isoelectric focusing (CIEF), one of CE separation modes, is able to resolve proteins and peptides that differ in isoelectric point (pI) by less than 0.01 pH units [11]. When a voltage is applied to two ends of a capillary filled with carrier ampholytes and protein or peptide samples, a pH gradient is formed along the capillary by stacking of the ampholytes. At the same time, proteins and peptides migrate to the points inside the capillary where their pI values are equivalent to the pH, creating discrete narrow zones (50–200 μm in width). High concentration gradients are generated by the narrow zones, which makes the concentration gradient sensor a sensitive detector for CIEF.

Because the zones are static inside the capillary, the best detector for CIEF is an on-line imaging system. Our group has developed two kinds of imaging detectors for CIEF: an absorption imaging detector [12] and a universal concentration gradient imaging detector [13,14]. For both detectors, the light source used has been an argon ion laser, a He–Ne laser, or a halogen lamp. This paper reports the development of an inexpensive, universal CIEF concentration gradient imaging detector which uses a diode laser as the light source.

2. Experimental

2.1. Apparatus

The optical alignment shown in Fig. 1 and capillary cartridge were similar to those of previous experiments [15].

An 100-μm-I.D., 4-cm-long square glass capillary (Dynamics, Rockaway, NJ, USA) was used as the separation column. The capillary inner wall was coated with non-cross-linked acrylamide to eliminate electroosmotic flow [11].

The light source of the imaging detector was a 670-nm diode laser (Type 9211, Toshiba, purchased with a collimating lens and driving circuit in a single package from MWK Industries, Corona, CA, USA). It was mounted in an aluminum barrel which provided heat dissipation, and the laser was fixed on a small translation stage capable of adjustment in two directions. The power supply for the laser was a rechargeable, 6-V, 12-A h battery. An adjustable resistor was connected in series with the diode laser to control the light intensity.

The laser beam was first expanded to a big beam spot by a beam expander which consisted of a ten-fold magnification microscopic objective lens (L1), a 50-μm pinhole (S1), and a 25-cm focal length lens (L2). The central part of the beam spot was selected by passing it through a 27 mm $\times$ 10 mm slot (S2). The beam was focused into the capillary by a 5-cm focal length cylindrical lens (L3) which was mounted on a three-axis stage. For alignment, the dark field method was employed [15,16]. After the beam passed through the capillary, it was focused onto an optical stop by an 8-cm focal length cylindrical lens (L4) which was mounted in the position vertical to the L3 lens. The optical stop was a 400-μm-wide, opaque line on a positive photographic film. Finally, the beam was projected by another 8-cm focal length cylindrical lens (L5) onto an 1024-pixel charge-coupled device (CCD) sensor (S3903-1024Q, Hamamatsu, Hamamatsu City, Japan). The CCD had a 25 mm $\times$ 0.5 mm sensing area, and was mounted on a two-axis stage. The distance between the L4 lens and the capillary was set to be 10 mm, and that between the L5 lens and the CCD sensor was set to be 7 mm in order to obtain the highest sensitivity [15]. This alignment monitored 25 mm of the 4-cm-long capillary.

Data was recorded using an IBM DACA board, connected to a PC-AT personal computer. To reduce the random noise, an averaging method was used. The scanning speed of the CCD was 10 Hz due to the 20-kHz maximum acquisition frequency of the IBM DACA board. For each measurement, the CCD scanned ten times in 1 s, and the averaged image of the ten scans was stored in the computer. The light intensity profile of the diode laser beam was first measured before the capillary cartridge was inserted into the alignment, and all sample images were normalized by using the profile.

2.2. Reagents

Solutions of 10 mM H_3PO_4 and 20 mM NaOH were used as the anolyte and catholyte for CIEF, respectively. All chemicals were reagent grade, and solutions were prepared using deionized water. The protein samples included trypsin inhibitor (chicken egg white, Sigma) and human hemoglobin standard (hemo control AFSC, Helena Labs., Beaumont, TX, USA). Tryptic peptides of cytochrome c (bovine heart, Sigma) were chosen for peptide mapping. Trypsin was purchased from Worthington (Freehold, NJ, USA). The trypsin digestion procedure was the same as that reported elsewhere [17]. After digestion, the products were desalted using dialysis membranes with a molecular mass cutoff of 500 against water for 6 h.

2.3. Isoelectric focusing procedures

The CIEF procedure was the same as in previous experiments [14]. The separation voltage was 4 kV for the 4-cm-long capillary. All experiments were done in triplicate to ensure reproducibility.

3. Results and discussion

During the isoelectric focusing process, proteins or peptides are focused into narrow zones at positions corresponding to their p*I* values along the capillary. For the alignment shown in Fig. 1, if there are no sample zones inside the capillary, the collimated laser beam will be focused by the L4 lens into its focal point (point O) and blocked by the stop. When the light beam passes through the capillary as shown in Fig. 1, the beam rays passing through sample zones will be deflected from their original directions and cannot be focused at point O. They will bypass the stop and reach the CCD. In this way, the beam intensity profile detected by the CCD is proportional to the derivative of the sample concentration gradient along the capillary [15].

The use of the diode laser has several benefits. The size of the imaging detector is reduced from that of the

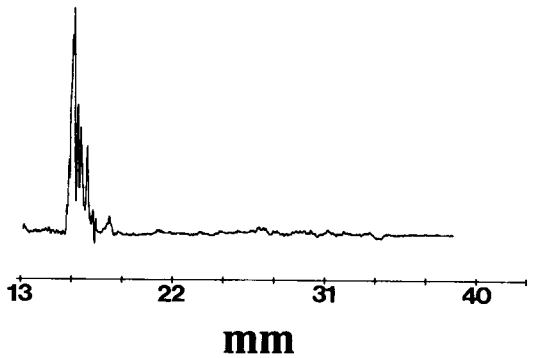

Fig. 2. Isoelectric electropherogram of trypsin inhibitor. Concentration: 100 μg/ml.

previous assembly [15] due to the small size of the diode laser. The whole light source, including driving circuit and collimating lens, is only about 8 cm in length and 2 cm in diameter. The aluminium barrel used to fix the laser provides enough heat dissipation to keep the wavelength of the laser stable. The diode laser has less pointing noise level than the He–Ne laser [10]. The battery is also a low-noise power supply for the diode laser. It can last more than 100 h for the diode laser once charged. The beam intensity of the laser can be continuously adjusted by just turning the resistor instead of using optical neutral filters for other laser devices which introduces noise in the laser beam profile. The intensity adjustment is necessary to keep the signal to reach the full scale of the CCD sensor and A/D board for different samples.

There are several problems in applying the diode laser to the imaging detector. One is its beam astigmatism. It has a non-Gaussian intensity profile, and non-circular beam cross-section, elongated in one axis as shown in Fig. 1B. Two methods were used in the imaging detector to solve the problems. The diode laser was fixed in such a position that the long axis of its beam cross-section was incident upon the capillary axis, and the beam was passed through a slot, as shown in Fig. 1, before it was focused into the capillary. In this way, the laser beam could be easily focused into the 100-μm-I.D. capillary. The uneven intensity profile of the beam was corrected by normalizing the sample images by the beam intensity profile.

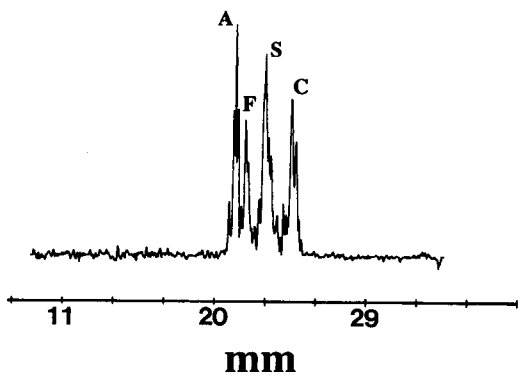

Fig. 3. Isoelectric electropherogram of standard human hemoglobin variants (A, F, S, and C). Sample is diluted 100 times.

In the UV absorption detector, the wavelength is a major factor affecting the sensitivity of the detection. For example, the best working wavelength for trypsin inhibitor is its absorption peak in the range 190–240 nm. For human hemoglobin, the best wavelength is ca. 410 nm where its absorption peak is located. Changing the wavelength over a wide range is difficult for lasers, especially for a diode laser. However, for the concentration gradient detector, although its sensitivity can be affected by changing the wavelength, especially when the wavelength of the light source is near the absorption peak of the sample, it is not an important factor [18]. Any type of sample can be detected by using a diode laser with a wavelength of 670 nm and even with a near-IR wavelength [9]. For example, Figs. 2 and 3 show the good sensitivity of this diode laser-based detector for the two proteins.

The real-time imaging detection decreases the analysis time because it combines the separation and detection into one step. The electropherogram shown in Fig. 2 was recorded 2 min after the separation voltage was turned on. The p*I* values of the separated proteins can be determined directly from their positions inside the capillary because of the use of the imaging detector and the good reproducibility of the focused pattern produced by the CIEF-imaging detector [14]. The p*I* value of the protein (the highest peak in Fig. 2) is measured to be 5.8.

Analysis of the hemoglobin variants in human blood is of major clinical interest because it is an important method for diagnosing abnormal blood in patients. Current techniques used for screening the hemoglobins are liquid chromatography (LC) [19] and CIEF methods [20]. The speed of the CIEF method (20 min per sample) is lower than that of the LC method (3 min per sample) due to the mobilization process in the CIEF method. However, the resolution of the CIEF method is much better than that of the LC method, and CIEF consumes only minute amounts of blood sample. If the

CIEF analysis speed can be increased, it will be an ideal instrument for screening hemoglobin samples. Our CIEF-imaging detector is just such an instrument. Because of the use of the short capillary and the imaging detector, analysis of a hemoglobin sample is expected to take about 2 min. The separated variants can be detected by the concentration gradient detector with the diode laser as the light source. Fig. 3 shows the electropherogram of four standard human hemoglobin variants (A, F, S, and C) detected by the diode laser-based imaging detector. The blood sample is diluted 100 times. This image is obtained in 2 min after the separation starts. Fig. 3 shows that all four variants can be resolved well by the 4-cm-long capillary column and the detector. Several low peaks in Fig. 3 may correspond to other variants of hemoglobin. The resolution for p*I* can be estimated from this electropherogram to be less than 0.02 pH, from p*I* difference of A (7.10) and F (7.15) variants, the peak width of A, and the distance between peaks A and F. From the experimental results the CIEF-imaging detector system proves to be an ideal instrument for clinical screening of blood samples.

Peptide mapping is a major tool for characterization of proteins. Reversed-phase liquid chromatography (RP-LC) is an established technique for peptide mapping [21]. However, alternative methods of peptide mapping that complement RP-LC are necessary [22]. Capillary zone electrophoresis (CZE) is one of the good alternatives owing to its high speed [22]. CIEF is another choice [23]. One of its advantages is that its separation principle is based only on p*I* differences of sample components, which is more orthogonal to RP-LC than CZE.

There are two major problems, however, in using conventional CIEF instruments for peptide mapping [23]. Owing to the UV absorption of the carrier ampholytes used in CIEF, the on-column UV absorption detectors have to be operated at a wavelength of 280 nm instead of 180–240 nm where the absorption peaks of proteins are located. Only peptides containing tyrosine and/or tryptophan have absorption at 280 nm. Thus, in CIEF peptide mapping, fewer peaks can be observed than in CZE [23]. This mapping method is difficult to use alone for characterization of proteins. The second problem is the difficulty to determine p*I* values of peptides accurately. Conventional CIEF uses a mobilization process after the focusing process to migrate all sample zones past the detection point of an on-column detector. The mobilization speed is not constant, resulting in distortion of the linear pH gradient created in the focusing process [24]. Therefore, p*I* values of peptides cannot be determined directly from their retention times. Both problems can be solved by our universal imaging detection system.

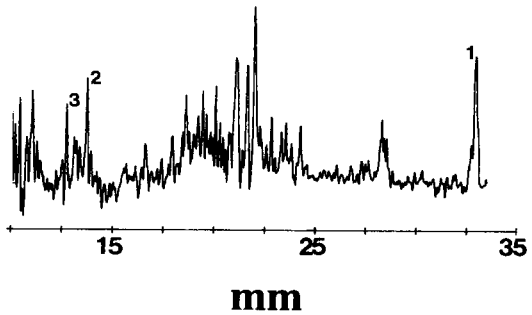

Fig. 4. Isoelectric electropherogram of tryptic peptides from bovine cytochrome c. Concentration of the protein before digestion is 1 mg/ml. Only peaks 1, 2, and 3 can be detected by UV absorption detectors operated at 280 nm.

Fig. 4 shows an isoelectric electropherogram of tryptic peptides of bovine heart cytochrome c. More than ten peptides are apparent in the p*I* range 4.8–9.2 although the concentration of each peptide is low. The concentration of the protein before digestion is 1 mg/ml. The standard deviations of peak positions based on three runs are less than 300 μm for the 4-cm-long capillary which corresponds to 0.05 pH for p*I* determination. This is much better than that of conventional CIEF instrument [23]. CIEF instruments with a UV absorption detector can only detect three tryptic peptides of bovine cytochrome c in the pH range 4.8–9.3 [23]. These three peptides have p*I* values of 9.3, 5.6, and 5.4. Results in Fig. 4 agree very well with these values. The p*I* values of the peaks 1, 2 and 3 in Fig. 4, which can be calculated directly from their positions inside the capillary, are 9.10, 5.62, 5.46, respectively. However, this electropherogram was obtained in only 2–4 min. This is the highest speed ever reported for peptide mapping. The high speed is a special advantage of using the CIEF-imaging detection system as the second separation step in conjunction with LC for two-dimensional protein separations [25].

In the future, the CIEF diode laser-based imaging detector system will be developed into a multi-channel electrophoretic technique [26]. The capillaries can be replaced by multi-channels etched on quartz plates

[27]. The whole instrument, including the diode laser, CCD sensor and multi-channels, could be constructed on a single wafer.

Acknowledgements

This work was supported by the Natural Sciences and Engineering Research Council of Canada. The authors thank L. Vonguyen for her help in tryptic digestion of proteins and M. Adams for his editorial assistance in preparing this manuscript.

References

[1] T. Imasaka and N. Ishibashi, Anal. Chem., 62 (1990) 363A.
[2] M. Ohtsu, H. Kotani and H. Tagawa, Jpn. J. Appl. Phys., 22 (1983) 1553.
[3] Y. Kawabata, T. Kamikubo, T. Imasaka and N. Ishibashi, Anal. Chem., 55 (1983) 1419.
[4] T. Imasaka, A. Yoshitake and N. Ishibashi, Anal. Chem., 56 (1984) 1077.
[5] R. Hergenroder and K. Niemax, Spectrochim. Acta, 43B (1988) 1443.
[6] P.A. Johnson, J.A. Vera, B.W. Smith and J.D. Winefordner, Spectrosc. Lett., 60 (1988) 607.
[7] T. Higashijima, T. Fuchigami, T. Imasaka and N. Ishibashi, Anal. Chem., 64 (1992) 711.
[8] J. Pawliszyn, Rev. Sci. Instrum., 58 (1987) 245.
[9] C. Chen, T. Demana, S. Huang and M.D. Morris, Anal. Chem., 61 (1989) 1590.
[10] J. Wu, P. Frank and J. Pawliszyn, Appl. Spectrosc., 46 (1992) 1837.
[11] T. Wehr, M. Zhu, R. Rodriguez, D. Burke and K. Duncan, Am. Biotechnol. Lab., 8 (1990) 22.
[12] J. Wu and J. Pawliszyn, J. Liq. Chromatogr., 16 (1993) 1891.
[13] J. Wu and J. Pawliszyn, Anal. Chem., 64 (1992) 224.
[14] J. Wu and J. Pawliszyn, Anal. Chem., 64 (1992) 2934.
[15] J. Wu and J. Pawliszyn, Anal. Chem., 66 (1994) 867.
[16] W.A. Stolzenburg, J. SMPTE, 74 (1965) 654.
[17] P.M. Young and T.E. Wheat, Peptide Res., 3 (1990) 287.
[18] J. Pawliszyn, Spectrochim. Acta Rev., 13 (1990) 311.
[19] S.J. Loomis, M. Go, L. Kupeli, D.J. Bartling and S.R. Binder, Am. Clin. Lab., (1990) 33.
[20] M. Zhu, R. Rodriguez, T. Wehr and C. Siebert, J. Chromatogr., 608 (1992) 225.
[21] R.L. Garnick, N.J. Solli and P.A. Papa, Anal. Chem., 60 (1988) 2546.
[22] K.A. Cobb and M. Novotny, Anal. Chem., 61 (1989) 2226.
[23] J.R. Mazzeo, J.A. Martineau and I.S. Krull, Anal. Biochem., 208 (1993) 323.
[24] F. Kilar, J. Chromatogr., 545 (1991) 403.
[25] M.M. Bushey and J.W. Jorgenson, Anal. Chem., 62 (1990) 978.
[26] J. Wu and J. Pawliszyn, Electrophoresis, 14 (1993) 469.
[27] D.J. Harrison, A. Manz, Z. Fan, H. Ludi and H.M. Widmer, Anal. Chem., 64 (1992) 1926.

ELSEVIER

Analytica Chimica Acta 299 (1995) 343–347

ANALYTICA CHIMICA ACTA

Application of coaxial beam photothermal microscopy to the analysis of a single biological cell in water

Masaaki Harada, Masashi Shibata, Takehiko Kitamori, Tsuguo Sawada *

Department of Applied Chemistry, Faculty of Engineering, The University of Tokyo, 7-3-1 Hongo, Bunkyo, Tokyo 113, Japan

Received 15 February 1994; revised manuscript received 11 April 1994.

Abstract

Photothermal microscopy, with the excitation and probe beams coaxial under a microscope, was shown to provide highly sensitive absorptiometry for micro-objects. The signal dependence on the modulation frequency showed that the detected signal was photothermally generated. In addition, the thermal lens effect of the microparticle itself was expected to be dominant, judging from the signal dependence on the focal point of the excitation and probe beams. This method was applied to the measurement of a single, stained biological cell in water. The results suggested that the method could measure a trace amount of chemical species in a living biological cell.

Keywords: Laser spectroscopy; Coaxial beam; Photothermal microscopy; Microscopy

1. Introduction

Great demands for microanalysis have been raised in a variety of technological fields, such as polymer, electronic, and biological industries. Although elemental analyses using ions and electrons have been the mainstream, a high-vacuum environment is needed. Lately laser spectroscopic microanalysis has attracted considerable attention, as it nondestructively gives chemical information with a high sensitivity. In addition, visible spectrometry can be applied to measurements in water, which is one of the most important characteristics.

Photothermal spectroscopy is well established as a highly sensitive spectroscopic method [1–5] and it has been successfully applied to microscopic investigation. We have developed a new type of photothermal microscopic technique [6], in which the excitation and probe beams are coaxially passed through the body tube of a microscope and focused by an objective lens into the sample. Among various kinds of proposed detection techniques, it may be classified as dual-beam thermal lens spectroscopy [7] considering the optical arrangement, but details remain to be clarified. Introducing a microscope into the photothermal measurement system makes it possible to selectively measure a particular microscopic area of the sample or microsubstances, the sizes of which are several μm to several tens of μm. We have already reported that with the method 6 fg of Fe–8-quinolinol chelate adsorbed on a 50-μm diameter microparticle was detectable. The detection limit of absorbance was calculated as 10^{-3} [6].

* Corresponding author.

SSDI 0003-2670(94)00314-9

Previous studies were all performed in air. In this report, measurements in water were undertaken to allow application of the method to in vitro measurements of biological cells. Quantitation results of stained mouse hybridoma cells are presented and discussed. The signal generation mechanism is also examined on the basis of the signal dependence on the modulation frequency and focus height of the beams.

12. Experimental

The experimental setup was the same as that reported before [6]. The modulated excitation beam (488.0-nm emission line of an Ar ion laser) and probe (633-nm beam of a 1-mW He–Ne laser) beam were coaxially passed through the body tube of the microscope and then focused by an objective lens onto the sample placed on the sample stage. The coaxial beams transmitted from the sample were collected with another objective, and the probe beam was selectively passed through an optical filter and its intensity was monitored by a photodiode. The signal from the photodiode was pre-amplified by a gain of 100 and synchronously detected by a lock-in amplifier with the modulation.

Polystsyrene microparticles containing four different amounts of red dye, homogeneously distributed inside the particles, were used to test the quantitative ability of this method and its applicability to measurements in water. The microparticle diameters were around 40 μm. As a practical sample, mouse hybridoma cells (diameter about 20 μm) were cultured and stained at five different concentrations of dye solutions (8, 2, 1, 0.4, and 0.2 μg/ml). Trinitrobenzenesulfonate sodium salt (TNBS), which is sensitive towards amino acids and colour them yellow, was used as a dye. The cells were dyed at 37°C for 5–10 min.

13. Results and discussion

Judging from the experimental arrangement, the spatial intensity profile of the probe beam is expected to be modulated while it travels through the temperature gradient field produced photothermally, which may possibly generate the signal. No signal was obtained without the excitation beam or without the probe beam, and the signal intensity was linearly proportional to the excitation beam power [6]. However, such a signal dependency could be also observed when the excitation beam power was detected. Then in the first place, to confirm that the detected signal is indeed photothermally generated, the modulation frequency dependence of the signal was measured. The excitation beam intensity was modulated acousto-optically between 10 and 10000 Hz, and the whole frequency range was covered in three measurements. The measured sample was a dye-containing polystyrene microparticle. The result is shown in Fig 1. The signal intensity was independent of the modulation frequency at low frequencies due to thermal saturation, while it was proportional to the inverse of the modulation frequency at extremely high frequencies. On the other hand, theoretical analysis predicts that when an excitation laser beam with a Gaussian intensity distribution irradiates a transparent plane sample, the temperature distribution at a sample surface is given by [8].

$$T(r) \propto \int_0^\infty \frac{1}{\delta^2 + \frac{i\omega}{D}} \exp\left(-\frac{R^2\delta^2}{4}\right) \delta J_0(\delta r)\, \mathrm{d}\delta$$

where $T(r)$ (K) is the temperature variation as a function of the radial distance r (m) from the center of the laser beam; δ (m^{-1}) is the spatial frequency; i is the imaginary unit; ω (rad/s) is the angular modulation frequency; D (m^2/s) is the thermal diffusivity; R (m) is the beam radius; and $J_0(\delta r)$ is the Bessel function of zero-th order. As photothermal signal intensity is determined approximately by temperature arise, this expression means that the photothermal signal intensity is nearly constant due to saturation by thermal equilibrium as ω approaches 0, while it is proportional to ω^{-1} as ω reaches infinity. So the result shown in Fig. 1 was solid evidence that detected signal was photothermally generated. From these photothermal characteristics of the signal, it is as concluded that the photothermal signal was generated from the microparticles and detected in the present experiment.

Photothermal phenomena expected to dominate this experiment were the thermal lens in the sample,

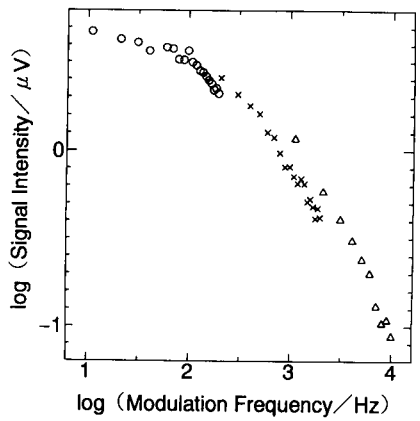

Fig. 1. Signal intensity dependence on the modulation frequency. Because of operational restrictions of the acousto-optic modulator, three measurements were made to cover the whole frequency range shown. 0 = 10–200 Hz; × = 200–2000 Hz; △ = 1000–10000 Hz.

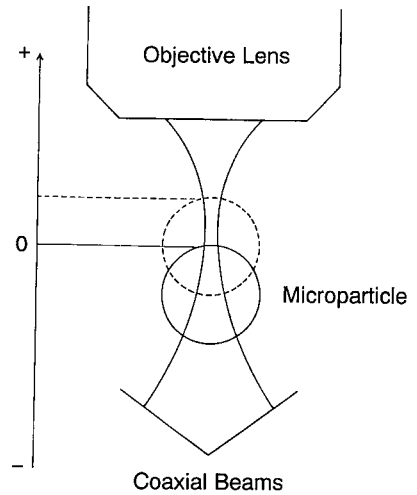

Fig. 2. Schematic of the experimental configuration of the coaxial beams and the particle.

the thermal wave in the air outside the sample, and the thermal expansion of the sample itself. Actually, the detected signal resulted from these several effects, but the thermal lens effect of the sample seemed to be dominant because the temperature gradient inside the sample was generated normal to the probe beam while that outside the sample was generated parallel to it. To confirm this, signal dependence on the distance between the sample surface and the focal point of the laser beams was examined. The test sample was a 50-μm diameter XAD (polystyrene–divinylbenzene copolymer) particle, which adsorbed the Fe–8-quinolinol chelate complex only on a surface. Detailed descriptions of the sample have been reported elsewhere [9,10]. The signal amplitude and phase were measured as the sample was moved up and down relative to the focal point of the laser beams as shown in Fig. 2. The result is shown in Fig. 3. As seen from Fig. 2, positive distances on the abscissa of Fig. 3 mean that the focal point is inside the sample, while negative ones mean that the focal point is outside it. The origin on the abscissa means that the focal point is at the sample surface.

The signal intensity was maximized when the focus was a short distance inside the sample, while the phase changed by 180° when the focal point passed through the sample surface. The thermal lens theory predicts that the signal intensity from a thin plane sample is maximized when the sample is before and beyond the beam waist and that the thermal lens placed before the waist converges the beam while the same lens beyond the waist diverges it [11]. However, these two peaks are not always symmetric relative to the beam waist because the experimental parameters such as a beam diameter, a beam divergence, and a wavelength are different between the excitation and probe beams. Also in the measurements, the signal intensity peak was sometimes observed when the focal point was a short distance outside the sample, but not so frequently observed as when the focal point was inside the sample. Therefore, we supposed that apart from the reasons men-

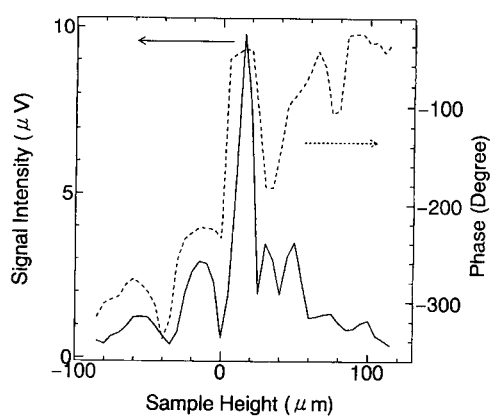

Fig. 3. Signal dependence on the distance between the focal point of the coaxial beams and the particle surface.

tioned above, the sample thickness and shape were responsible for the result. The observed features of the signal are characteristic of a thermal lens signal and it was concluded that the thermal lens effect of the sample should be dominant.

The quantitative ability of this method in air has already been proved with polystyrene microparticles [6]. The signal intensity linearly depended on the amount of dye contained in one particle in the range of some tens to hundreds of pg of dye, and 8 pg or less of dye was also proved to be detectable with an output power of 10 mW. So far all the experiments were performed in air.

To measure biological samples in vitro measurements in water were tried. Polystyrene microparticles, dispersed in water, were sandwiched between the slide glass and cover glass, as shown in Fig. 4. When measured in water, the signal intensity decreased to less than half of that when measured in air due to scattering loss of beam intensity by the cover glass, but considering the low output power used (10 mW), the measurements in water were judged to be still more sensitive than conventional microspectrometry and to be quite practicable.

Then stained biological cells were measured. These results are shown in Fig. 5. The output power of the Ar ion laser was 150 mW just after the laser head and the excitation beam power irradiating the particle virtually was assumed to be less than a tenth of it. About eight cells from dye solutions of different concentrations were measured and the mean value and standard deviation of the signal intensity were plotted. The observed large variation of the signal intensity seemed to come from different amounts of dye contained in the cells, even though stained in the same dye solution, as the variation in repeated measurements of one polystyrene microparticle in air was rather small. Considering this, the signal intensity seemed to be generally proportional to the dye concentration in the low concentration range (presumably less than 0.5 μg/ml of TNBS concentration), while independent of it in the high concentration range. Though more measurements in the low concentration range are necessary, it is expected that this method can be applied to quantitating a trace amount of chemical species distributed in a biological cell in vitro. For detailed evaluation of applicability to biological cells, determination of an absolute amount of dye distributed in a particle with fluorescent microspectrometry is now in progress.

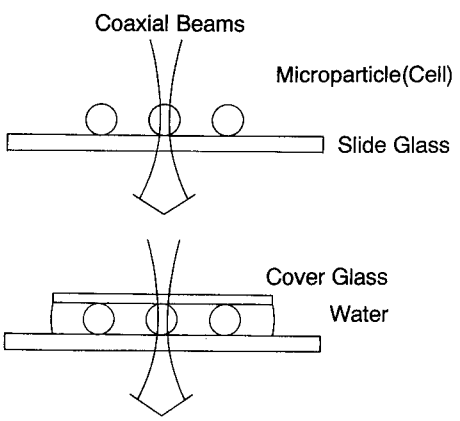

Fig. 4. Schematic illustration of the sample environments in air and water.

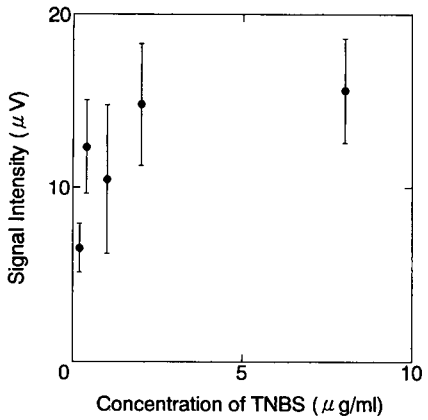

Fig. 5. Signal intensity dependence on the concentration of the dye solution.

Acknowledgements

We thank Dr. E. Suzuki and Dr. H. Ueda of the Department of Chemical Engineering, Faculty of Engineering, The University of Tokyo, Japan, for preparation of the stained biological cells and useful discussions.

References

[1] M.D. Morris and K. Peck, Anal. Chem., 58 (1986) 811A.
[2] J.C. Murphy and L.C. Aamodt, J. Appl. Phys., 51 (1980) 4580.
[3] W.B. Jackson, N.M. Amer, A.C. Boccara and D. Fournier, Appl. Opt., 20 (1981) 1333.
[4] A. Mandelis, J. Appl. Phys., 54 (1983) 3404.
[5] T.I. Chen and M.D. Morris, Anal. Chem., 56 (1984) 19.
[6] M. Harada, K. Iwamoto, T. Kitamori and T. Sawada, Anal. Chem., 65 (1993) 2938.
[7] H.L. Fang and R.L. Swofford, in Ultrasensitive Laser Spectroscopy, Academic Press, New York, 1983, P. 175.
[8] L.C. Aamodt and J.C. Murphy, J. Appl. Phys., 52 (1981) 4903.
[9] A. Yoshinaga, Y.-M. Hsueh, T. Sawada and Y. Gohshi, Anal. Sci., 5 (1989) 147.
[10] Y.-M. Hsueh, A. Harata, T. Kitamori and T. Sawada, Anal. Sci., 6 (1990) 71.
[11] J.M. Harris and N.J. Dovich, Anal. Chem., 52 (1980) 695A.

ELSEVIER

Analytica Chimica Acta 299 (1995) 349–354

ANALYTICA CHIMICA ACTA

Study of electrochemical interfaces by transient reflecting gratings

Akira Harata, Takahiro Kawasaki [1], Masaki Ito, Tsuguo Sawada *

Department of Applied Chemistry, Faculty of Engineering, University of Tokyo, 7-3-1 Hongo, Bunkyo-ku, Tokyo 113, Japan

Received 15 February 1994; revised manuscript received 24 March 1994

Abstract

Picosecond photothermal/photoacoustic measurement of gold interfaces in some aqueous solutions of electrolytes was carried out using a transient reflecting grating (TRG) method. As the electric potential became more anodic, the TRG-induced diffracted-light intensity increased above that expected from the reflectivity change, and the transient waveform also changed, both in the electrical double-layer and Faradaic oxidation regions. These changes were related to the anions in the supporting electrolyte. These results are discussed with respect to the photothermal and photoacoustic effects at the nanometer-scale interface.

Keywords: Transient reflecting gratings; Picosecond photothermal effect; Hypersonics interfacial waves; Electric double-layer

1. Introduction

In this paper, experimental results on picosecond photothermal/photoacoustic (PT/PA) measurements at the interfaces between gold and aqueous solutions of some electrolytes (e.g., H_2SO_4, $HClO_4$ or HCl) observed as the transient reflecting grating (TRG) signals are reported. In the TRG method, transient gratings [1] are formed on the surface of an opaque material, or at the interface, by holographic illumination of two pulsed laser beams, and they are detected as reflecting gratings [2–8]. These TRGs consist of thermal, acoustic and electronical gratings locally formed at the interface. Unlike the conventional PT/PA methods, the TRG method can be used for ultrafast PT/PA studies of interfaces when they are combined with a synchronously delayed pump-probe technique. Since that temporal resolution is improved up to the pulse-duration limit of the light source, both the ranges of heat conduction and acoustic localization can be reduced and therefore, spatial resolution is improved. It provides higher selectivity and sensitivity at the spatially limited area, i.e., the interface, with suppressed disturbance from bulk materials.

Kasinski et al. [9] and Miller [10] were the first to demonstrate generation and detection of hypersonic interfacial waves (HIWs) at a water/polar TiO_2 interface using a transient grating method. They detected diffracted light passing through the surface restricted-volume grating in transmission geometry. It is noted that TiO_2 is a semiconductor and transparent to longer-wavelength light. Later, Harata et al. [2] observed hypersonic surface acoustic waves (SAWs) on an aluminum film and a silicon single crystal using the TRG method, i.e., in reflection geometry. Detection in reflection is somewhat inferior because of the much smaller diffraction efficiency [11], but it is superior in selectivity for a surface or interface [12]; i.e., detection by reflection allows a thinner surface or interface to be observed. In fact, our group [2–6] has successfully

* Corresponding author.

[1] Present address: LNG engineering sect., Tokyo Gas Co., Ltd., 1-1 Nakasode, Sodegaura-shi, Chiba 299-02, Japan.

SSDI 0003-2670(94)00321-1

applied the TRG method to monitor an ion-implanted silicon surface and to evaluate the change in, for example, thermal diffusivity, SAW velocity and Auger recombination rate due to ion implantation.

Since the PT/PA methods are important and extensively used for calorimetric measurements of interfacial phenomena [13], in the present work, we experimentally demonstrated the ability for investigating picosecond PT/PA phenomena at electrochemical interfaces by using the TRG method.

2. Principles

The principles of the TRG method applied to the metal/liquid interface is schematically shown in Fig. 1. When two ultrashort light pulses (pump pulses) having the same wavelength λ and intensity I_e overlap spatially and temporally at the metallic surface with a crossing angle 2θ, the optical interference fringes having a period $\Lambda = \lambda/2 \sin\theta$ are projected on the surface. As a result of ultrafast photothermal energy conversion, a thermal grating of spatially modulated temperature rise is instantly formed in the metal and diffused to the liquid through the interface. They are followed by formation of a temporal oscillating interfacial corrugation due to counterpropagating coherent HIWs (S-mode) generated via thermal expansion of the metal as well as the formation of a temporal oscillating longitudinal acoustic waves (L-mode) propagating parallel to the interface in the liquid. Both the thermal and acoustic gratings have the same spatially periodic profiles as the optical interference fringes, so that all the gratings, as well as the acoustic wavelength, have the same spacing Λ unless no non-linear phenomena occur. Because of spatially periodic perturbations of both dielectric constants and boundary conditions, these gratings collectively act as reflecting gratings and diffract the third light pulse (probe pulse) at certain fixed angles. (In this report, we neglect a concentration grating of excited-state density formed soon after laser illumination.)

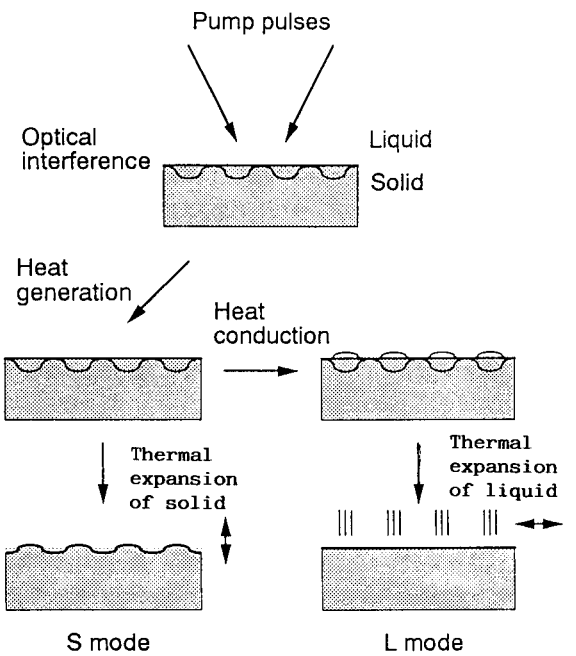

Fig. 1. Principle of the TRG method applied to the metal/liquid interface. Interference pattern formed by two pumping pulses generates thermal grating on/in the solid followed by thermal diffusion to liquid and thermal expansion of both solid and liquid.

The thermal grating decays to equilibrium through thermal diffusion, and the acoustic waves disappear through both attenuation and propagation away from the excited region. The temporal behaviors of these gratings are monitored by detecting the diffracted light of the probe pulse delayed with respect to the pump pulses. As an analogy of TRG formation on the surface [4,5], we can describe the time-dependent signal intensity $S(t)$,

$$S(t) = rI_p[(1-r)I_e g(t)]^2 \quad (1)$$

where r is the reflectivity, I_p and I_e are the intensities of a probe pulse and a pump pulse, respectively, and $g(t)$ is the time- dependent term in the signal. For the surface, we can successfully give an empirical form of $g(t)$ as a function of SAW frequency, onset time of SAW generation, attenuation time constants for the thermal grating and SAW, respectively, and the contribution ratio between thermal and acoustic effects to grating amplitudes [4,5]. However, we do not discuss the appropriate $g(t)$ form for the metal/liquid interface in this paper.

3. Experimental

The experimental setup is illustrated in Fig. 2. The TRG measurement system was the same as previously reported [4,6], although the sample was immersed in an aqueous solution of an electrolyte in an electrochem-

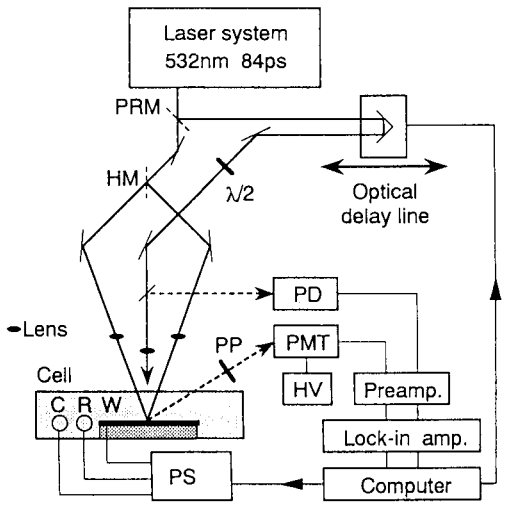

Fig. 2. Experimental setup for the transient reflecting grating experiment at a electrochemical interface: PRM, partially reflective mirror; HM, half-mirror; λ/2, half-wave plate; PD, photodiode; PP, polarizing plate; HV, high-voltage power supply; PMT, photomultiplier tube; other optical elements, mirrors or prisms; W, working electrode; R, reference electrode (Ag/AgCl); C, counter electrode; and PS, potentiostat.

ical cell. A mode-locked Q-switched Nd:YAG laser was used as the light source. A single pulse was selected from the output pulse trains in a Q-switched pulse, and its frequency was doubled to generate a polarized visible light pulse (wavelength, 532 nm; pulse width, 84 ps; repetition rates, 1.03 kHz). A portion of the light pulse was sampled by a partially reflective mirror and was led to a computer-controlled optical delay line to provide a synchronously delayed probe pulse. The remainder was attenuated and halved to generate two pump pulses. They were overlapped again to produce optical interference fringes in a 60-μm diameter spot on the interface, while their incident angles normal to the surface were adjusted to θ and $-\theta$. The fringe spacing Λ was 0.80, 1.48, 1.62 or 2.30 μm. The maximum intensity of each pump pulse was less than 0.3 μJ/pulse and no damage to the metal electrode and no bubble generation were observed during the experiments. Through all the measurements, the electric fields of the pump pulses were parallel to their incident plane, i.e., p-polarized.

The delayed probe pulse was focused to a 40-μm diameter spot and was incident normal to the surface at the center of the pump interference pattern after its polarization was rotated by a half-wave plate to be perpendicular to that of the pump pulses. Typically, the probe light energy was less than 10 nJ/pulse. A part of the probe light was diffracted toward specific directions defined as the Bragg condition of the TRGs. One of the diffraction spots was separated from the scattered light by an aperture and a polarizing plate (PP). (PP was set to cut out p-polarized light and to transmit s-polarized light.) The diffracted light was detected with a photomultiplier tube. The signal was amplified with a preamplifier before being fed into the lock-in amplifier which was connected to a microcomputer. The intensity was recorded as a function of the position of the delay line to obtain TRG responses.

A 1-μm thick polycrystalline gold film was evaporated onto a polycarbonate substrate and used as a working electrode (W). A platinum wire and Ag/AgCl electrode were the counter (C) and reference (R), respectively. The electrode potential of W was controlled by a potentiostat (PS) with respect to that of Ag/AgCl electrode. Aqueous solutions of H_2SO_4, $HClO_4$ or HCl were diluted from reagent grade acids as received, and their concentrations ranged from 0.05 to 0.10 M. The optical path length of the cell was 20 mm. Measurement was performed at room temperature after the solution was deoxygenated by N_2 gas bubbling.

The dependence of TRG responses on the following parameters was measured: intensity of laser pulse; electric potential of gold; and electrolyte in the solution.

4. Results and discussion

4.1. Typical TRG response and dependence of its intensity on electric potential

Fig. 3 displays a typical TRG response obtained for a gold–0.05 M H_2SO_4 aqueous solution interface with

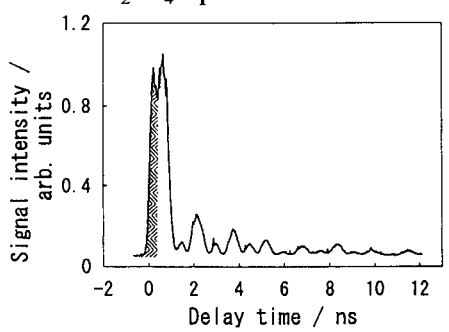

Fig. 3. Typical response of the transient reflecting gratings formed at gold/0.05 M H_2SO_4 aqueous solution interface with $\Lambda = 1.62$ μm. The first peak (shadowed part) is thermal, the second is thermal + acoustic, and the others are acoustic.

$\Lambda = 1.62$ μm. The signal seems to be composed mainly of two types of gratings. The first peak (shadowed part) is thought to be thermal, the second is thermal + acoustic, and the others are acoustic. Since in the present experimental setup a single pulse is divided into three parts and used as two pump pulses and one probe pulse, the signal intensity must be dependent on the (laser intensity)^3 according to Eq. 1. We experimentally confirmed the cubic dependence at both the first and the second peaks of TRG response with $\Lambda = 2.30$ μm on gold (300 nm)/chromium (20 nm)/glass electrode of open circuit in ultrapure water. That result suggests no non-linear PT/PA processes occurred at the interface.

Setting the probe delay line at the first peak in Fig. 3, the potential of the working electrode was scanned like cyclic voltammetry, while the current density, J, TRG signal intensity, S, and reflected probe intensity, R, were measured. The results are shown in Fig. 4. Data were collected after more than three cyclic scans. The scanning speed was 70 mV/s. S and R are normalized, respectively, with the values S_0 and R_0 obtained at 0 V vs. Ag/AgCl. Fig. 4a shows the cyclic voltammogram of the gold electrode. Both the oxidation and reduction currents are observed above 1.2 and below 0.9 V vs. Ag/AgCl, respectively. At the maximum potential, two

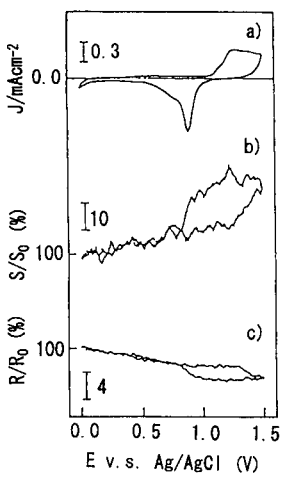

Fig. 4. Cyclic voltammogram at the gold electrode (a) and TRG signal intensity S and reflected probe intensity R measured during the electric potential scanning (b) and (c), respectively. The probe delay line was set at the first peak in Fig. 3 and the potential of the working electrode was cyclically scanned with 70 mV/s like cyclic voltammetry, while S, R and the current density J were simultaneously measured. S and R are normalized with the values S_0 and R_0 obtained at 0 V vs. Ag/AgCl, respectively.

to three monolayers of AuO_2 were estimated to be formed on the gold surface. The TRG signal gradually increased as the potential became more anodic even in the electric double layer region, 0.0–1.2 V, and a maximum increase of about 30% was observed corresponding to formation of gold oxide. On the other hand, R gradually decreased and a maximum decrease of about 5% was observed. The behavior of the reflectivity is the same as previously reported [14]. As shown in Eq. 1, the TRG signal intensity, S, is proportional to $r(1-r)^2$. The reflectivity of the gold in water for 532 nm light is about 70%, therefore a 3.5% decrease in r, which is equal to a 5% decrease in R, should result in a 18.5% increase in S. The observed 30% increase in S is higher than the estimate, especially in the Faradaic oxidation region. Since the PT/PA signal is proportional to $1-r$ for a very thin oxide film on the electrode, the TRG is demonstrated to be more sensitive than PT/PA. Furthermore, these results suggest some additional property of the interface can be monitored with TRG.

4.2. Dependence of TRG waveform on electric potential

To investigate the origins of TRG signal intensity dependence on electric potential in detail, the dependence of the TRG waveform was measured for the gold–0.1 M $HClO_4$ aqueous solution interface by setting the gold potential to 0.0, 0.8 or 1.25 V vs. Ag/AgCl. The results with $\Lambda = 1.48$ μm are shown in Fig. 5. It is noted that oxide is not formed at 0.0 and 0.8 V (double layer region) and a few monolayers of gold oxide are formed at 1.25 V. The thick lines in Fig. 5a and b are for the 0.0 V state, the thin line in Fig. 5a is for the 1.25 V state and that in Fig. 5b for 0.80 V. The numbers indicated in Fig. 5a are for peak identification. When the electrode potential is anodic enough to form the oxide, the TRG waveform dramatically changes, as is shown in Fig. 5a. The large changes occurred at the 1st, 2nd, 4th, 6th, 8th, 10th and 12th peak and little at the other peaks. The largest change was observed at the 2nd peak. The intensity ratio between 0.0 and 1.25 V was not the same for the first and second peaks. The results cannot be explained by a simple model based on increased absorption by the oxide. It indicates the different contribution of different gratings having different dependence on the potential, as described before. Even at 0.8 V, the intensity at the first and second peaks was

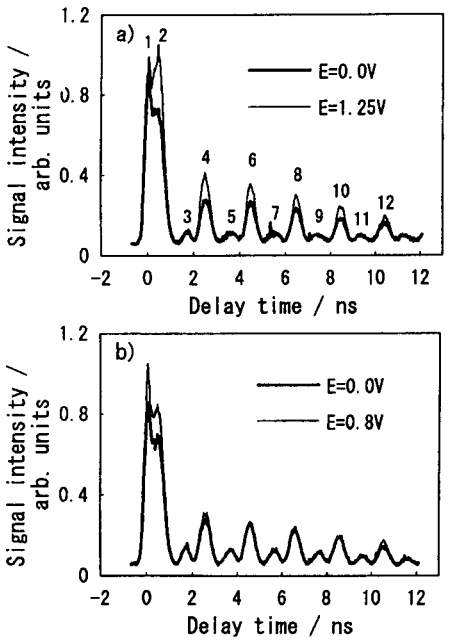

Fig. 5. TRG waveform dependence on electric potential. Measurement was performed at gold in 0.1 M $HClO_4$ aqueous solution by setting the gold potential to 0.0, 0.8 or 1.25 V vs. Ag/AgCl with $\Lambda = 1.48$ μm. Numbers in Fig. 5a are for peak identification.

changed as shown in Fig. 5b. What is important is that these waveforms are not similar to each other. The fact that the waveform changes means that a change in the thermal or acoustic property can be monitored by the TRG waveforms. As for thermal properties, the thermal diffusion length μ is defined as $(D\Delta t)^{1/2}$, where D is thermal diffusivity and Δt is the delay time after pump laser illumination. In water, $D = 1.2 \times 10^{-3}$ cm^2/s, so, it can be calculated that $\mu = 3.5$ nm when $\Delta t = 100$ ps. This value is comparable to the thickness of the electric double layer. The S-mode HIWs are localized at the interface within about 1/4 of its wavelength [8], i.e. several hundreds of nanometers. These facts mean high selectivity of TRG to the interfacial region. For example, as preliminary result [15], it was experimentally observed with $\Lambda = 0.80$ μm TRG at a gold/0.1 M $HClO_4$ interface that the frequency of HIWs calculated from the intervals between the peaks in TRG responses were slightly changed for 0.0 and 1.25 V, which may be due to change in the interfacial tension. The interfacial thermal and acoustic property is not well investigated because of lack of a measurement method. These results show the possibility of TRG for the purpose.

The initial part of Fig. 5b is expanded in Fig. 6a with data for 0.05 M H_2SO_4 and 0.1 M $HClO_4$ + 0.1 M HCl measured under the same experimental conditions in Figs. 6b and 6c, respectively. The ratios of waveform change between 0.0 and 0.8 V are not constant for different anions in the solution. It is indicated that, as anions become more tend to adsorb on the electrode ($Cl^- > SO_4^{2-} > ClO_4^-$), the ratio becomes smaller. These anions determine the environment of the electrical double layer near the interface, at a few nm from the vicinity of the electrode. In this region, both the structure and functionality of water are not the same as the bulk water. It is necessary to take into account some chemical aspects for the explanation of the TRG waveform.

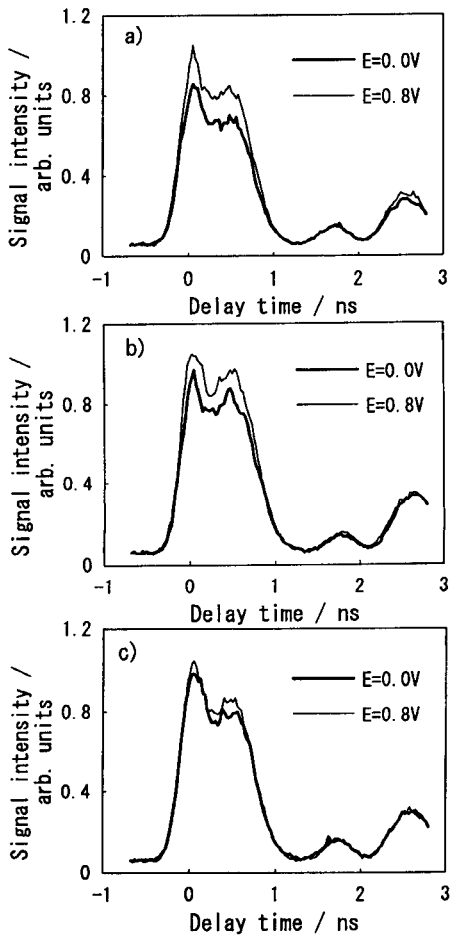

Fig. 6. TRG waveform dependence on electrical potential in various solutions. Measurement was performed at gold in 0.1 M $HClO_4$ (a), 0.05 M H_2SO_4 (b) or 0.1 M $HClO_4$ + 0.1 M HCl (c) by setting the gold potential to 0.0 and 0.8 V vs. Ag/AgCl with $\Lambda = 1.48$ μm.

5. Conclusions

The TRG method based on picosecond photothermal measurement is proposed as a new investigating tool of metal/solution interfaces. Interfaces between gold and aqueous solutions of some electrolytes were investigated. As the electrode potential becomes more anodic, the TRG-induced diffracted-light intensity increased beyond that expected from the change in reflectivity, and the transient waveform is also changed, both in the electric double layer and Faradaic oxidation regions. These changes were related to the anions in the supporting electrolyte. These findings will provide additional important information for microscopic interfacial characterization.

References

[1] H.J. Eichler, P. Günter and D.W. Pohl, Laser-Induced Dynamic Gratings, Springer Verlag, Berlin, 1986, Chap. 1, p. 2.
[2] A. Harata, H. Nishimura and T. Sawada, Appl. Phys. Lett., 57 (1990) 132 (errata: 57 (1990) 2034).
[3] A. Harata and T. Sawada, Appl. Phys. Lett., 58 (1991) 1839.
[4] A. Harata, H. Nishimura, T. Tanaka and T. Sawada, Rev. Sci. Instrum., 64 (1993) 618.
[5] A. Harata, Q. Shen, T. Tanaka and T. Sawada, Jpn. J. Appl. Phys., 32 (1993) 3633.
[6] H. Nishimura, A. Harata and T. Sawada, Jpn. J. Appl. Phys., 32 (1993) 5149.
[7] D.M. Pennington and C.B. Harris, IEEE J. Quantum Electron., QE-28 (1992) 2523.
[8] A. Harata and T. Sawada, Proc. 12th Symp. Ultrasonic Electronics, Tokyo, 1991, Jpn. J. Appl. Phys., 31 (1992) Suppl. 31-1, p. 88.
[9] J.J. Kasinski, L. Gomez-Jahn, K.J. Leong, S.M. Gracewski and R.J.D. Miller, Opt. Lett., 13 (1988) 710.
[10] R.J.D. Miller, in R.J.H. Clark and R.E. Hester (Eds.), Time Resolved Spectroscopy, Wiley, Chichester, 1989, p. 1.
[11] H. Bergner, V. Bruckner and M. Supianek, IEEE J. Quantum Electron., QE-22 (1986) 1306.
[12] I.M. Fishman, C.D. Marshall, J.S. Meth and M.D. Fayer, J. Opt. Soc. Am. B, 8/9 (1991) 1880.
[13] A. Mandelis, Anal. Sci., 6 (1990) 491; and references cited therein.
[14] T. Takamura, K. Takamura, W. Nippe and E. Yeager, J. Electrochem. Soc., 117 (1970) 626.
[15] A. Harata, Kagaku to Kogyo (Chemistry and Chemical Industry, Chem. Soc. Jpn), 45 (1992) 229 (in Japanese).

ELSEVIER

Analytica Chimica Acta 299 (1995) 355–360

ANALYTICA CHIMICA ACTA

Dependence of the laser two-photon ionization signal of anthracene on the electron mobility and the excess energy in non-polar solvents

Teiichiro Ogawa *, Miki Sato, Makoto Tachibana, Kazuhiko Ideta, Takanori Inoue, Keiji Nakashima

Department of Molecular Sciences and Technology, Kyushu University, Kasuga-shi, Fukuoka 816, Japan

Received 6 January 1994; revised manuscript received 10 March 1994

Abstract

The photocurrent and photoionization charge of anthracene in various non-polar solvents have been measured under the third-harmonics of a Nd–YAG laser excitation. They are quadratically proportional to the laser pulse energy, though those of water are cubically proportional to them. Anthracene exhibited a larger signal in those solvents in which both the electron mobility and the excess energy are large. Such solvents offered a higher sensitivity for the photoionization technique. Degassing showed only a minor effect. The detection limits were 14 ng/dm^3 (ppt) in hexane and 3.0 ng/dm^3 (ppt) in 2,2,4-trimethylpentane.

Keywords: Anthracene; Laser spectroscopy

1. Introduction

Laser two-photon ionization via a resonant state is useful and selective for the ionization of photoabsorbing molecules [1,2]. Detection of charged species by conductometry offers a sensitive analytical technique both in solution [3–8] and on surface of metals [9,10] and of solutions [11,12].

Ionization processes are dramatically influenced by the medium. In the sequential photoionization process the molecule is excited to an intermediate excited state and then the excited molecule absorbs the second photon to create a geminate electron-ion pair (process 1 below), where an electron and an ion are still captured in the same solvent cage. The process can be described as follows [13–16]:

$$A + h\nu \rightarrow A^*,\ A^* + h\nu \rightarrow (A^+ \cdots e) \quad (1)$$

$$(A^+ \cdots e) \rightarrow A^+ + e \quad (2)$$

$$e + A \rightarrow A^- \quad (3)$$

The escape probability of an electron from the geminate pair (process 2) depends on the electron mobility of the solvent and the excess energy of the geminate pair; when either of them is large, more ions are created [13–16]. Thus, more sensitive detection would be possible in a solvent of which the electron mobility is large and in a solvent in which the ionization threshold of the solute is low. The electron mobility tends to increase with the degree of sphericity of the molecules, and is closely correlated with thermalization ranges of secondary electrons [15]. The electrons escaped from the geminate pair are quickly captured by neutral solutes

* Corresponding author.

Elsevier Science B.V.
SSDI 0003-2670(94)00310-6

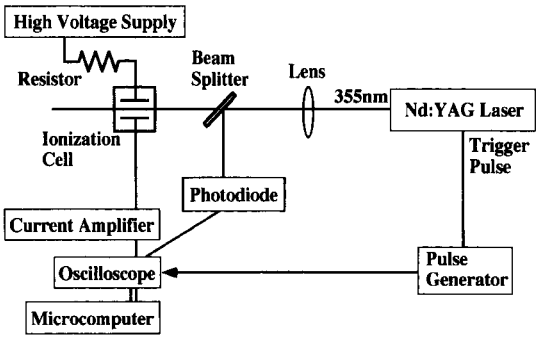

Fig. 1. Schematic diagram of the experimental apparatus.

within 50 ns (process 3) [17]. The time profile of photocurrent in the μs–ms range is due to drifts of cations and anions, and depends on the space charge effect [18].

In the present paper, we are reporting the dependence of photoionization signal of anthracene on the electron mobility of several solvents and on the excess energy in them. Dependence of the detection limits on both the electron mobility and the excess energy has been obtained.

2. Experimental

The schematic diagram of the experimental apparatus is shown in Fig. 1. The third harmonics of a Nd–YAG laser (Spectra Physics GCR-11; 60 mJ and 5–6 ns at 355 nm) was operated at a repetition rate of 7 Hz and was focused softly into a sample cell. The cell consisted of a fluorescence cell (4×1×1 cm) and a pair of copper electrodes (3.5×0.8 cm) as shown in Fig. 2. The electrode spacing was 2 mm. One of the electrodes was connected to a high-voltage power supply unit (Ikegami HD2.5KM) through a current-limiting resistor of 10 MΩ, and the other to a current amplifier (Keithley 427). The signal was measured with a digital storagescope (Iwatsu DS6411; 40 MHz). The data were analyzed with a microcomputer (Epson PC286L).

The anthracene (research grade) was obtained from Kishida and used as supplied. The pentane, hexane, cyclohexane and 2,2,4-trimethylpentane (isooctane) were research-grade obtained from Kishida. The cyclopentane and 2,2-dimethylbutane (neohexane) were research grade obtained from Tokyo Kasei Kogyo. The tetramethylsilane was research-grade and obtained

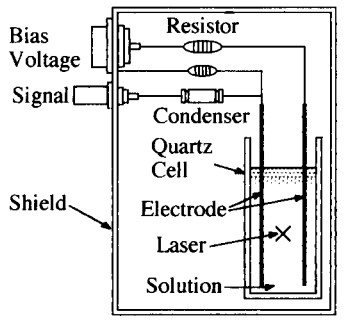

Fig. 2. Schematic diagram of the cell. It consists of a fluorescence cell and a pair of copper electrodes. The resistor to the high voltage power supply was 10 MΩ, and that to ground was 1 MΩ. The condenser was 0.47 μF.

from Janssen Chimica. They are used as received except for the determination of detection limits, where they were distilled.

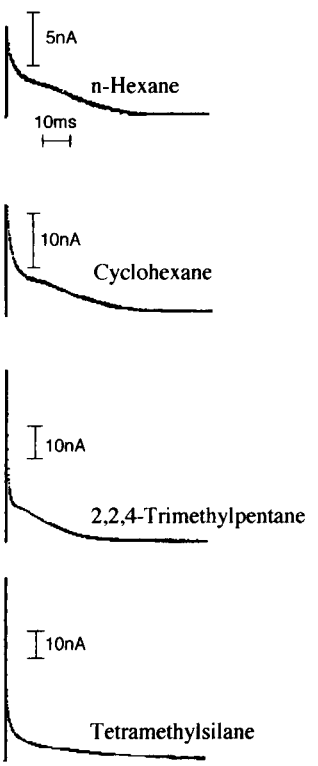

Fig. 3. Typical time profiles of photocurrent of anthracene (1×10^{-6} M). Laser pulse energy: 600 μJ (hexane, cyclohexane), 300 μJ (2,2,4-trimethylpentane), 250 μJ (tetramethylsilane). Resolution time: 10 μs. Electrode spacing: 2 mm. Applied voltage: 1.5 kV.

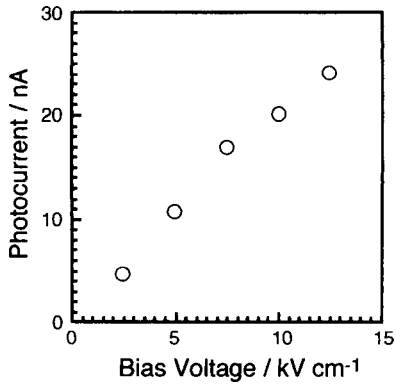

Fig. 4. Dependence of photocurrent of anthracene (1×10^{-6} M) in hexane on the applied bias voltage.

3. Results and discussion

Time profiles of the photoionization current of anthracene (1×10^{-6} M) in four typical non-polar hydrocarbon solvents are shown in Fig. 3; the resolution time used in these measurements was about 10 μs. These profiles exhibited a typical shape that is influenced by the space charge [18]. Its peak height was taken as photocurrent and its peak area as photoionization charge.

The photocurrent was linearly proportional to the applied voltage as shown in Fig. 4. It seems to be saturated at above 10 kV/cm, and 7.5 kV/cm was used for the following measurements.

Photocurrent of anthracene was quadratically proportional to the laser pulse energy, while that of the pure solvent was cubically proportional to it, as shown in Fig. 5 in hexane and in trimethylpentane; dimethylbutane and tetramethylsilane gave similar results. This finding indicates that two photons are necessary for the photoionization of anthracene, but three photons for non-polar hydrocarbon liquid.

Electron mobility of a dielectric liquid is closely related to the thermalization ranges of secondary electrons [15]. A geminate electron can move further in liquids with a large electron mobility and a large thermalization range, and thus has a larger probability for geminate separation, because it becomes so much spatially separated that mutual Coulombic attraction within a geminate pair becomes negligible compared to kT, where k is the Boltzmann constant. Dependence of the photoionization charge on the electron mobility of the solvent [20] is shown in Fig. 6a and that of photocurrent in Fig. 6b. As are shown in this figure, the larger the electron mobility of the solvent is, the larger is the photoionization signal. However, dependence is more evident for photocurrent, probably because the larger photoionization charges created at a solvent with higher mobility exhibit larger bulk recombination and the apparent photoionization charge does not increase as the photocurrent increases. Effect of degassing was small [7], as shown in Fig. 6b. An oxygen molecule may capture an electron created in geminate separation and become an oxygen anion. In either case, one anion is produced per one electron, and the total charge may differ little.

The photoionization threshold of anthracene is different for different solvents, as have been measured and calculated [19]. When the photoionization threshold (I_{th}) is low in a solvent, the geminate electron-ion pair in that solvent has a larger excess energy, which was

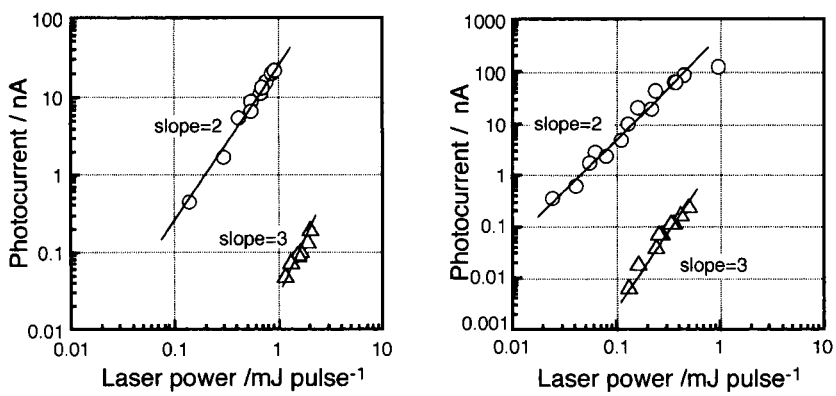

Fig. 5. Dependence of photocurrent of anthracene (1×10^{-6} M) in hexane (left) and in trimethylpentane (right) on the incident laser pulse energy. (○) Anthracene, (△) solvent. Electrode spacing: 2 mm.

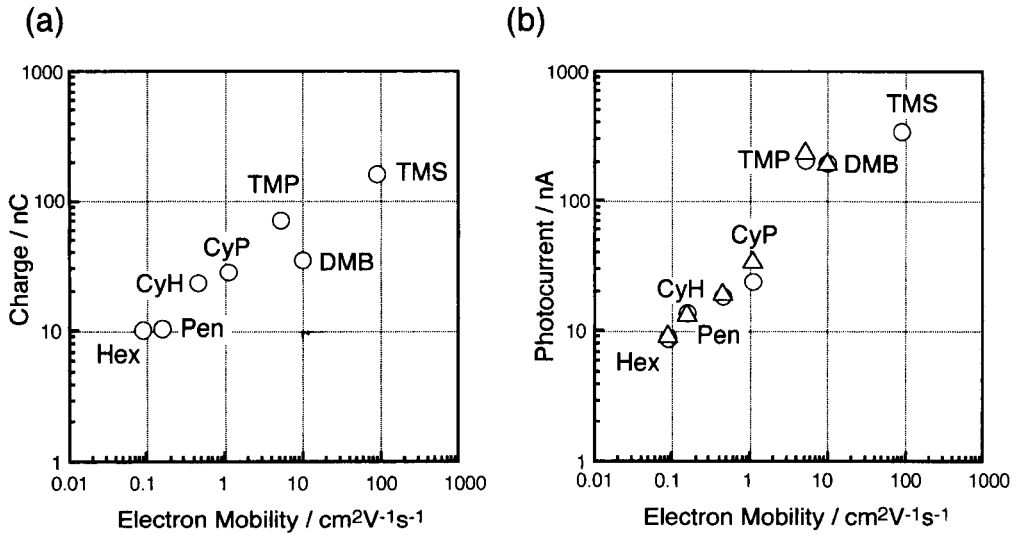

Fig. 6. Dependence of photoionization charge (a) and photocurrent(b) of anthracene (1×10^{-6} M) on the electron mobility of solvents. Laser pulse energy: 600 μJ. Hex = hexane, Pen = pentane, CyH = cyclohexane, CyP = cyclopentane, TMP = 2,2,4-trimethylpentane, DMB = 2,2-dimethylbutane, TMS = tetramethylsilane. (○) Without nitrogen bubbling, (△) after nitrogen bubbling.

defined as $6.81-I_{th}$ where 6.81 is the sum of the one-photon energy of the laser (3.50 eV) and the energy of the S_1 state (3.31 ± 0.01 eV [21]) of anthracene, because the S_1 state is the intermediate excited state for anthracene [22]. When the geminate pair has a larger excess energy, the geminate electron should carry a larger translational energy and can move further so that mutual Coulombic attraction within a geminate pair becomes negligibly small. Then, it has a larger probability for geminate separation. The photoionization charge and photocurrent are plotted versus the excess energy, as shown in Fig. 7. As expected, there is a good correlation between them. This finding indicates that use of a shorter-wavelength laser would increase the sensitivity of this technique.

Electron mobility is related to the electron affinity of the solvent (V_0); when the latter is large, the former is small [16]. The excess energy becomes larger as the I_{th} becomes smaller, and I_{th} is defined as $I_{th}=I_p+V_0+P^+$, where I_p is the ionization potential in the gas phase, and P^+ is the polarization energy of the positive ion. Thus, the electron mobility and the excess energy are related parameters, and the dependence of photocurrent on them may be similar.

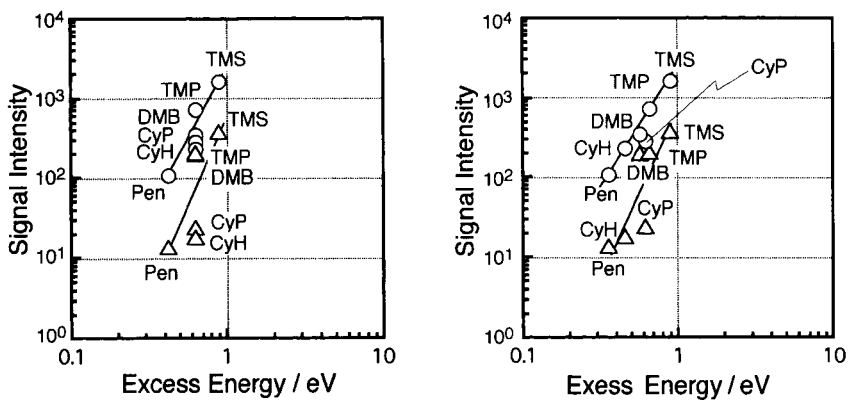

Fig. 7. Dependence of photocurrent (△) and photoionization charge (○) of anthracene (1×10^{-6} M) on the experimental values [19] (left) and the calculated values [19] (right) of the excess energy. Pen = pentane, CyH = cyclohexane, CyP = cyclopentane, TMP = 2,2,4-trimethylpentane, DMB = 2,2-dimethylbutane, TMS = tetramethylsilane.

Table 1
Detection limits of anthracene

Solvent	Excitation wavelength (nm)	Electron mobility [20] ($cm^2/V\,s$)	Detection limit (ng/dm^3)
Hexane	355	0.09	14 [a]
(Ref. [6])	337		10 [b]
2,2,4-Trimethylpentane	355	5.3	3.0 [a]

[a] Obtained at $S/N=3$, [b] obtained at $S/N=2$.

Typical analytical curves are shown for three laser pulse energies. The straight relation extends to a smaller concentration range when the laser pulse energy is increased. It is linear for more than three orders of concentration above the detection limits.

The detection limits were defined as a concentration where the signal-to-noise ratio (S/N) was three. The detection limits of anthracene were determined at the laser pulse energy of 2.5 mJ and are summarized in Table 1. The detection limit for anthracene in hexane excited at 337 nm (nitrogen laser) was reported to be 10 ppt at $S/N=2$ [6] and is almost equal to the present value in the same solvent, though the excess energy should be larger at 337 nm. The detection limit in 2,2,4-trimethylpentane is smaller than that obtained in hexane and than that published previously.

Because the electron mobility is much larger in 2,2,4-trimethylpentane than in hexane, Table 1 indicates that a solvent with a higher value of the electron mobility offers a much better detection limit in the laser two-photon ionization method. The photoionization threshold of anthracene in hexane has not been measured; however, it would be approximately equal to that of pentane, because both the conduction band energy [16] and the dielectric constant of the two solvents are approximately equal. Thus, we can expect that anthracene has a larger excess energy in 2,2,4-trimethylpentane than in hexane. Therefore, we can conclude that a larger value of the excess energy would offer better detection sensitivity in the laser two-photon ionization method.

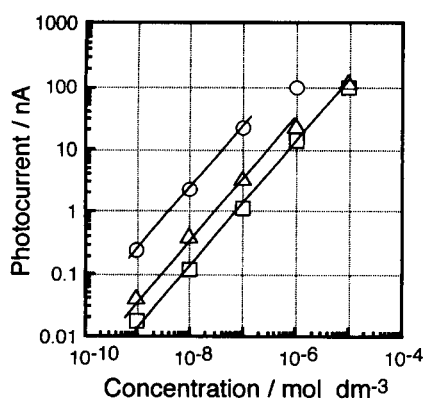

Fig. 8. Typical analytical curves of anthracene at three laser pulse energy values: ○, 2.5 mJ; △, 0.9 mJ; □, 0.7 mJ.

References

[1] S. Yamada and T. Ogawa, Prog. Anal. Spectrosc., 9 (1986) 429.
[2] T. Ogawa, Bunseki Kagaku, 42 (1993) 201.
[3] E. Voigtman, A. Jurgensen and J.D. Winefordner, Anal. Chem., 53 (1981) 1921.
[4] S. Yamada, K. Kano and T. Ogawa, Bunseki Kagaku, 31 (1982) E247.
[5] E. Voigtman and J.D. Winefordner, Anal. Chem., 54 (1982) 1834.
[6] S. Yamada, K. Hino, K. Kano and T. Ogawa, Anal. Chem., 55 (1983) 1914.
[7] S. Yamada, T. Ogawa and P. Zhang, Anal. Chim. Acta, 183 (1986) 251.
[8] T. Ogawa, K. Kise, T. Yasuda, H. Kawazumi and S. Yamada, Anal. Chem., 64 (1992) 1217.
[9] T. Ogawa, T. Yasuda and H. Kawazumi, Anal. Sci., 8 (1992) 81.
[10] T. Ogawa, T. Yasuda and H. Kawazumi, Anal. Chem., 64 (1992) 2615.
[11] K. Masuda, T. Inoue, T. Yasuda, K. Nakashima and T. Ogawa, Anal. Sci., 9 (1993) 297.
[12] T. Inoue, K. Masuda, K. Nakashima and T. Ogawa, Anal. Chem., 66 (1994) 1012.
[13] L. Onsager, Phys. Rev., 54 (1938) 554.
[14] J.M. Warman, in J.H. Baxendale and F. Busi (Eds.), The Study of Fast Processes and Transient Species by Electron Pulse Radiolysis, Reidel, Dordrecht, 1982, p. 433.
[15] G.R. Freeman, Ann. Rev. Phys, Chem., 34 (1983) 463.
[16] L.G. Christophorou and K. Siomos, in L.G. Christophorou (Ed.), Electron–Molecule Interactions and Their Applications, Vol. 2, Academic Press, New York, 1984, p. 221.

[17] S. Yamada, S. Yoshida, H. Kawazumi, T. Nagamura and T. Ogawa, Chem. Phys. Lett., 122 (1985) 391.
[18] K. Nakashima, M. Kise and T. Ogawa, Chem. Lett., (1992) 837.
[19] D.W. Tweenten and S. Lipsky, J. Phys. Chem., 93 (1989) 2683.
[20] Handbook of Chemistry, Vol. 2, 4th edn., Chemical Society of Japan, Maruzen, Tokyo, 1993, p. 415.
[21] R.S. Becker, in Theory and Interpretation of Fluorescence and Phosphorescence, Japanese edition, Tokyo Kagaku Doujin, Tokyo, 1972, p. 150.
[22] K. Nakashima, M. Kise and T. Ogawa, in preparation.

ELSEVIER

Analytica Chimica Acta 299 (1995) 361–369

ANALYTICA CHIMICA ACTA

Direct and indirect detection of liquid chromatography by infrared thermal lens spectrometry

Chieu D. Tran *, Guilan Huang, Victor I. Grishko

Department of Chemistry, Marquette University, Milwaukee, WI 53233, USA

Received 29 November 1993; revised manuscript received 5 January 1994

Abstract

A novel, sensitive and universal detector for liquid chromatography has been developed. This detector is based on the measurement of infrared absorption of effluents by the thermal lens effect. In this instrument, the chromatographic effluent was excited by infrared radiation derived from a solid-state tunable F-center laser. The heat generated as a consequence of the sample absorption of the infrared radiation was measured by a He–Ne monitoring laser whose beam was collinearly overlapped with the excitation infrared beam in the sample. The technique is universal because it can be used for the detection of compounds which have absorption in the infrared region (by direct detection) as well as non-absorbing compounds (by indirect detection). The sensitivity of the technique is directly proportional to the excitation laser power, and with the used of laser power of only 4.5 mW, the technique is at least ten times more sensitive than corresponding absorption detectors. A detection limit of picograms was achieved for phenol and its chloro substituents.

Keywords: Infrared spectrometry; Liquid chromatography; Phenol; Thermal lens detector

1. Introduction

Liquid chromatography (LC) has increasingly become the technique of choice for chemical separations. The popularity stems from the fact that with use of the appropriate stationary and mobile phases, all compounds can virtually be separated by this technique. As a consequence, there has been an increased demand for a universal detector which has the required sensitivity to detect all types of compounds.

Refractive index, absorption, fluorescence and electrochemical detection are currently used for LC [1–3]. While these detectors have shown to be effective, they all suffer limitations, namely they can only be used for certain types of compounds [1–3]. A truly universal detector for LC does not exist, although the refractive index detector comes close. The refractive index detector, however, is not very sensitive and is considered incompatible with gradient separations. It is, therefore, of particular importance that a detector that can be used for all types of compounds be developed.

A detector based on absorption measurement in the infrared (IR) region can, in principle, be a universal detector because virtually all compounds absorb in this region [2,3]. Unfortunately, this is not practically possible because of a variety of factors including the low sensitivity of present IR spectrometers and the IR absorption of the mobile phase [2,3]. The first limitation, i.e., low sensitivity of present IR techniques, is mainly due to the low output power of IR sources and the low sensitivity of IR detectors. Therefore, in principle, it may be possible to achieve higher sensitivity

* Corresponding author.

SSDI 0003-2670(94)00299-1

if the measurements are performed by use of either a new IR source with higher output power and a new sensitive detector and/or a new measurement principle that is much different from the conventional transmission measurements. While it is possible to achieve higher output intensity by use of IR lasers (e.g., F-center, CO or CO_2 laser) it is not possible to significantly enhance the detecting sensitivity if IR detectors are used. The reason for the latter stems from the fact that the sensitivities of currently available IR detectors are still significantly lower than that of the UV–visible detectors. It is thus evidently clear that the sensitivity of absorption measurements in the IR region can only be achieved if novel measurement techniques which are, in principle, different from the conventional transmission measurements and which do not rely on the use of IR detector, are used. Thermal lens is one of such possible techniques.

The thermal lens technique is based on the measurement of the temperature rise that is produced in an illuminated sample by non-radiative relaxation of the energy absorbed from a laser [4–14]. This novel technique should serve as an excellent means for sensitive measurements of absorption in the IR region. This is because in this technique, the absorbed optical energy is directly measured. As a consequence, its sensitivity is similar to that of the fluorescence technique and is relatively higher than that of conventional absorption measurements. In fact, it has been calculated and experimentally verified that the sensitivity of the thermal lens technique could be 237 times higher than that of conventional absorption techniques when a visible laser of only 50 mW was used for excitation [4–14]. Furthermore, the IR absorption, when determined by use of the thermal lens effect, can be measured sensitively with a visible-region detector. Specifically, thermal lens measurement is generally based on the pump and probe optical configuration, and in this system the signal is detected by a phase detection technique (at the chopping frequency of the pump beam) with a visible probe laser that not only has a relatively low noise level (compared with the IR pump source) but also can be sensitively detected with a visible-region photodiode. The second limitation, i.e., the interference of IR absorption by the mobile phase, can be ameliorated by use of the so-called indirect detection technique. Specifically, the measurement will be performed at the specific wavelength where the mobile phase has strong absorption but the analytes do not absorb. The sample is detected by their negative signals. That is the background signal due to the absorption of the mobile phase will be decreased when the sample is eluted out because the samples do not absorb at this wavelength.

The information presented is indeed provocative and clearly indicates that it is possible to synergistically use the thermal lens technique and the indirect detection method to develop a novel LC detector which is truly universal. Such considerations prompted us to initiate this study which aims to develop an LC detector based on thermal lens measurements in the IR region. This paper describes the instrumentation development for the first IR thermal lens LC detector. Preliminary results on the use of this detector for the comparison study between the direct (detection at wavelength where only the analytes absorb) and indirect (detection at wavelength where the mobile phase absorbs but the analyte do not) will also be reported.

2. Experimental

A schematic diagram of the IR thermal lens detector is shown in Fig. 1. The excitation beam was provided by an F-center laser (Model FCL-10, Burleigh, Rochester, NY, USA). This IR solid-state laser, which has output radiation from 2.4 to 3.5 μm, was pumped by a krypton laser (Model Innova 70K, Coherent, Palo Alto, CA, USA). The F-center laser was spectrally tuned by use of a computer-controlled stepping motor to rotate the intra-cavity grating. After being modulated at 314

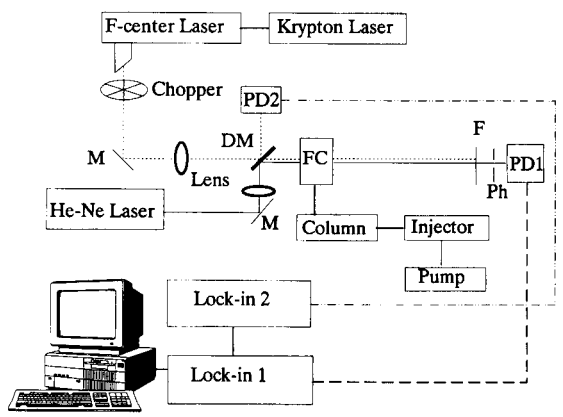

Fig. 1. Schematic diagram of the IR thermal lens detector for LC: M, mirror; DM, dichroic mirror; FC, microflow cell; F, interference filter; Ph, pinhole; PD, PIN photodiode; Lock-in, lock-in amplifier.

Hz by a mechanical chopper (Stanford Research Systems Model SR450) the excitation beam was focussed onto the sample by an LiF lens having a focal length of 120 mm. The probe beam, provided by a He–Ne laser (Spectra-Physics Model 154), was aligned to colinearly overlap with the pump beam at the sample by means of a dichroic mirror (DM) which was fabricated by a dielectrically coated CaF_2 substrate with a thin dielectric layer to reflect the 632.8-nm probe beam and to transmit all IR radiation. The cell used in this study was a chromatographic microflow cell (FC) equipped with quartz windows (ISCO Model 68-0080-011). This cell had a 5-mm pathlength and a 10-μl volume. The pump and probe beam were separated by an interference filter (F) which blocked the pump beam and transmitted the probe beam. The heat generated by the sample as a consequence of its absorption of the pump beam changed the intensity in the center of the probe beam. The intensity fluctuation of the probe beam was measured with a PIN photodiode (PD1, United Detector Technology Model PIN 10-DP) placed 2.0 m from the sample and behind the interference filter (F) and the pinhole (Ph). A lens with a focal length of 50 mm was used to focus the probe beam, and its relative distance to the sample was adjusted to give a maximum thermal lens signal. Demodulation and amplification of the thermal lens signal were accomplished by means of a lock-in amplifier (lock-in 1, Stanford Research Systems Model SR-510).

Similar to other spectrally tunable lasers (dye lasers, Ti-Sapphire laser), the output intensity of the F-center laser varies as a function of wavelength. It was necessary, therefore, to normalize the thermal lens signal to the intensity of the pump beam. This was accomplished by use of the small portion of the IR beam reflected from the dichroic filter as the reference for the pump beam. This reflected IR beam, as illustrated, is detected by a lead selenide detector (PD2). The output of this detector is fed into a lock-in amplifier (lock-in 2, Princeton Applied Research Model 5207) and the output of this lock-in amplifier is connected to the first lock-in in order to calculate the ratio of the thermal lens signal (output of lock-in 1) to the pump beam intensity (output of lock-in 2). The output which corresponds to the ratio value was then connected to a microcomputer (IBM AT compatible with 386 microprocessor, Northgate Computer Systems, Eden Prairie, MN, USA) through the A/D of the 12-bit DAS board (Metra-Byte, Taunton, MA, USA).

A Shimadzu isocratic pump (Model LC-600) was used to deliver the eluent. The sample was injected into the system through a Rheodyne Model 7125 sample injector valve equipped with a 20-μl loop. A 250 mm $\times$ 4.6 mm I.D. stainless-steel column packed with Nucleosil 5 silica (Cat. No. OOG-0321-EO, Phenomenex, Torrance, CA, USA) was used. Chromatograms obtained with the developed IR thermal lens detector were compared with those measured by using a conventional UV–visible absorption detector (Shimadzu SPD-6AV UV–visible variable-wavelength detector).

IR absorption spectra were taken on a Fourier transform IR (FT-IR) spectrophotometer (4020 Galaxy series, Mattson Instruments) using a variable pathlength cell fabricated from CaF_2 (International Crystal Laboratories, Garfield, NJ, USA). UV and visible absorption spectra were measured on a Shimadzu Model 1220 absorption spectrophotometer.

All compounds were obtained from commercial sources and used as received. Solvents were from Burdick and Jackson (Baxter Scientific, IL, USA) and deionized water was distilled from an all-glass distillation apparatus. The mobile phase was degassed and filtered through a membrane filter with a 0.45-μm pore size.

3. Results and discussion

3.1. Direct detection

The six compounds used in this study are phenol (PN), 2-chlorophenol (2-CL-PN), 3-chlorophenol (3-CL-PN), 4-chlorophenol (4-CL-PN), 2,4,5-trichlorophenol (TCL-PN) and pentachlorophenol (PCL-PN). These compounds were selected for this study because they are environmentally hazardous, namely they have been used as herbicides and are known to be toxic. The absorption spectra of these compounds in a carbon tetrachloride–acetonitrile (98:2, v/v) mixture, taken with a CaF_2 cell on the FT-IR spectrophotometer are shown in Fig. 2. For comparison the thermal lens spectra of these compounds were also taken, and the spectra obtained are shown in Fig. 3. It is clearly evident from these two sets of spectra that the IR thermal lens tech-

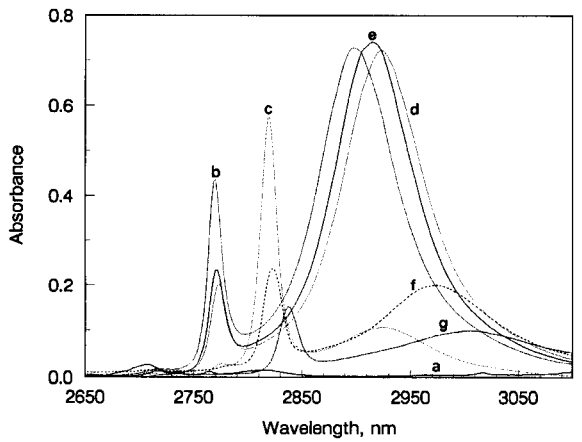

Fig. 2. IR absorption spectra of a 2:98 (v/v) mixture of acetonitrile–carbon tetrachloride (a), 2.76×10^{-2} M phenol (b), 1.87×10^{-2} M 2-chlorophenol (c), 2.02×10^{-2} M 3-chlorophenol (d), 2.18×10^{-2} M 4-chlorophenol (e), 9.12×10^{-2} M 2,4,5-trichlorophenol (f) and 6.76×10^{-3} M pentachlorophenol (g) in the above solvent mixture, taken with the FT-IR spectrophotometer.

nique not only is more sensitive but also has higher resolution than the FT-IR spectrometer. Also, as expected, the thermal lens spectra have shapes similar to those of the FT-IR spectra. The only difference between the two sets of spectra is the region between 2700 and 2800 nm where absorption bands were detected by the FT-IR spectrometer (Fig. 2) but are missing in the thermal lens measurement (Fig. 3). This

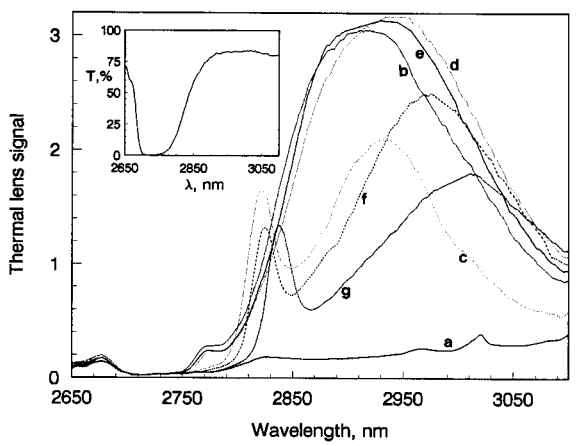

Fig. 3. Thermal lens spectra of a 2:98 (v/v) mixture of acetonitrile–carbon tetrachloride (a), 2.76×10^{-2} M phenol (b), 1.87×10^{-3} M 2-chlorophenol (c), 2.02×10^{-2} M 3-chlorophenol (d), 2.18×10^{-2} M 4-chlorophenol (e), 9.12×10^{-2} M 2,4,5-trichlorophenol (f) and 6.76×10^{-3} M pentachlorophenol (g) in the above solvent mixture, taken with the IR thermal lens spectrophotometer. The inset is the transmission spectrum of the chromatographic microflow cell used to take these spectra.

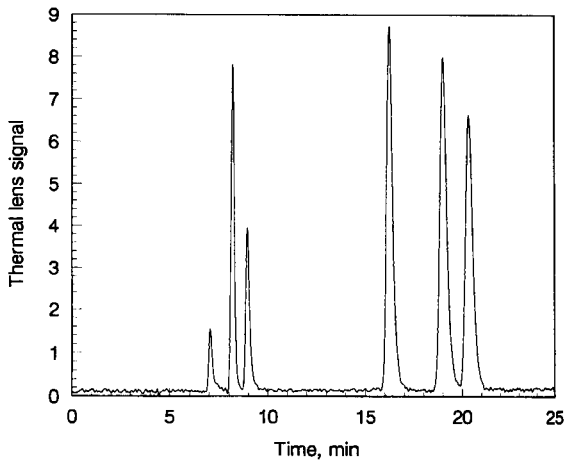

Fig. 4. Chromatogram of the mixture of phenol and its chloro substituents, taken with the IR thermal lens detector at 2925 nm. See text for chromatographic conditions.

discrepancy is due to the difference in the transparency of the two cells used for the measurements. A CaF_2 variable-pathlength cell, which is transparent throughout the measurement region, was used for the FT-IR measurements. The cell used in the thermal lens measurements was a chromatographic microflow cell (ISCO Model 68-0080-011) which was constructed from quartz windows. As illustrated in the inset of Fig. 3, because of the absorption of the quartz windows, this cell does not transmit in the 2700–2800 nm region. As a consequence, the thermal lens signal of the samples in this cell cannot be measured in this region.

It is evident from Figs. 2 and 3 that the mobile phase, which in this case was the 2:98 (v/v) acetonitrile–carbon tetrachloride mixture, has expectedly no absorption in this IR region. Therefore, the IR thermal lens spectrometer can be used for direct chromatographic detection with this mobile phase. Also from the figures, it seems that 2925 nm is the common wavelength where all six compounds can be sensitively detected. Accordingly, the IR excitation laser (i.e., the F-center laser) of the thermal lens detector was initially set at this wavelength and the chromatogram obtained is shown in Fig. 4 (this separation was obtained with a flow-rate of 0.8 ml min^{-1}). As illustrated, all six compounds were baseline-separated under these conditions and were sensitively detected at this wavelength. The retention times for each compound, confirmed by individually injecting the pure compound into the column using identical chromatographic conditions, were found to be

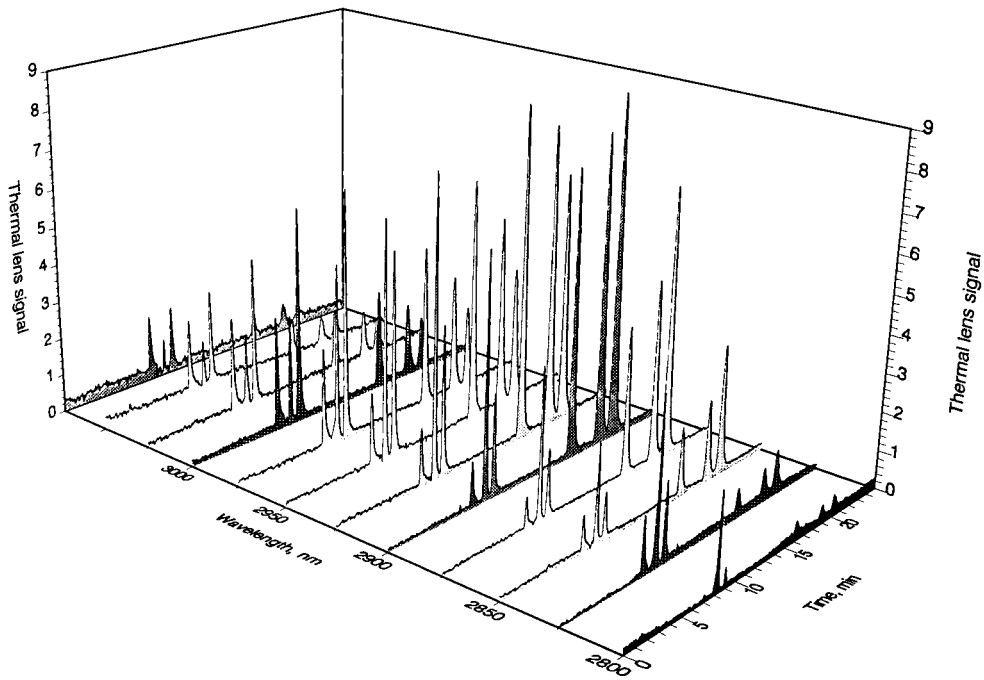

Fig. 5. Chromatograms of a mixture of phenol and its chloro substituents, taken at different wavelengths by the IR thermal lens detector. Chromatographic conditions were the same as those in Fig. 4.

7.02, 8.23, 8.95, 16.28, 18.96 and 20.40 min for PCL-PN, 2-CL-PN, TCL-PN, 3-CL-PN, 4-CL-PN and PN, respectively.

Chromatograms were also recorded at eleven different wavelengths ranging from 2800 to 3075 nm (Fig. 5). As expected, for each compound the intensity of the chromatogram varies as a function of the wavelength in a manner similar to its absorption spectrum (Fig. 2) and thermal lens spectrum (Fig. 3). It is also evident from these chromatograms that 2925 nm is the wavelength at which all six compounds can be sensitively detected. Consequently, this wavelength was used to determine the limits of detection (LODs) for two of the compounds, namely 3-CL-PN and 4-CL-PN, for this thermal lens detector. The chromatograms of 3-CL-PN and 4-CL-PN at different concentrations are shown in Fig. 6A and B, respectively. As expected, for each compound, the detected thermal lens signal intensity was found to be linearly proportional to the amount injected over two decades of concentrations, i.e., from 3.12×10^{-5} to 4.00×10^{-3} M (correlation coefficients for 3-CL-PN and 4-CL-PN were 0.998 and 0.999, $n=8$). Under these conditions (i.e., 4.5 mW of the 2925-nm excitation beam modulated at 314 Hz), the LODs, defined as twice the peak-to-peak noise of the baseline divided by the slope of the calibration graph, are estimated to be 3.4×10^{-7} and 5.1×10^{-7} M for 3-CL-PN and 4-CL-PN, respectively. These correspond to a mass detectability of 0.88 and 1.30 ng, respectively. Since the molar absorptivities of these two compounds at 2925 nm are 178.1 and 175.0 M^{-1} cm^{-1}, respectively, and the chromatographic microflow cell used has a pathlength of 5 mm, the LOD values above correspond to absorbance units of 3.0×10^{-5} and 4.4×10^{-5}.

To facilitate the evaluation of this IR thermal lens detector, chromatograms of the mixture of six compounds were also measured using the UV absorption detector (Shimadzu Model SPD-6AV UV–visible variable-wavelength detector). Since the wavelengths at which 3-CL-PN and 4-CL-PN have maximum absorption were found to be 275 and 282 nm, respectively, these wavelengths were used to determine the LODs for these two compounds. With the use of a chromatographic microflow cell having a 1-cm pathlength, the LODs were found to be 1.7×10^{-7} and 2.2×10^{-7} M for 3-CL-PN and 4-CL-PN, respectively. Based on molar absorptivities of 1812 M^{-1} cm^{-1} (for 3-CL-

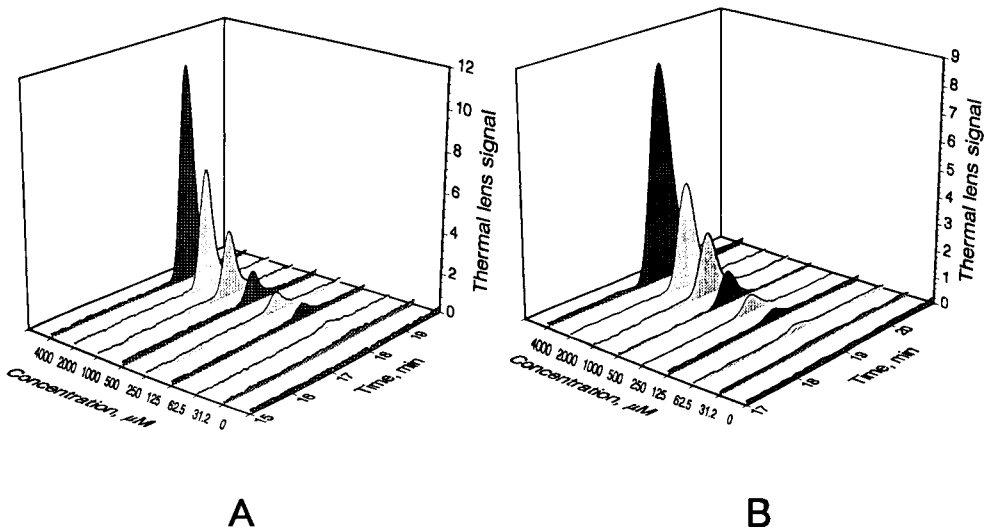

Fig. 6. Chromatograms of (A) 3-chlorophenol and (B) 4-chlorophenol at different injection concentrations, detected by the IR thermal lens detector at 2925 nm.

PN) and 1771 M^{-1} cm^{-1} (for 4-CL-PN), the LOD values above were calculated to correspond to absorbance values of 3.1×10^{-4} and 3.9×10^{-4}. These LODs are about ten times higher than the corresponding LODs obtained by the thermal lens detector. It is important to point out that the absorption detector used in this case operated in the UV region. Because the UV absorption technique is known to be more sensitive than the FT-IR technique, higher LOD values may be obtained if the FT-IR detector is used. Therefore, the sensitivity enhancement may be higher if the comparison between the thermal lens and the absorption is made in the same IR region. In addition to its high sensitivity, the present IR thermal lens detector is superior to the UV detector because it is based on the absorption measurement of the functional group of the analyte (e.g., the OH group in this work) and, hence, can be used for the detection of a variety of compounds (e.g., aromatic and aliphatic alcohols) whereas the UV absorption detector is only applicable to UV-absorbing compounds (only aromatic alcohols).

3.2. *Indirect detection*

While the IR thermal lens method has proven to be sensitive in the application above, it cannot be considered as a universal LC detector. This is because the method is based on the use of a mobile phase that does not absorb the excitation laser radiation. Unfortunately, only a few solvents are transparent in the IR region and these solvents (e.g., carbon tetrachloride) are either poor chromatographic solvents (only a few compounds are separated by use of these solvents as mobile phase) or too toxic to use. As a consequence, the IR thermal lens detector, in the application above, suffers from severe limitations. These limitations can be ameliorated by using the so-called indirect detection technique. Specifically, the thermal lens measurements will be performed at a wavelength where the mobile phase strongly absorbs but the analytes do not absorb. The thermal lens signal of the mobile phase will be decreased when the sample is eluted and the sample is, therefore, detected by the "negative" signal.

The mobile phase used for this indirect detection is a 95:5 (v/v) mixture of cyclohexane–methylene chloride. The FT-IR spectrum of a 10% (v/v) solution of this mobile phase in carbon tetrachloride is shown in Fig. 7 together with the spectra of the 0.25 M carbon tetrachloride solutions of 2-CL-PN, DCL-PN, TCL-PN and PCL-PN. As illustrated, the mobile phase has a strong absorption in the whole region from 3100 to 3325 nm. It is important to point out that the mobile phase used to measure the spectrum shown in Fig. 7 was not a neat solution but rather only a 10% solution in carbon tetrachloride. The corresponding absorption spectrum of this solvent mixture, when used as the mobile phase for LC, will be ten times higher than that shown in Fig. 7. It will, therefore, overshadow the

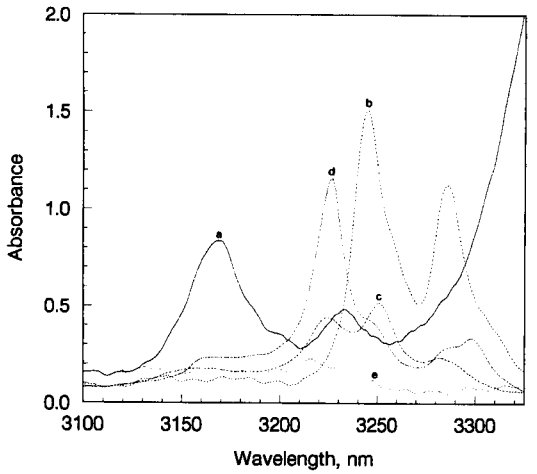

Fig. 7. IR absorption spectra of a 10% (v/v) solution of a 95:5 (v/v) cyclohexane– methylene chloride mixture in carbon tetrachloride (a), and 0.25 M carbon tetrachloride solution of 2-chlorophenol (b), 2,4-dichlorophenol (c), 2,4,5-trichlorophenol (d) and pentachlorophenol (e).

absorption of the analytes that are present in the chromatographic separations at concentrations much lower than the 0.25 M shown in Fig. 7. As a consequence, this mobile phase can be used for the indirect detection of these four compounds in this wavelength region (i.e., from 3100 to 3325 nm). Fig. 8 shows the results obtained by use of the IR thermal lens detector to record the chromatograms of these four compounds at 3100, 3150, 3200, 3250, 3275, 3300 and 3325 nm. In this figure, the chromatograms obtained were reversed in order to increase the clarity (notice the negative scale of the vertical axis). The elution order of these four compounds was found to be PCL-PN (17.5 min), 2-CL-PN (21.0 min), DCL-PN (22.7 min) and TCL-PN (26.7 min). It is evident from these chromatograms that 3275 nm is the best wavelength for the sensitive detection of these compounds. This is as expected because from Fig. 7 it is clear that the absorption of the four compounds is minimal at 3275 nm. Accordingly, 3275 nm was used to construct the calibration graph for PCL-PN. A very good linear relationship was found between the concentration and signal intensity (correlation coefficient was -0.9987). The calibration line has a negative slope ($-1.63\times10^{-2}\pm4.8\times10^{-4}$ mV mol^{-1} l) because in this case the (thermal lens) signal (of the mobile phase) is highest when the analyte is absent. From this calibration, the LOD was estimated to be 6.02×10^{-5} M which corresponds to a mass detectability of 320 ng. This LOD value is about 64 times higher than that obtained for the same compound using the direct detection method. This is as expected because the background signal of the indirect detection is the thermal lens signal of the mobile phase which is

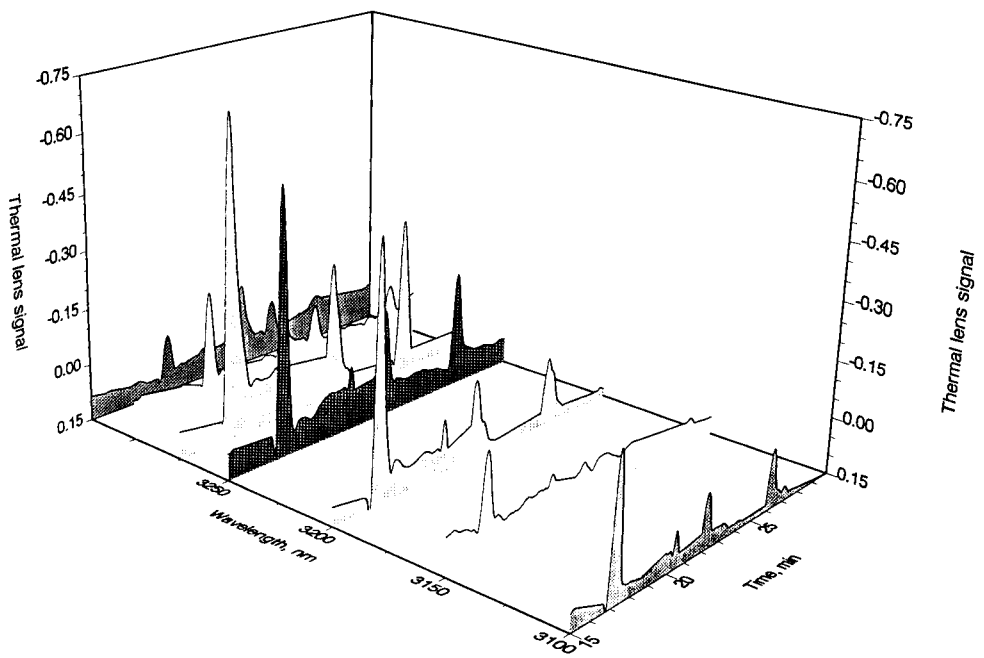

Fig. 8. Chromatograms of a mixture of phenol and its chloro substituents, taken at different wavelengths by the IR thermal lens detector.

the highest signal (compared to signals when analytes are present). This background signal is much higher than that for direct detection (which should be zero). The associated background noise, therefore, is higher for indirect detection than for direct detection. Consequently, the LOD for the indirect method is higher than for the direct method.

Taken together, the results presented clearly demonstrate that LC detection in the IR region can be sensitively performed by use of the thermal lens technique. This IR thermal lens detection method is universal since it can be used for the detection of compounds that have absorption bands in the IR region (by direct detection) and compounds that do not have any absorption in the IR region (by indirect detection). Unlike the refractive index detector, this detector is applicable not only to isocratic but also to gradient separations. This is because in the thermal lens technique, the IR pump beam is focussed into the sample cell and the detector is much smaller than the probe beam (at the detector). In consequence, any change in the solvent composition due to the gradient elution will not produce any drift in the baseline because the pump beam is still focussed in the sample and the position of the (relatively large) probe beam on the (small) detector is unchanged (the only observable change is the magnitude of the thermal lens signal). Compared with indirect UV absorption detection, this IR thermal lens detector has a much wider application. This is because, except for a few metal ions, all compounds have absorption either only in the UV region, in both the UV and visible regions or do not absorb at all in any region. UV absorption bands are relatively wide so that indirect UV detection may not be possible for some compounds without adding other species. Conversely, IR absorption bands are much narrower and, as a consequence, the IR thermal lens detector, in the indirect mode, can detect virtually all compounds without the need to add any other species. The sensitivity of the IR thermal lens method and the spatial characteristic of the laser beam (i.e., it can be focussed to a diffusion-limited spot) render it feasible to use the method for detection in capillary electrophoresis.

As described above, the sensitivity of this novel IR thermal lens detector in the direct detection mode was experimentally determined to be about ten times greater than that of conventional absorption measurements in the UV region. The sensitivity is enhanced because in this thermal lens technique the signal intensity is directly proportional to that of the excitation laser power. As a consequence, its sensitivity is much higher than that of transmission measurements. Theoretically, this can be seen in the enhancement factor (E) which is the enhancement in the sensitivity over transmission measurements [6]:

$$E = \frac{P(\mathrm{d}n/\mathrm{d}T)}{1.91\lambda k} \quad (1)$$

where P is the excitation laser power, k and $(\mathrm{d}n/\mathrm{d}T)$ are the thermal conductivity and temperature coefficient of the refractive index of the solvent, and λ is the wavelength of the probe beam.

By use of this equation the sensitivity enhancement for the mobile phase (2:98 acetonitrile–carbon tetrachloride mixture) which has and $\mathrm{d}n/\mathrm{d}T$ and k values of 5.5×10^{-4} K^{-1} and 1.20 mW cm^{-1} K^{-1}, respectively [12,15], was calculated to be about 17 (higher than conventional transmission) for an excitation IR laser of only 4.5 mW (modulated with a chopper with a 50–50 duty cycle at a 314-Hz frequency). The experimental enhancement factor of 10 is relatively lower than the calculated value of 17. A variety of reasons may account for this discrepancy but the most likely one is probably the fact that the calculated enhancement factor is based on the use of a steady-state thermal lens signal whereas in the chromatographic experiments, the thermal lens signals were measured at 314 Hz, i.e., before the sample reached the steady state.

Acknowledgements

The authors are grateful to the National Institutes of Health, National Center for Research Resources (Bethesda, MD) for financial support of this work.

References

[1] E.S. Yeung, Detectors for Liquid Chromatography, John Wiley, New York, 1986.
[2] C. Parriott, in D. Parriott (Ed.), A Practical Guide to HPLC Detection, Academic Press, New York, 1993, Ch. 9, pp. 233–288.
[3] V.F. Kalasinsky and K.S. Kalasinsky, in G. Patonay (Ed.), HPLC Detection: Newer Methods, VCH Publishers, New York, 1992, Ch. 7, pp. 127–162.

[4] N.J. Dovichi, CRC Crit. Rev. Anal. Chem., 17 (1987) 357.
[5] C.D. Tran, in D. Bicanic (Ed.), Photoacoustic and Photothermal Phenomena III, Springer Verlag, Berlin, 1992, pp. 463–473.
[6] C.D. Tran, in G. Patonay (Ed), HPLC Detection: Newer Methods, VCH Publisers, New York, 1992, Ch. 6, pp. 111–126.
[7] C.D. Tran, Anal. Chem., 60 (1988) 182.
[8] C.D. Tran and T.A. Van Fleet, Anal. Chem., 60 (1988) 2478.
[9] M. Franko and C.D. Tran, Anal. Chem., 60 (1988) 1925.
[10] M. Franko and C.D. Tran, Appl. Spectrosc., 43 (1989) 661.
[11] C.D. Tran, Appl. Spectrosc., 40 (1987) 512.
[12] M. Franko and C.D. Tran, J. Phys. Chem., 95 (1991) 6688.
[13] C.A. Carter, J.M. Brady and J.M. Harris, Appl. Spectrosc., 36 (1982) 309.
[14] S.L. Nikolaisen and S.E. Bialkowski, Anal. Chem., 56 (1985) 758.
[15] J.A. Riddick, W.B. Bunger and T.K. Sakano, Organic Solvents—Physical Properties and Methods of Purification, Wiley, New York, 1986.

ELSEVIER

Analytica Chimica Acta 299 (1995) 371–375

ANALYTICA CHIMICA ACTA

Separation of polycyclic aromatic hydrocarbons by micellar electrokinetic chromatography with laser fluorescence detection

Takashi Kaneta, Tetsuya Yamashita, Totaro Imasaka *

Department of Chemical Science and Technology, Faculty of Engineering, Kyushu University, Hakozaki, Fukuoka 812, Japan

Received 25 January 1994; revised manuscript received 21 April 1994

Abstract

Polycyclic aromatic hydrocarbons (PAHs) were separated by micellar electrokinetic chromatography and were detected by laser fluorometry. The PAHs with large molecular weights were separated by using dimethylformamide as an organic modifier. A He–Cd laser (325 nm, 5 mW) or a blue semiconductor laser (415 nm, 50 μW) was used as an exciting light source. The detection limit ($S/N = 3$) for perylene was 1.4×10^{-7} M under He–Cd laser excitation or 3.4×10^{-7} M under semiconductor laser excitation.

Keywords: Chromatography; Fluorimetry; Laser spectroscopy; PAHs; Micellar electrokinetic chromatography

1. Introduction

Many kinds of polycyclic aromatic hydrocarbons (PAHs) exist in the environment, and some of them are strongly carcinogenic. Thus PAHs must be separated prior to detection at trace levels. Micellar electrokinetic chromatography (MEKC) is an excellent separation technique, because of its high resolving power [1,2]. Furthermore, MEKC has a potential to accomplish ultra-sensitive detection, because of a small sample amount injected. Absorbance spectrometry is most frequently used, but the detection limit reported is limited to 10^{-5} M levels. More sensitive detection in MEKC is achieved by laser-induced fluorometry [3].

One of the problems in MEKC is a difficulty in separation of hydrophobic compounds. For example, large PAHs are so hydrophobic that they are completely incorporated into the micelle, and are not separated by conventional MEKC. In order to solve this problem, a few attempts have been performed, e.g., addition of cyclodextrin [4,5] or of an organic modifier [6–9] in the carrier solution. We have already reported the separation of anthracene derivatives and several other PAHs as well by addition of cyclodextrin to the mobile phase [3,10]. However, it is difficult to separate PAHs with large molecular weights, since they cannot be included in cyclodextrin. Another approach to separate large hydrophobic compounds is to use hydrophilic micelles. Nishi et al. [11,12] have reported that bile salts form more hydrophilic micelles than sodium dodecylsulfate currently used in MEKC. Thus bile salts increase the polarity of the micellar phase, and then they decrease

* Corresponding author.

SSDI 0003-2670(94)00317-3

the capacity factor even for a strongly hydrophobic compound. Cole et al. [13] have also reported that bile salts are effective to improve the resolution of PAHs.

In this study, we report on the separation of PAHs with relatively large molecular weights by using a bile salt, sodium deoxycholate, as a surfactant and an organic solvent, dimethylformamide, as an organic modifier. Dimethylformamide was clarified to be an effective modifier to improve the resolution of PAHs. Six PAHs, containing structural isomers, were detected by using a HeCd laser. A similar study was conducted using a blue semiconductor laser.

2. Experimental

2.1. Apparatus

The fluorescence detection system has been described in Refs. [9,10]. A He–Cd laser (Omnichrome, Model 356-2S; 325 nm, 5 mW) or a blue semiconductor laser (Matsushita, Tokyo, IMSO0820-04; 415 nm, 50 μW) was used as an exciting light source. The sample was injected into the capillary (GL sciences, Tokyo, 50 μm i.d., 375 μm o.d.) filled with a buffer solution by a siphon method; the inlet side of the capillary was dipped into the sample solution which was raised typically 4 cm above the outlet side of the solution for 5–10 s. Platinum wires are immersed into both sides of the buffer solutions as electrodes to apply a high potential (typically 20 kV). A high voltage power supply, Model HCZE-30PN0.25 (Matsusada Precision Devices, Shiga), was used to apply a high potential. Fluorescence was detected 10 cm from the end of the capillary, at which the polyimide coating was burned off by a flame. All experiments were performed at room temperature.

2.2. Reagents

All reagents used were of analytical grade. Benzo[*a*]pyrene, dibenz[*a*,*h*]anthracene, and 2,3-benztriphenylene were obtained from Tokyo Kasei Kogyo (Tokyo). Fluoranthene, pyrene and sodium deoxycholate were purchased from Wako (Osaka). Perylene was obtained from Aldrich (Milwaukee, WI). Sodium deoxycholate was used as a surfactant. Dansyl amines (dns amines) were used for determination of the migration time of the micelle [14]. Dansylation of amines was performed according to the literature [15]. A typical sample solution contained 1×10^{-5} M of each dns amine in methanol. A carrier solution was prepared as follows: 1.75 mmol of sodium deoxycholate was dissolved in water, and then 0.5 ml of 1 M tris(hydroxymethy)aminomethane (Tris), 0.25 ml of 1 M sodium dihydrogenphosphate, and the specified amount of organic modifier were added to this solution in turn. The solution was finally made up to 25 ml with water. Thus the concentration was 70 mM for sodium deoxycholate, 20 mM for Tris, and 10 mM for sodium dihydrogenphosphate.

3. Results and conclusion

3.1. Separation of PAHs

The resolution, *Rs*, in MEKC is given by [2]

$$Rs = \frac{N^{1/2}}{4}\left(\frac{\alpha - 1}{\alpha}\right)\left(\frac{k'_2}{1 + k'_2}\right)\left(\frac{1 - t_0/t_{mc}}{1 + (t_0/t_{mc})k'_1}\right) \quad (1)$$

where N is the plate number, k'_1 and k'_2 are the capacity factors of the samples, t_0/t_{mc} is the elution range, and α is the separation factor which is equal to k'_2/k'_1. It has been reported that the optimum resolution is achieved when a capacity factor lies between 0.84 and 5.4 [2]. On the other hand, a larger separation factor is favorable to attain better peak resolution. Thus, it is necessary to optimize both the capacity factor and the separation factor simultaneously for best separation.

Hydrophobic compounds such as PAHs tend to be completely incorporated into micelles and cannot be separated by conventional MEKC. The capacity factor achieved in this condition is > 100, and they are far beyond the optimum. Addition of an organic modifier to the carrier solution improves the resolution of PAHs by decreasing the capacity factor. Previously, we have found that acetonitrile and dimethylformamide are effective modifiers to decrease the capacity factor for several hydrophobic

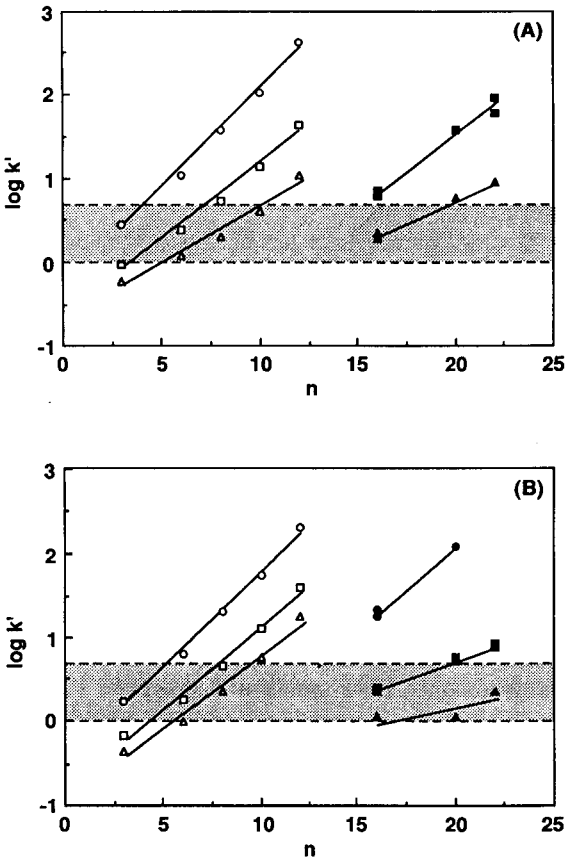

Fig. 1. Relationship between number of carbon atoms (n) and logarithm of capacity factor (k') for dns amine and PAH. The value of n is the number of carbon atoms in the aliphatic hydrocarbon for dns amine and the number of all carbon atoms in the molecule for PAH. (A) Acetonitrile, (B) dimethylformamide. (●, ○) 10%, (■, □) 20%, (▲, △) 30%. Open marks; dns amine, closed marks; PAH. The range enclosed by a mesh is the range of an optimum capacity factor. The data of 10% acetonitrile are not given in the figure. This is due to the fact that PAHs are not separated by MEKC.

compounds [16]. So, we first investigated change in the retention time of PAHs by addition of these organic modifiers.

It is well-known that there is a linear relationship between log k' and the number of carbon atoms in homologues in liquid chromatography and its slope represents the logarithm of the separation factor. Nishi et al. [12] have reported that such a linear relationship is also satisfied in MEKC. Fig. 1 shows the observed relationships between log k' and the number of carbon atoms for dns amines, indicating the validity of their study. Fig. 1 also shows that the relationship is linear for PAHs as well as that for dns amines. Thus the separation factor can be discussed in the similar manner even for PAHs. The separation factor deceases with increasing the concentration of the organic modifiers for both dns amines and PAHs. However, acetonitrile decreased the separation factor of dns amines more efficiently, while the separation factor of PAHs was more strongly affected by dimethylformamide. The decrease in the separation factor is caused by reducing the difference of polarities in the mobile and pseudostationary phases. The polarity influences the intensity of the interaction between the sample and solvent molecules in four ways, dispersion, dipole, hydrogen bonding and dielectric interaction [17]. Thus the separation factor would reflect the interaction between the sample and solvent molecules; the stronger interaction provides a smaller separation factor. Fig. 1 indicates that acetonitrile interacts more strongly with aliphatic hydrocarbons but more weakly with PAHs than dimethylformamide. In the preliminary study, it was found that PAHs were easily dissolved in dimethylformamide. These facts imply that the interaction between PAHs and dimethylformamide would be relatively strong.

The decrease in the separation factor by using an organic modifier is unfavorable for resolution of the sample (cf. Eq. 1), but it is unavoidable to decrease the capacity factor (cf. Fig. 1). Thus the experimental condition must be carefully optimized. From Fig. 1, possible candidates for optimum conditions are (1) 20% dimethylformamide and (2) 30% acetonitrile. Fig. 2 shows a chromatogram for a mixture sample containing six PAHs, which was obtained by using a carrier solution containing 20% dimethylformamide. Isomers such as fluoranthene–pyrene, perylene–benzo[a]pyrene, and 2,3-dibenztriphenylene–dibenz[a,h]anthracene were completely separated by using dimethylformamide as an organic modifier. These PAH isomers could not be separated by cyclodextrin-modified MEKC. Thus dimethylformamide was a very useful modifier to separate PAHs. A similar work was also performed by using 30% acetonitrile as an organic modifier. However, the isomers could not be separated completely.

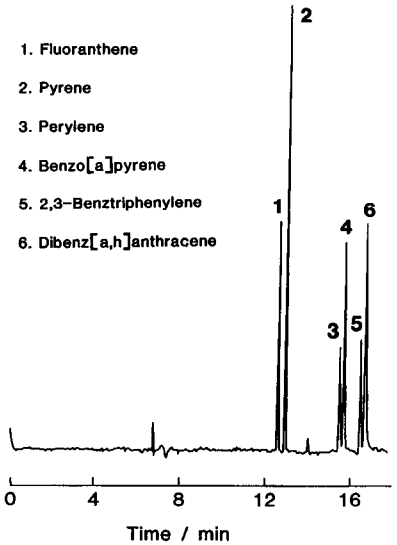

Fig. 2. Chromatogram for a mixture sample containing six PAHs obtained using the He–Cd laser. The concentration is 1×10^{-5} M for each sample. Capillary length, 60 cm; migration voltage, 20 kV.

3.2. Detectability

Table 1 shows the detection limits measured for the PAHs. The values obtained in this study (4.6×10^{-8}–1.4×10^{-7} M) are similar to that obtained by conventional fluorometry (2.8×10^{-8} M for perylene in open-tubular capillary liquid chromatography [18]). However, the values were inferior to those reported for cyclodextrin-modified MEKC [3] and capillary zone electrophoresis [19], though the resolution was greatly improved in the present method. The poor detection limits were attributed to a large background signal occurring from the carrier solution; deoxycholate used as a surfactant emitted weak fluorescence when a He–Cd laser was used as an exciting source. It is interesting to note that the fluorescence intensity of deoxycholate decreases with increasing concentration of dimethylformamide; the background signal decreased to half of the original intensity by increasing the concentration of dimethylformamide to 40%.

In order to decrease the background signal, the He–Cd laser was replaced with the blue semiconductor laser. The background signal was greatly decreased by using this laser, since the emitting wavelength is located at 415 nm and is far from the exciting maximum of deoxycholate (334 nm). Fig. 3 shows a chromatogram for a sample containing perylene and 2-aminoanthracene. The detection limit was 3.4×10^{-7} M for perylene. This value is similar to that obtained by using the He–Cd laser, nevertheless the output power of the blue semiconductor laser (50 μW) is two orders of magnitudes smaller than that of the He–Cd laser (5 mW). Unfortunately, none of the PAHs measured in Fig. 1 could be detected except perylene, since the emitting wavelength of the blue laser was too long to excite them. However, the blue laser is very practical since it is more compact than not only conventional lasers but also conventional light sources and can easily be operated without any maintenance. Furthermore, the blue laser is more advantageous than the conventional light source when the focusing capability and monochromaticity of the laser are successfully used, e.g., the monochromatic light can be easily eliminated from fluorescence. A blue laser with an output power of 40 mW has

Table 1
Detection limits of PAHs

Compound	Detection limit [a] (M)
Fluoranthene	8.9×10^{-8}
Pyrene	4.6×10^{-8}
Perylene	1.4×10^{-7}
Benzo[*a*]pyrene	8.7×10^{-8}
2,3-Benztriphenylene	1.4×10^{-7}
Dibenz[a,h]anthracene	1.3×10^{-7}

[a] $S/N=3$.

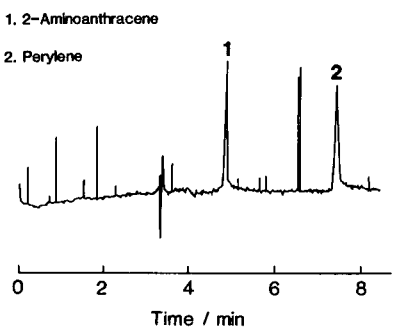

Fig. 3. Chromatogram for a mixture sample containing two PAHs obtained by using blue semiconductor laser. The sample concentration is 1×10^{-4} M for 2-aminoanthracene and 1×10^{-5} M for perylene. Capillary length, 50 cm; migration voltage, 25 kV.

already been developed [20], thus the sensitivity will be improved in the future.

4. Conclusions

The PAHs with large molecular weights were separated by MEKC and were measured by laser-induced fluorometry. The resolution could be controlled by changing the concentrations of sodium deoxycholate used as a surfactant and of dimethylformamide used as an organic modifier. Several PAH isomers, which could not be separated by cyclodextrin-modified MEKC, were readily separated by the present approach. The detection limits of the PAHs were 10^{-7}–10^{-8} M levels, which were similar to those obtained by conventional fluorometry. Thus MEKC combined with laser-induced fluorometry was useful for trace analysis of PAHs. The sensitivity was determined by a large background signal occurring from sodium deoxycholate, when a He–Cd laser was used as an exciting source. On the other hand, the sensitivity was determined by the output power of the laser, when a blue semiconductor laser was used instead.

References

[1] S. Terable, K. Otsuka, K. Ichikawa, A. Tsuchiya and T. Ando, Anal. Chem., 56 (1984) 111.
[2] S. Terabe, K. Otsuka and T. Ando, Anal. Chem., 57 (1985) 834.
[3] T. Imasaka, K. Nishitani and N. Ishibashi, Anal. Chim. Acta, 256 (1992) 3.
[4] S. Terabe, Y. Miyashita, O. Shibata, E.R. Barnhart, L.R. Alexander, D.G. Patterson, B.L. Karger, K. Hosoya and N. Tanaka, J. Chromatogr., 516 (1990) 23.
[5] T. Ueda, F. Kitamura, R. Mitchell, T. Metcalf, T. Kuwana and A. Nakamoto, Anal. Chem., 63 (1991) 2979.
[6] K. Otsuka, S. Terabe and T. Ando, Nippon Kagaku Kaishi, 7 (1987) 950.
[7] A.T. Balchunas and M.J. Sepaniak, Anal. Chem., 59 (1987) 1466.
[8] A.T. Balchunas and M.J. Sepaniak, Anal. Chem., 60 (1988) 617.
[9] R.D. Holland and M.J. Sepaniak, Anal. Chem., 65 (1993) 1140.
[10] T. Imasaka, K. Nishitani and N. Ishibashi, Analyst, 116 (1991) 1407.
[11] H. Nishi, T. Fukuyama, M. Matsuo and S. Terabe, J. Chromatogr., 498 (1990) 313.
[12] H. Nishi, T. Fukuyama, M. Matsuo and S. Terabe, J. Chromatogr., 513 (1990) 279.
[13] R.O. Cole, M.J. Sepaniak, W.L. Hinze, J Gorse and K. Oldiges, J. Chromatogr., 557 (1991) 113.
[14] Y. Tapuhi, D.E. Schmidt, W. Lindner and B.L. Karger, Anal. Biochem., 115 (1981) 123.
[15] M.M. Bushey and J.W. Jorgenson, J. Microcolumn Sep., 1 (1989) 125.
[16] T. Kaneta, T. Yamashita and T. Imasaka, Electrophoresis, in press.
[17] L.R. Snyder and J.J. Kirkland, Introduction to Modern Liquid Chromatography, Wiley, New York, 1979.
[18] E.J. Guthrie and J.W. Jorgenson, Anal. Chem., 56 (1984) 483.
[19] S. Nie, R. Dadoo and R.N. Zare, Anal. Chem., 65 (1993) 3571.
[20] W.J. Kozlovsky, W. Lenth, E.E. Latta, A. Moser and G.L. Bona, Appl. Phys. Lett., 56 (1990) 2291.

ELSEVIER

Analytica Chimica Acta 299 (1995) 377–385

ANALYTICA CHIMICA ACTA

Dynamics of matrix-assisted laser desorption as revealed by the associated acoustic signal

Theodore W. Heise, Edward S. Yeung *

Ames Laboratory, USDOE and Department of Chemistry, Iowa State University, Ames, IA 50011, USA

Received 14 December 1994; revised manuscript received 28 January 1994

Abstract

Some characteristics of the commonly used ultraviolet matrices for matrix-assisted laser desorption were determined, including solubilities in methanol and solid-phase absorption spectra. Differences between frontside and rearside desorption geometries are observed. Acoustic and quartz crystal microbalance signals were investigated as possible means of quantification of the amount of material vaporized by each laser pulse. Evidence for the existence of desorption thresholds is presented. Threshold values were determined to be in the 2–3 MW/cm^2 range.

Keywords: Acoustic methods; Piezoelectric sensors; Laser desorption

1. Introduction

In brief, matrix-assisted laser desorption (MALD) is the method [1] of dispersing a biopolymer of interest in a large excess of a matrix. The mixture is irradiated with a laser pulse and vaporizes. Analyte ions are formed and then detected by mass spectrometry (MS). The MALD process has been demonstrated to be a collective event with little or no signal present below a certain threshold laser irradiance [2], usually in the 1–10 MW/cm^2 range. The process, although relatively poorly understood, is known to be a bulk process rather than a monolayer event [3]. A number of models have been proposed for the MALD process [4–7].

Whatever the mechanism may be, one can certainly say MALD has proven to be of great utility in the MS analysis of otherwise intractable biopolymers [8]. Peptides [9], proteins [10], oligosaccharides [11], oligonucleotides [12], and even double-stranded DNA [13] have been converted to gas-phase ions for mass analysis by this method. The greatest utility has been for molecular weight determinations of proteins [14], since fragmentation of the parent ion rarely occurs.

In general two laser desorption geometries are possible: frontside and rearside [15,16]. It has been shown that laser-generated plumes can significantly attenuate the laser energy delivered to that surface [17]. Therefore rearside desorption tends to minimize plasma effects due to interaction of the desorption laser with the vaporized sample. A knowledge of the amount of material removed with each laser pulse may prove to be useful for understanding the vaporization dynamics. The large amount of material removed in IR-MALD has made direct microscopic estimation of sample removal possible [18]. However, in typical UV-MALD work, the small amount of material removed per laser pulse (typically ≤ 10 amol [18]) is difficult to quantify [19].

* Corresponding author.

SSDI 0003-2670(94)00309-2

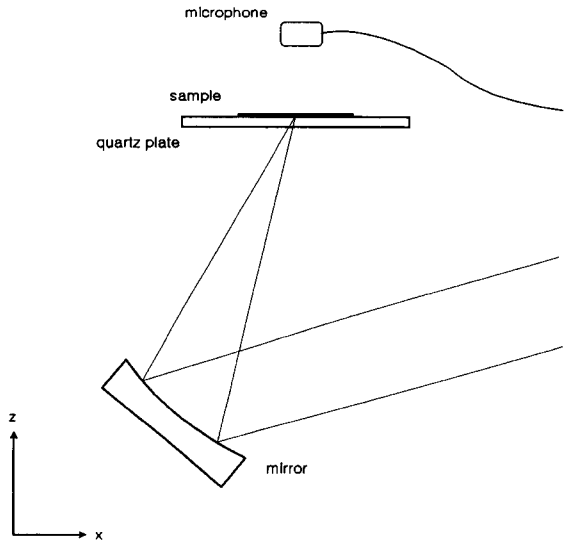

Fig. 1. Block diagram for acoustic monitoring of MALD.

The goal of this work is to use the piezoelectric quartz crystal "microbalance" (QCM) and the acoustic signal associated with vaporization to independently measure mass changes in MALD events. Through use of the Sauerbray equation, [20] changes in crystal mass can be determined from the measured frequency changes. This relationship can be extended to encompass mass changes in films of material in intimate contact with the crystal. The QCM typically exhibits a Gaussian-type response with the center having the highest degree of sensitivity [21,22]. For that reason, all experiments here were performed at the electrode center. Previous work in our group has demonstrated that laser ablation generates an acoustic signal which is directly proportional to the amount of material removed [23,24]. This effect has been observed in other laboratories as well [25]. It would be interesting to evaluate the applicability of the acoustic signal for quantification in MALD.

2. Experimental

A nitrogen laser (EMG 101, Lambda Physik) was used for sample desorption. The desorption setup for the rearside geometry is shown in Fig. 1. A cylindrical concave mirror was used to focus the beam to a line. Measurements from burn spots on photographic film and vaporized samples showed the irradiated area to be 0.5 mm × 6 mm. There were several reasons for using this configuration. First, this focusing arrangement was found to give the most uniform beam profile. Second, this setup was also found to yield the highest irradiance. Finally, a line was used rather than a point to increase the probe pathlength within the plume for fluorescence studies [26]. The laser was operated at low repetition rates (~ 0.5 Hz) with a shutter manually opened to admit a single laser pulse. Therefore, each set of data collected was for a single desorption event. It should be stressed here that unlike the majority of MALD work, no signal averaging was done. Laser fluence was varied by placing glass plates at 45° angles in the beam path. This allowed up to an order of magnitude beam attenuation in 15–20% increments.

Desorption of samples was carried out at atmospheric pressure without any special enclosures. The pulse energy was monitored by directing a partially reflected portion of the desorption beam to an energy probe (Models Rj-7200 and Rjp734, Laser Precision, Utica, NY, USA). Typical pulse energies ranged from 1 to 4 mJ at the desorption site with pulse widths of ~ 20 ns. Samples were prepared on quartz plates. The efficiency of sample desorption was checked by visual inspection of the films using a microscope.

Matrices were chosen based on previous utility in UV-MALD, and were obtained from Aldrich. All matrices were used as received. The matrices are listed in Table 1. All solutions were prepared in methanol

Table 1
Properties of various matrix materials at 337 nm

Matrix	MW (g/mol)	Solution ϵ ($l\ mol^{-1}\ cm^{-1}$)	Film ϵ ($l\ mol^{-1}\ cm^{-1}$)	Desorption threshold (MW/cm^2)
Anthranilic acid	137.14	3300	2700	1.93 (0.23)
Caffeic acid	180.16	8400	3000	2.93 (0.27)
Ferulic acid	194.19	8000	9500	2.00 (0.20)
Gentisic acid	154.12	3100	2800	2.96 (0.20)
Sinapinic acid	224.21	11000	9700	1.95 (0.37)

unless stated otherwise. To generate the thickest possible films, saturated solutions of matrix were needed. Solubilities were determined by repetitively adding volumes of methanol to a known mass of sample until no solid remained. With the exception of the QCM work, samples were always prepared on $2\times2\times1/16$ in. quartz plates. In order to have a reliable estimate of the amount of material desorbed, the most uniform sample films were desired. In the end, spin-coating from alcoholic solutions was found to give the most uniform films up to a maximum thickness of $\sim$700 nmol/cm^2. For the acoustic studies, all samples were prepared by spin-coating 10-μl aliquots of methanolic solutions. The spin-coater was home-built and operated at 800 r.p.m. For the QCM experiment, sample films were cast by depositing 1-μl aliquots directly onto the electrode surface. The films formed matched the electrode area nearly exactly. They were rather uniform albeit less so than with spin-coating.

Matrix solubilities ranged between 0.1 and 0.5 M. Ferulic and sinapinic acid solubilities were 0.5 M. Caffeic acid was soluble up to about 0.25 M. Gentisic acid had lower solubility at 0.1 M. The solubility of anthranilic acid was not determined. Film thicknesses were determined from the concentration and volume of solution deposited. With this knowledge and the assumption of uniform film distribution, measurement of the area of the film allowed calculation of the film thickness. Implicit in the uniformity assumption is the further assumption that the analyte was dispersed uniformly throughout the matrix. At these low concentrations, the analyte is not expected to alter the dynamics of desorption. Film thicknesses were estimated to vary over a range from several hundred nanometers to several micrometers thick. These estimates were based on the assumption of uniform matrix distribution and a density estimate of $\sim$1 g/ml.

Absorbance spectra and absorptivities were determined using a Hewlett Packard photodiode-array spectrophotometer. Solution spectra were taken in methanol solution. The films were produced by spin-coating onto quartz plates and measured by simply placing the plate in the spectrometer with the sample oriented perpendicular to the beam path.

The acoustic transducer used was an Archer wide-range response replacement condenser microphone element (Radio Shack, No. 270-092B). The listed response was essentially flat over the frequency range from 20 Hz to approximately 16 kHz. The microphone was positioned $\sim$36 mm from the desorption site along the sample surface normal. For the QCM work, the oscillator consisted of a 6-MHz AT cut quartz crystal from Maxtek (Part No. 1032000) connected with an oscillator controller chip (Texas Instruments, No. 74LS321). The electrode configuration was a keyhole-type design and had an active area of approximately 31 mm^2. A photon counter in conjunction with an amplifier–discriminator (Ortec, Models 9315 and 9302, respectively) was used to determine the oscillation frequency. Because the electrode was not transparent to UV radiation, all QCM desorption was done in front-side geometry.

3. Results and discussion

3.1. Matrix characterization

Film morphology varied tremendously with sample preparation method, analyte, and matrix. In general, the ferulic acid solutions gave the most uniform films. In agreement with most of the literature reports, a thicker ring of sample formed at the edge of cast films. Films formed by spin-coating did not exhibit this edge effect and were nicely uniform. Although they were too thin to give much information under a microscope, macroscopically they were extremely even looking. One estimation of film uniformity was available from interference effects within the films. Reflected room light was limited to mostly a single color per film. Supposing that the interference is first order, this would suggest a thickness variation of no more than 10%.

An observable change in ferulic acid films occurred over time. The films, which were initially transparent, became opaque with the passage of time. This time period varied from 10 min to 1 h. It is possible that solvent is trapped in the matrix and evaporation is slow. The change in appearance was speeded when the plates were warmed. The caffeic acid samples were typically opaque immediately upon drying. The other matrices typically produced transparent films that did not become opaque. Anthranilic acid tended to coat the quartz surface quite unevenly.

Molar absorptivities for films and solutions at 337 nm were also determined for each matrix, as listed in Table 1. An absorbance plot for deposited ferulic acid

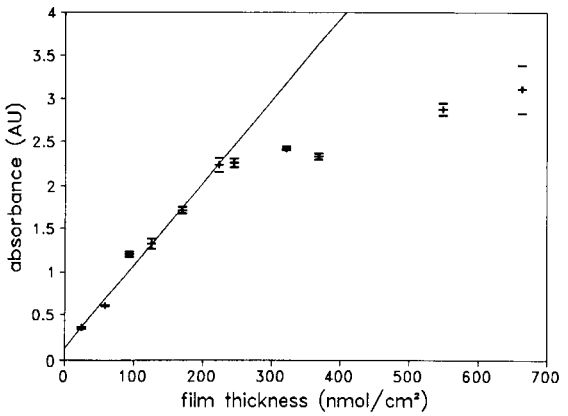

Fig. 2. Absorptivity determination for ferulic acid films.

is shown in Fig. 2. Absorbance was determined for each film thickness at five different positions on the film. The error bars indicate ± 1 S.D. give a sense of film uniformity. Absorbance values larger than 2.5 are subject to instrumental errors. Absorbance spectra for both solution and film samples of the five matrices investigated are displayed in Fig. 3. A trend common to all samples is that the absorbance maximum is shifted to higher wavelengths for the film. This greatly affects the efficiency of laser coupling at 337 nm. A long absorption tail exists in each case towards high wavelengths for the thin films. This is indicative of scattering due to the crystalline structure of the films.

3.2. *Quantification*

Frontside and rearside desorption gave distinctly different results. When the desorption laser irradiance was less than ~ 1 MW/cm^2, desorption was incomplete or absent regardless of geometry. At higher irradiances (i.e., > 1.5 MW/cm^2), rearside desorption was virtually complete with no observable film residue remaining. Frontside desorption removed considerably less sample. Depending on film thickness, 3–30 laser pulses were required for complete sample removal. For rearside desorption the cleaned sample area was found to be a function of laser pulse energy. This can be attributed to the threshold nature of the desorption process. The laser only interacts with the layers right next to the substrate. Since the films are of finite thickness, once the desorption threshold is exceeded, no additional material is removed from the sample surface with increased irradiance. However, as pulse energy increases, an increasing portion of the beam profile is above threshold fluence.

One way to determine the amount of material removed for each pulse is to measure the area cleaned by the laser beam. For the areal method the film thickness was determined by straightforward calculation from the amount deposited divided by the area covered. Of course this approach depends on the assumption of uniform sample distribution. The area cleaned was measured with a microscope fitted with a reticle. Quantitation of the amount desorbed was then taken to be the total amount deposited factored by the fraction of cleaned area to total area. Since frontside desorption did not clean the slides, areal quantitation was not possible for that geometry.

It is known that the volume expansion during vaporization produces an acoustic wave that is related to the amount of material vaporized [23–25]. A typical acoustic waveform is shown in Fig. 4. The arrival of the first positive deflection can be seen at 104 μs. The sample to microphone distance divided by the transit time yields a velocity of 346 m/s. This value is typical of the speed of sound in air and, ignoring any supersonic component [27], serves as an independent check on the sample-to-microphone distance. The negative deflection at 80 μs corresponds to transmission of sound through the solid support of the microphone.

Correlation of the acoustic signal to the amount of material removed in MALD was not straightforward. There are several causes. For frontside desorption, sample removal was generally incomplete. This made the areal estimation method inappropriate as an independent check. For rearside desorption, sample removal was virtually complete. However, no definite correlation of acoustic signal to the cleaned area was found. Acoustic signal arises as a result of compression of the surrounding atmosphere by the rapidly expanding plume. It is suggested that rearside desorption vaporizes only a portion of the sample closest to the quartz plate. The remainder of the sample is left with no physical attachment to the quartz, but driven away from the quartz surface by the expansion of the intervening material. Although sample removal was complete, it is likely that only the vaporized portion contributed to the acoustic signal. If this picture is true, it can be further hypothesized that the non-vaporized portion of the film could have a quenching effect on the expansion of the vapor and the resulting acoustic signal.

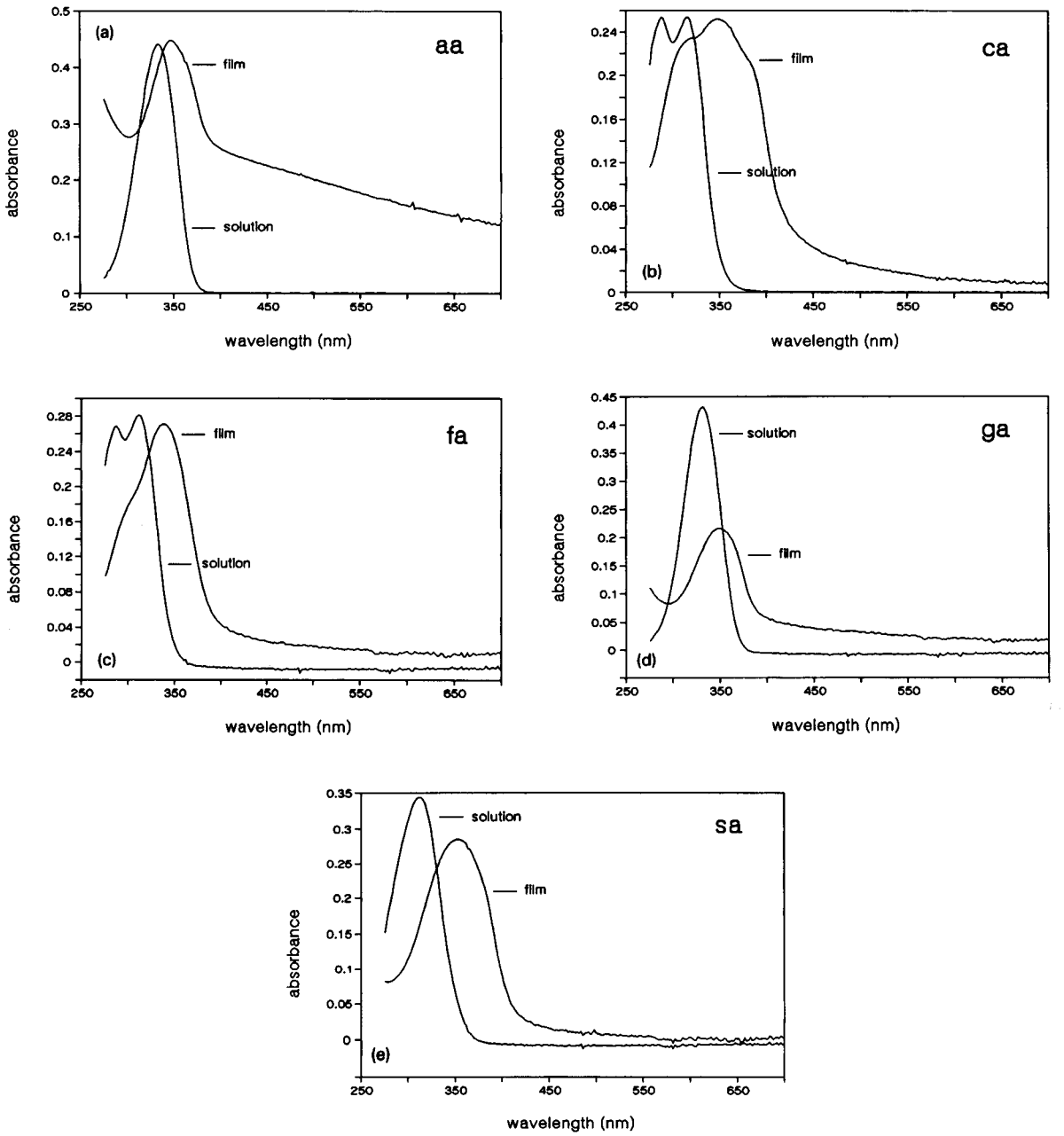

Fig. 3. Absorbance spectra of UV matrices: aa = antranilic acid (solution 160 μM, film 133 nmol/cm^2); ca = caffeic acid (solution 32 μM, film 20 nmol/cm^2); fa = ferulic acid (solution 32 μM, film 24 nmol/cm^2); ga = gentisic acid (solution 160 μM, film 24 nmol/cm^2); sa = sinapinic acid (solution 32 μM, film 27 nmol/cm^2).

In Fig. 5a, the frontside acoustic signal is plotted as a function of ferulic acid film thickness. Results from the rearside experiment are presented in Fig. 5b. At low film thicknesses, both plots show a linear dependence between the acoustic signal and film thickness. This is the regime where the acoustic signal is useful for quantification. In the frontside experiment the plot is basically flat above 120 nmol/cm^2. For a similar experiment for caffeic acid, the plot levels off at 220 nmol/cm^2. The rearside experiment shows a continued

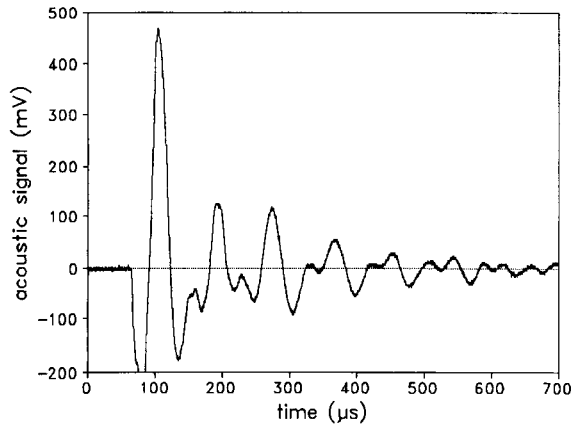

Fig. 4. Typical acoustic signal for frontside desorption of ferulic acid. Film thickness, 16 nmol/mm^2; microphone-to-sample distance, ~36 mm.

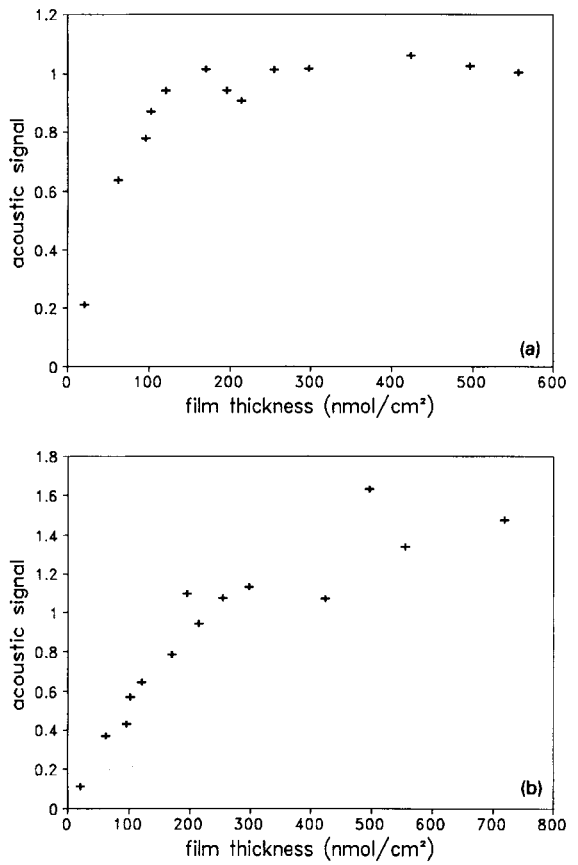

Fig. 5. Acoustic monitoring of (a) frontside desorption of ferulic acid films and (b) rearside desorption of ferulic acid films.

increase in the acoustic signal although the slope decreases somewhat for thicker films. This can be explained by the presence of a vapor plume in frontside desorption at early times, attenuating the laser beam for the thicker films and causing saturation in the amount of material vaporized. It should be pointed out that the acoustic signal is also a function of the energy delivered by the vaporization laser. The data in Fig. 5 have been normalized to compensate for variations in that energy. More will be said about this energy dependence later.

3.3. QCM studies

Fig. 6 shows the stepwise increase in QCM frequency with successive laser pulses. Laser pulses occur at approximately every tenth QCM reading. Each step increase in QCM frequency represents loss of film material from a desorption event. Given the relationship between frequency change and mass change, it is apparent that the greatest removal of material comes with the first several pulses. As pulses continue, sample removal is completed, the frequency change approaches zero, and the QCM frequency approaches a steady state. The overall frequency change in this example is 764 Hz. Assuming ideality of the Sauerbray equation, this corresponds to a mass removal of 1.5 μg. The areal method of quantitation indicates a mass removal of 2.2 μg. There is a discrepancy between these values, but when one considers all the assumptions involved in each calculation, the agreement is surprisingly good. The fact that the QCM value is the lower of the two suggests the difference may be attributed to the decreased sensitivity of the QCM for material deposited off-center.

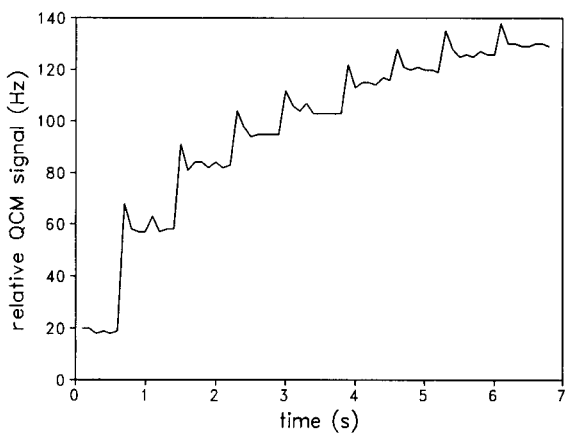

Fig. 6. QCM monitoring of frontside desorption of 557 nmol/cm^2 ferulic acid film. The laser pulses are separated by 1 s each.

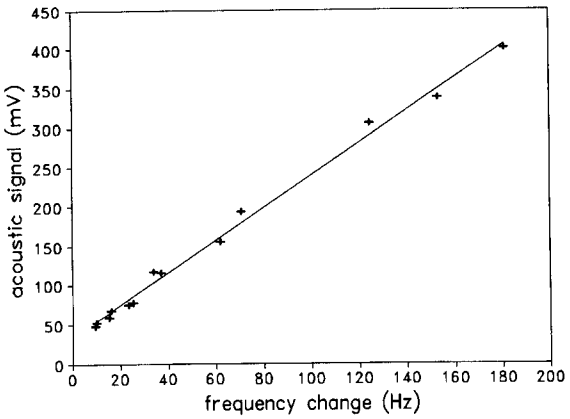

Fig. 7. Correlation between the acoustic signal and the QCM response for frontside desorption of 700 nmol/cm^2 ferulic acid film.

When the bare QCM was initially irradiated, a slight increase in oscillator frequency (~6 Hz) over about 60 laser pulses was observed. Recently, an ablation threshold of 0.6 J/cm^2 for gold from a QCM electrode has been demonstrated [21]. Based on typical fluences used in this work (~0.1 J/cm^2) it is unlikely that the observed frequency change is due to ablation of gold. In fact one run consisting of over 1800 laser pulses showed no change in QCM frequency for the last 1500 pulses. It can be postulated that the initial frequency change may be due to the removal of a surface oxide layer. Visual inspection of the QCM electrode after irradiation showed the desorption area to be noticeably shinier, supporting this hypothesis. In our desorption experiments, due to attenuation of the desorption pulse by the sample film, it was unlikely that gold removal could occur until a significant portion of the sample had been removed. Compared to the overall frequency change of over 700 Hz, this small contribution can reasonably be ignored.

Fig. 7 shows the acoustic signal plotted as a function of the change in QCM frequency. This plot is linear with a correlation coefficient of 0.997. The non-zero intercept is probably due to a background acoustic signal generated by the rapid thermal expansion of the bare gold electrode. Leung and Tam [27] have observed an acoustic signal at sub-threshold laser irradiances. They refer to this as a thermal piston signal. Heating effects are also the likely cause of spiking observed at the leading edge of each step in Fig. 6. Therefore each initial QCM reading after a laser pulse (corresponding to the spikes) is not useful for quantification. Although quantification of the amount of material vaporized for each MALD event by the acoustic signal could not be confirmed by an independent method, the linear relationship between the acoustic signal and both film thickness (Fig. 5) and QCM response (Fig. 7) suggest that the idea is reasonable.

3.4. Dependence on laser energy

As previously mentioned, there was a decided dependence of the acoustic signal upon nitrogen laser energy. In fact this relationship was found to be linear. The linear fits, as shown in Fig. 8, gave non-zero x-axis intercepts which tended to be remarkably independent of film thickness. Table 2 shows values determined for a range of ferulic acid film thicknesses. These intercepts, corresponding to a minimum pulse energy, represent a threshold value for a desorption event. Below this threshold there is insufficient energy to initiate desorption.

Rearside desorption gives about 10% higher thresholds than frontside. This difference is most evident for the thicker films. It was mentioned above that a qualitative explanation for complete sample removal in rearside geometry might be vaporization of sample closest to the quartz, which then drives the remaining non-vaporized sample away. If this explanation is correct, the energy required to remove the non-vaporized solid material can manifest itself as an increase in the observed threshold.

At low laser irradiances, the acoustic signal showed a tendency (Fig. 8) to deviate positively from the linear

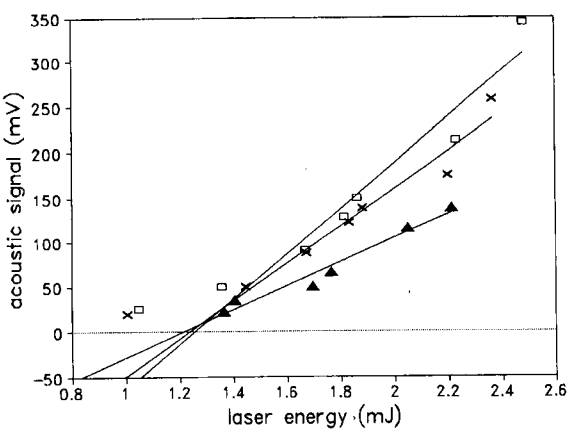

Fig. 8. Energy dependence of acoustic response for frontside desorption of three ferulic acid films; 424 nmol/cm^2 (□); 197 nmol/cm^2 (×); 63 nmol/cm^2 (▲).

Table 2
Desorption threshold of ferulic acid for various film thicknesses and for different desorption geometries (1 mJ = 1.67 MW/cm^2)

Film thickness (nmol/cm^2)	Frontside threshold (mJ)	Rearside threshold (mJ)
720	0.95	1.45
560	1.18	1.61
500	1.29	1.72
420	1.26	1.42
300	1.26	1.34
260	1.34	1.25
220	1.41	0.96
200	1.24	1.08
170	1.15	1.18
120	1.17	1.18
100	1.17	1.44
96	1.17	1.20
63	1.21	1.38
21	1.05	1.22
Mean	1.20	1.32
S.D.	0.11	0.20

fit. This is attributed to non-uniformity of the laser-beam profile. This unevenness creates hot spots where the local irradiance is significantly greater than the average irradiance. The result is that localized areas can exceed the vaporization threshold and give rise to an acoustic signal. With the omission of data points below the calculated threshold value, typical linear fits (Fig. 8) had correlation coefficients of 0.99.

A wide range of values for ion production thresholds in MALD have been reported [28], but the most recent work has tended to values in the range 1–10 W/cm^2. Specifically, the Hillenkamp group has reported a threshold for ion production using gentisic acid of 3×10^6 W/cm^2 [29]. Likewise, Ens et al. [2] have reported a threshold value of 2×10^6 W/cm^2 for sinapinic acid. These values agree remarkably well with the present measurements for acoustic thresholds. Threshold values for all matrices studied are presented in Table 1. If one ignores anthranilic acid, a correspondence between molar absorptivity (ε) and desorption threshold is seen. Specifically, larger molar absorptivity corresponds to a lower threshold. The effect of increasing ε would be to lower the irradiance required to reach some specific threshold energy value. The presence of an amine functional group exclusively on anthranilic acid could cause increased volatility and explain its unique behavior.

The conclusion is that once enough energy has been supplied to the irradiated sample to initiate desorption, ionization also takes place. Ens et al. [2] have reported ion yield scaling by a high power (fourth to sixth) of desorption laser irradiance. The fact that our acoustic signal is linear above threshold indicates that ion production may be occurring by mechanisms other than direct photoionization. It should be noted that our use of laser irradiance as the threshold parameter is somewhat arbitrary. Beavis [30] has suggested that laser fluence is, in fact, the critical parameter. Work at Uppsala [31] supports this view.

Acknowledgements

The Ames Laboratory is operated for the US Department of Energy by Iowa State University under Contract No. W-7405-Eng-82. This work was supported by the Director of Energy Research, Office of Basic Energy Sciences, Division of Chemical Sciences. Additional support was provided to TWH through a fellowship by the College of Liberal Arts and Sciences, Iowa State University.

References

[1] M. Karas, D. Bachmann, U. Bahr and F. Hillenkamp, Int. J. Mass Spectrom. Ion Proc., 78 (1987) 53.
[2] W. Ens, F. Mao, F. Mayer and K.G. Standing, Rapid Commun. Mass Spectrom., 5 (1991) 117.
[3] B.U.R. Sundqvist, Int. J. Mass Spectrom. Ion Proc., 118–119 (1992) 265.
[4] A. Vertes, R. Gijbels and R.D. Levine, Rapid Commun. Mass Spectrom., 4 (1990) 228.
[5] R.E. Johnson and B.U.R. Sundqvist, Rapid Commun. Mass Spectrom., 5 (1991) 574.
[6] A. Vertes, in K.G. Standing and W. Ens (Eds.), Methods and Mechanisms for Producing Ions from Large Molecules, Plenum Press, New York, 1991, p. 275.
[7] R.C. Beavis and B.T. Chait, in K.G. Standing and W. Ens (Eds.), Methods and Mechanisms for Producing Ions from Large Molecules, Plenum Press, New York, 1991, p. 227.
[8] F. Hillenkamp, M. Karas, R.C. Beavis and B.C. Chait, Anal. Chem., 63 (1991) 1193A.
[9] G. Talbo and P. Roepstorff, Rapid Commun. Mass Spectrom., 7 (1993) 201.
[10] S. Lewis, K.K. Korsmeyer and M.A. Correia, Rapid Commun. Mass Spectrom., 7 (1993) 16.
[11] B. Stahl, M. Steup, M. Karas and F. Hillenkamp, Anal. Chem., 63 (1991) 1463.

[12] K.J. Wu, A. Steding and C.H. Becker, Rapid Commun. Mass Spectrom., 7 (1993) 142.
[13] R.W. Nelson, R.M. Thomas and P. Williams, Rapid Commun. Mass Spectrom., 4 (1990) 348.
[14] M. Karas, U. Bahr, A. Ingendoh and F. Hillenkamp, Angew. Chem., 101 (1989) 805.
[15] R.S. Houk, in E.H. Piepmeier (Ed.), Analytical Applications of Lasers, Wiley, New York, 1986, p. 587.
[16] A. Vertes, L. Balazs and R. Gijbels, Rapid Commun. Mass Spectrom., 4 (1990) 263.
[17] R.S. Patel and M.Q. Brewster, J. Heat Transfer, 112 (1990) 170.
[18] E. Nordhoff, A. Ingendoh, R. Cramer, A. Overberg, B. Stahl, M. Karas, F. Hillenkamp and P.F. Crain, Rapid Commun. Mass Spectrom., 6 (1992) 771.
[19] K. Strupat, M. Karas and F. Hillenkamp, Int. J. Mass Spectrom. Ion Proc., 111 (1991) 89.
[20] G.Z. Sauerbrey, Z. Phys., 155 (1959) 206.
[21] J. Pérez and B.R. Weiner, Appl. Surf. Sci., 62 (1992) 281.
[22] A.C. Hillier and M.D. Ward, Anal. Chem., 64 (1992) 2539.
[23] G. Chen and E.S. Yeung, Anal. Chem., 60 (1988) 2258.
[24] H.-M. Pang and E.S. Yeung, Anal. Chem., 61 (1989) 2546.
[25] Y.-M. Lai and N.-H. Cheung, personal communication.
[26] T.W. Heise and E.S. Yeung, Anal. Chem., 64 (1992) 2175.
[27] W.P. Leung and A.C. Tam, Appl. Phys. Lett., 60 (1992) 23.
[28] R.C. Beavis, Org. Mass Spectrom., 27 (1992) 653.
[29] K. Strupat, M. Karas and F. Hillenkamp, Int. J. Mass Spectrom. Ion Proc., 111 (1991) 89.
[30] R.C. Beavis, Org. Mass Spectrom., 27 (1992) 864.
[31] P. Demirev, A. Westman, C.T. Reimann, P. Håkansson, D. Barofsky, B.U.R. Sundqvist, Y.D. Cheng, W. Seibt and K. Siegbahn, Rapid Commun. Mass Spectrom., 6 (1992) 187.

ELSEVIER

Analytica Chimica Acta 299 (1995) 387–391

ANALYTICA CHIMICA ACTA

New percutaneous absorptiometry by a laser photoacoustic method using an open-ended cell

Ryuichi Takamoto [a], Shinya Yamamoto [a], Ryujiro Namba [a], Masahiro Matsuoka [a], Tsuguo Sawada [b,*]

[a] *Safety and Analytical Research Center, Shiseido Company, Ltd., 1050 Nippa-cho, Kohoku-ku, Yokohama 223, Japan*
[b] *Department of Industrial Chemistry, Faculty of Engineering, The University of Tokyo, 7-3-1 Hongo, Bunkyo-ku, Tokyo 113, Japan*

Received 8 March 1994; revised manuscript received 3 May 1994

Abstract

An UV laser photoacoustic (PA) method with high sensitivity and accuracy using a novel open-ended cell was developed. It was constructed by processing the end of a light guide as the sample chamber of the PA cell and by attaching an acoustic pipe bent at an optimized right angle to one end. A series of in vitro and in vivo percutaneous absorptiometric studies was performed using an anti-inflammatory agent and an anti-itching agent. As a result, it was concluded that this PA method was applicable to percutaneous absorption.

Keywords: Photoacoustic spectrometry; Percutaneous absorptiometry; Lasers

1. Introduction

Evaluation of the percutaneous absorption of a substance is very important in the development of endemic liniments. Therefore, various methods of percutaneous absorptiometry have been studied [1–5], such as the diffusion cell method and radioisotopic methods. However, a method which is capable of reliably and easily measuring percutaneous absorption has not yet been found. In particular, it is too difficult to acquire a reliable in vivo method.

Several investigations have reported the photoacoustic (PA) method as an effective method [6–12]. The most remarkable point is the reliability of an open-ended PA cell. We have reported the development of percutaneous absorptiometry using the laser PA method and its usefulness in in vitro and in vivo measurements. This system was combined with a longitudinal diffusion cell used generally for in vitro percutaneous absorptiometry to substantiate its applicability to in vitro measurement [13]. It was actually applied to human in vivo percutaneous absorptiometry to show the possibility of this method [14]. By measuring the change in the PA signal with time, corresponding to the amount of drug remaining on the skin, we were able to evaluate the percutaneous absorption of subject drugs. In order to cover the wide range of compounds which can be tested by this method, we have developed a new UV laser PA method with high sensitivity and accuracy using a novel open-ended PA cell [15]. For the development

* Corresponding author.

SSDI 0003-2670(94)00466-8

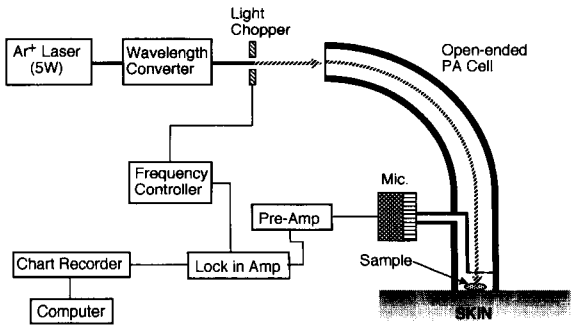

Fig. 1. Diagram of UV laser photoacoustic system using the open-ended cell.

of the PA cell (a) the influence of skin surface potential and environmental noise (< 100 Hz) and (b) the dead volume of the PA cell should be minimized and (c) the PA cell should be as small as possible for easy measurement.

A series of in vitro and in vivo percutaneous absorptiometric studies using the new open-ended PA cell were performed. The feasibility of a percutaneous absorptiometric technique utilizing this PA method is reported.

2. Experimental

Fig. 1 shows an in vivo percutaneous absorptiometric system using the open-ended PA cell combined with the light guide. UV radiation with a CW laser of 257 nm was used as the light source and was obtained by oscillating a multiple Ar^+ laser beam (Spectra Physics, Model 2020) at 5 W and using a BBO (β–BaB_2O_4) crystal wavelength converter (Ascal, UVA-4), which can be micro-adjusted optically. The UV laser beam was modulated at 2.2 kHz (the resonance frequency of the PA cell) by a light chopper (NF Co.). The output intensity of the light source was set to 3 mW by a light guide. The bundle-type guide (Asahi Glass, 1 m × 5 mm), which can transmit more than 85% of such UV radiation, was used to provide more measurement flexibility and to minimize the dead volume of the cell. The open-ended PA cell was constructed by using the end of the light guide as the sample chamber (stainless steel) and attaching an acoustic pipe (β-brass) bent at right angles inside the end of the light guide. A microphone (Primo, MP-10) was threaded to the acoustic pipe to control its length. The volume and width of the air layer in the sample chamber were 0.04 cm^3 and 0.2 cm, respectively. The total length of the acoustic pipe connecting the sample room and the microphone room was 8 cm. These values were found to produce a resonance at a frequency of several kHz that was hardly influenced by pulsation from the skin and environmental noise. This resonance frequency is based on the resonance theory calculated from the equation.

$$f = m(c/2L) \quad (1)$$

where f is the resonance frequency, m is the natural number, c is the speed of sound, and L is the total length of the acoustic pipe. Therefore, the frequency can be adjusted by changing the length of the acoustic pipe. Additionally, the acoustic pipe was bent at a right angle with sides 5 cm and 3 cm in length. The PA signal detected by the cell was analyzed using a lock-in amplifier (NF Co., 5610A), recorded using a chart recorder (Rika Denki Kogyo, NP-0393) and calculated using a computer (Nippon Denki, VX).

Next, in vitro percutaneous absorptiometry [13] was studied utilizing the open-ended PA cell as the longitudinal diffusion cell shown in Fig. 2. With this system it was feasible to measure simultaneously in real time. The decrease of the amount of drug applied to an excited skin by the PA method and the amount of drug penetrating the skin to the diffusion cell by absorbance. The UV laser beam for measur-

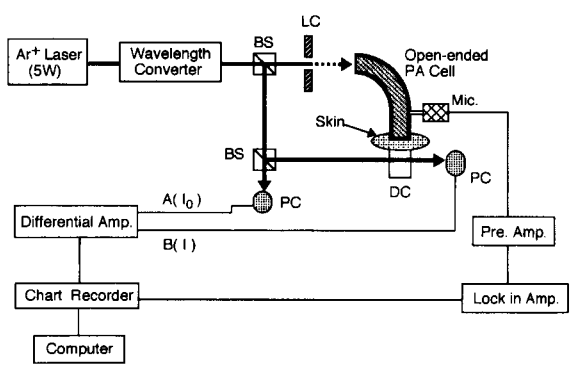

Fig. 2. Diagram of the in vitro percutaneous absorptiometry by simultaneous measurement of PA signal and absorbance. BS = beam splitter, LC = light chopper, PC = photocell, DC = diffusion cell.

ing the absorbance was further separated into two directions, one for the quartz longitudinal diffusion cell (Atock) capable of measuring absorbance and the other to the photocell (United Detector Technology, PIN-10DP) as the reference signal (I_0). The measured signal (I) and the reference signal (I_0) were introduced into a differential amplifier (NF P-61), and after calculation of the absorbance ($-\log I/I_0$) with a computer (Nippon Denki, PC9801-VX), the relation between PA signal and absorbance as a function of time was determined.

Indomethacin (IDM: $C_{19}H_{16}ClNO_4$, Wako, Reagent Class "for Biochemistry") as anti-inflammatory agent and zinc picolinate complex as anti-itching agent (PZ) that absorb UV radiation at 257 nm were used as model samples. The IDM ointment and the PZ solution were prepared using poly(ethylene glycol) (PEG) and water–glycerine (60:40), respectively. In addition, a hairless mouse and a guinea pig were used as the subject animals.

3. Results and discussion

3.1. Sensitivity and reproducibility of a novel open-ended PA cell combined with a light guide

The detection accuracy of PA measurement of IDM ointment was investigated using an UV laser PA system. Excellent sensitivity and reproducibility were obtained over 10 repeated measurements of IDM (4 μg per 5 mm diam.); the signal-to-noise ratio (S/N) was 46 and the coefficient of variation (C.V.) was not more than 3%. Excellent linearity was obtained for 2–120 μg of IDM with a correlation coefficient of not less than 0.99.

3.2. Application to the in vitro measurement of percutaneous absorption

A series of in vitro percutaneous absorptiometric measurements was performed on the skin of a hairless mouse. Within a 5 mm diameter circle on the skin of the hairless mouse (defatted), 6 mg of 1% IDM ointment was applied. Employing physiological saline solution as the diffusion cell solvent, the absorbance and PA signal were measured simultaneously. The results are shown in Fig. 3. An increase

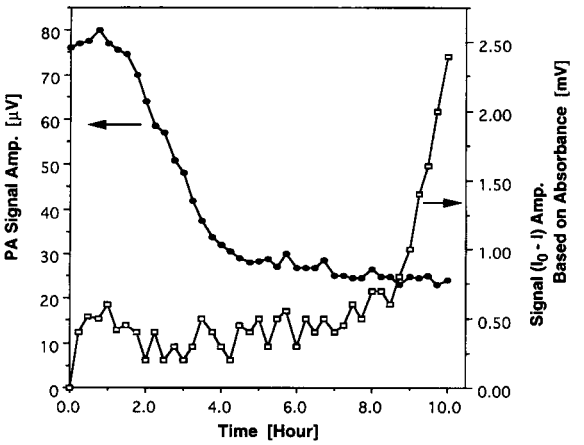

Fig. 3. In vitro percutaneous absorptiometry using the skin of a hairless mouse.

in absorbance and decrease in PA signal were also observed in the skin system of the hairless mouse, resembling a living body. Fluctuations in the absorbance are considered to be caused by floating matter and water-soluble matter deriving from the skin. The amount of IDM passing through the skin started to increase proportionally to time after a 7 h lag, and it was found that 1.1% of the initially applied IDM had been transmitted through the skin after 10 h. The rather longer lag time observed here, compared with the degree of decrease in PA signal, is because IDM was trapped in the skin. Another reason is the temperature [16], which in this experiment was ambient (20°C), whereas the in vitro percutaneous absorptiometry experiments were undergone at 37°C, to mimic body temperature.

Consequently, it can be expected that this in vitro percutaneous absorptiometric system, whereby the PA signal and the absorbance is measured simultaneously, will be capable of analyzing both the drug-releasing process and its transmission process through the skin, in real time, in a system resembling actual clinical conditions.

3.3. Measurement of in vivo percutaneous absorption

In vivo percutaneous absorptiometry was attempted using 1% IDM ointment as anti-inflammatory agent applied to a hairless mouse. Fig. 4 shows

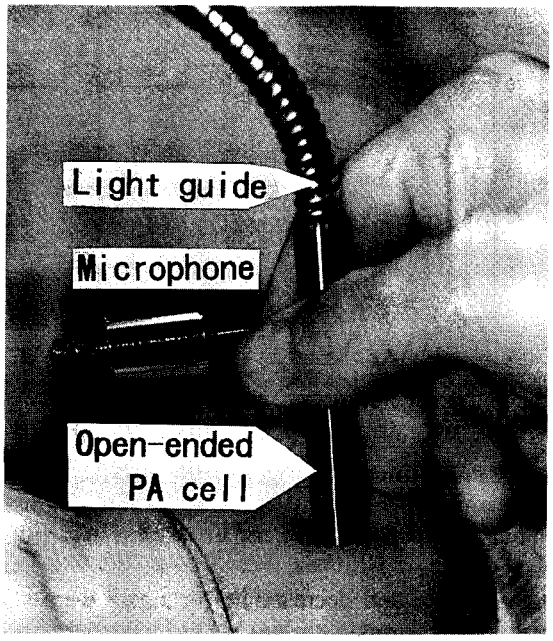

Fig. 4. Photograph showing the measurement of in vivo percutaneous absorption by the open-ended PA cell.

a photograph of the in vivo measurement. The PA cell is gently put on the skin with the applied sample. These measurements were made every 5 min to avoid accelerated percutaneous absorption as a result of heating by the UV laser beam. The measurement time of about 15 s and could be decreased to this time by the improved S/N value. This was very effective in minimizing damage to in vivo skin as much as possible. The obtained S/N value was about 40. Fig. 5 shows the mean results of five repeat measurements. When the PA signals obtained by applying only the PEG vehicle were compared with those of the 1% IDM ointment measured under the same conditions, the former was nearly constant with time, while the latter indicated a 5% decrease in the initial PA signal after 60 min. It was confirmed that the decrease in the PA signal is not due to chemical change in destruction of the IDM by irradiation. The change in the PA signal is thought to reflect the percutaneous absorption of IDM.

We then tried to obtain the diffusion coefficient of IDM across the skin of a hairless mouse in vivo, by observing the time constant of the decrease in the PA signal [9]. Since the decrease in the concentration of

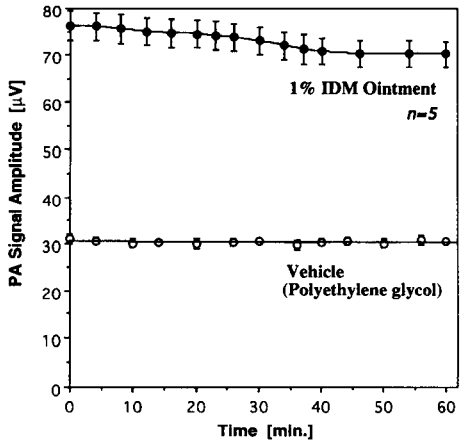

Fig. 5. PA signal versus time when measuring hairless mouse in vivo percutaneous absorption.

the IDM was essentially exponential, the time constant was obtained by plotting logarithmic PA signals with time. In addition, from the theory of diffusion of substances across membranes of finite width, it was found that the time constant, τ, of such processes is expressed as

$$\tau = 4L^2/\pi^2 D \quad (2)$$

where L is the width of the membrane and D is the diffusion coefficient of the substance in a given medium. This principle was applied to the results in Fig 5. A time constant of 607 min was obtained with

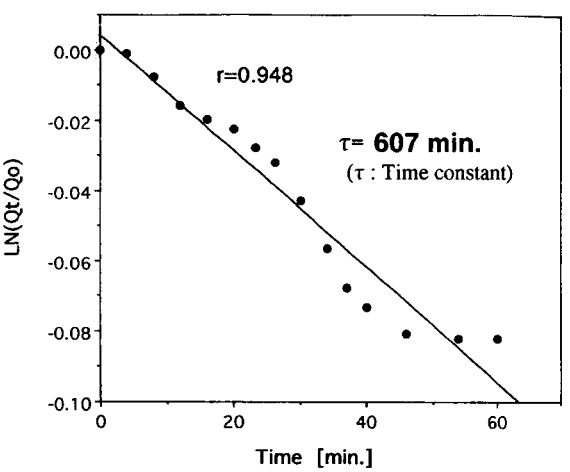

Fig. 6. Determination of the diffusion coefficient of IDM across the skin of a hairless mouse in vivo.

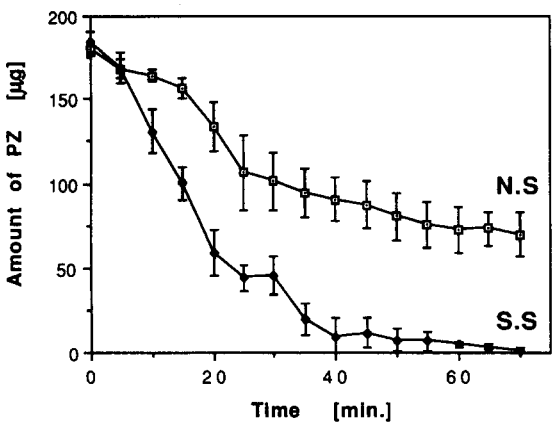

Fig. 7. Comparison of the in vivo percutaneous absorption of a normal skin (N.S.) with that of a stripped skin (S.S.).

a linear correlation coefficient of 0.948 (shown in Fig. 6); the diffusion coefficient was calculated to be 6.7×10^{-6} cm^2 min^{-1} for a skin thickness of 0.1 cm. This value is of the same order (3.5×10^{-6} cm^2 min^{-1}) as that obtained by the conventional in vitro method using a longitudinal diffusion cell. These results confirmed the effectiveness of this newly-developed in vivo percutaneous absorptiometric technique, which is simpler than other methods such as the use of radioisotopes.

Next, an in vivo percutaneous absorption experiment using the 0.8% PZ solution as anti-itching agent applied to both the normal skin of a guinea pig and the skin stripped horny layer by a tape. In general, the horny layer is the most important barrier for percutaneous absorption of an endemic liniment. As shown in Fig. 7, the anticipated differences in percutaneous absorption of PZ between normal skin and stripped skin were obtained by this novel technique.

4. Conclusions

A novel percutaneous absorptiometric system using an open-ended PA cell combined with a light guide was developed. This system is capable of measuring the decrease of the amount of a drug over the skin in vivo at any site with great ease, high sensitivity and accuracy. Based upon the results shown above, it was concluded that the newly developed UV laser PA method using a novel open-ended cell was applicable to percutaneous absorption.

Application to in vivo human skin must be safe, the total UV energy received at the skin was less than 40 mJ, and no ill effects were observed on the skin of hairless mice. Applying this energy to human skin in vivo seems to be safe but final confirmation is required. Experiments to confirm safety for human skin are under way.

References

[1] R.L. Bronaugh and R.F. Stewart, J. Pharm. Sci., 75 (1986) 1094.
[2] D. Southwell, B.W. Barry and R. Woodford, Int. J. Pharm., 18 (1984) 299.
[3] K. Tojo, M.M. Ghannam, Y. Sun and Y.W. Chien, J. Controlled Release, 1 (1985) 197.
[4] C.L. Gummer, R.S. Hinz and H.I. Maibach, Int. J. Pharm., 40 (1987) 101.
[5] R.H. Guy, E.M. Carlstrom, D.A.W. Bucks, R.S. Hinz and H.I. Maibach, J. Pharm. Sci, 75 (1986) 968.
[6] A. Rosencwaig, Clin. Chem., 28 (1982) 1878.
[7] A. Rosencwaig and E. Pines, Biochim. Biophys. Acta, 493 (1977) 10.
[8] S.D. Campbell, S.S. Yee and M.A. Afromowitz, J. Bioeng., 1 (1977) 185.
[9] S.D. Campbell, S.S. Yee and M.A. Afromowitz, IEEE Trans. Biomed. Eng., BME-26(4) (1979) 220.
[10] P. Poulet and J. Chambron, J. Photoacoustic, 1 (1983) 329.
[11] K. Kolmel, B. Sennhenn and K. Giese, J. Soc. Cosmet. Chem., 37 (1986) 375.
[12] K. Giese, A. Nicolaus, B. Sennhenn and K. Kolmel, Can. J. Phys., 64 (1986) 1139.
[13] R. Takamoto, R. Namba, O. Nakata and T. Sawada, Anal. Chem., 62 (1990) 674.
[14] R. Takamoto, R. Namba, M. Matsuoka and T. Sawada, Anal. Chem., 64 (1992) 2661.
[15] R. Takamoto, S. Yamamoto, R. Namba, T. Takamatsu, M. Matsuoka and T. Sawada, Anal. Chem., 66 (1994) 2267.
[16] W.C. Fritsch and R.B. Stoughton, J. Invest. Dermatol. 41 (1963) 307.

ELSEVIER

Analytica Chimica Acta 299 (1995) 393–399

ANALYTICA CHIMICA ACTA

Atomic emission spectrometric analysis of steel and glass using a TEA CO_2 laser-induced shock wave plasma

Kiichiro Kagawa [a,*], Hiroyuki Hattori [a], Masuo Ishikane [a], Masahiro Ueda [a], Hendrik Kurniawan [b]

[a] *Faculty of Education, Fukui University, Fukui 910, Japan*

[b] *Spectroscopy Laboratory, Graduate Faculty for Opto-electronic and Laser Application, University of Indonesia, 4 Salemba Raya, Jakarta 10430, Indonesia*

Received 5 January 1994; revised manuscript received 9 February 1994

Abstract

The shock wave plasma induced by the bombardment of laser light coming from a commercial TEA CO_2 laser has been used for the direct elemental analysis of solid samples. By using standard low-alloy steel samples, it is demonstrated that there is a linear relationship between the Cr content and the emission intensity, using an internal standard method. A background equivalent concentration for the Mg 383.8 nm emission line is found to be as low as about 0.005% in glass samples.

Keywords: Laser ablation analysis; Shock wave plasma; TEA-CO_2 laser

1. Introduction

Development of new techniques for direct analysis of solid samples without pretreatment has been ardently demanded in many fields, scientific and industrial. General methods for the direct analysis of solid samples are the spark-discharge method, the Grimm-discharge method and x-ray fluorescence spectrometry. The disadvantage of the spark-discharge and Grimm-discharge methods is the limitation of the analysis only to metal samples. X-ray fluorescence spectrometry cannot be applied to light elements such as Be and B. Another method for the direct analysis of solid samples is laser ablation atomic emission spectrometric analysis (LAESA) [1–3]. Advantages of LAESA are that both metallic and non-metallic samples are analyzed and the light elements can also be detected.

In normal LAESA, high power solid state lasers, such as ruby and Nd, are used and laser light is focused under atmospheric pressure. In the case of Q-switched laser bombardment, plasma generation takes place with a strong continuum emission spectrum due to the high density plasma. This makes it difficult to obtain highly sensitive analysis. Furthermore, strong self-absorption occurs because the heated plasma is surrounded by a sheath of cool atoms. These problems have been overcome to some extent by separating the evaporation and excitation stage. Commercial equipment is available in which the sample target is vaporized by a laser beam from a normal oscillation laser and the excitation is made by a spark discharge in terms of auxiliary electrodes placed above the surface of the target. However, there are still some difficulties in precision and sensitivity. Therefore, LAESA has mainly been used for qualitative analysis of solid samples.

* Corresponding author.

SSDI 0003-2670(94)00316-5

Another possible method for separating the evaporation and excitation stages in LAESA is to employ the laser-induced shock wave. Basov et al. [4] proved for the first time the generation of laser-induced shock wave plasma with the use of a high-power laser pulse (6 J, 15 ns) under lower ambient gas pressures (2 Torr). Hughes [5] reviewed these experiments concerning the laser-induced shock wave plasma. However, all these experiments were made only from the view point of high-temperature hydrodynamics, and no report has been made by other researchers on the application of the laser-induced shock wave plasma to spectrometric analysis.

In a series of studies, we have developed another LAESA method [6–15]. In our method, a laser beam with short pulse duration, such as N_2, excimer and TEA CO_2 laser beams, is employed and the pressure of the surrounding gas must be decreased to around 1 Torr. The laser induced plasma consists of two distinct regions. The first is a small area of plasma (called the primary plasma), which gives off intense continuous emission spectra for a short time just above the surface of the target. The other area (secondary plasma) expands with time around the primary plasma, emitting sharp atomic line spectra with low background signals. The shape of the secondary plasma is hemispherical when observed by the naked eye. The radius of the secondary plasma depends on the pulse energy of the laser and also on the pressure of the surrounding gas. The secondary plasma has characteristics quite suitable for emission spectrometric analysis. Especially, the low background emission intensity and the linear relationship between the emission line intensity and the content of the element are most advantageous. On the basis of the experiments using time-resolved spectroscopic study on the plasma induced by a TEA CO_2 laser and XeCl excimer laser, we have proposed a shock wave model to explain the mechanism in forming the secondary plasma, although the pulse energy of the laser is considerably lower than that employed in the experiments of Basov et al. [4]. We have called this analytical method laser-induced shock wave plasma spectrometry (LISPS).

In this paper, we report briefly on the practical application of LISPS using a TEA CO_2 laser as the exciting source. Gibson et al. [16] attempted for the first time the application of a TEA CO_2 laser to laser ablation emission spectrometric analysis. They determined Si in Ge samples under reduced pressure of the surrounding gas. However, it seems that their plasma is different in character from our shock wave plasma. The luminous region of their plasma was very small and the shape is not hemispherical. This is probably because in their case the pulse duration was rather long and the pulse energy was lower compared to our case.

The advantage of applying the TEA CO_2 laser as the source of the shock wave plasma are as follows:

(1) The TEA CO_2 laser is widely used industrially for marking processes and is commercially available. The laser operates with high power and with good shot-to-shot output stability. The running costs are very low.

(2) Since the photomultiplier tube is not sensitive at the wavelength of the TEA CO_2 laser light, there is no to care about stray laser light coming into the monochromator.

(3) Since the TEA CO_2 laser light has high absorbance on glass samples or rock samples, plasma generation takes place effectively with a low threshold pulse energy of the laser light.

2. Experimental

Fig. 1 shows the schematic representation of the experimental set-up used in this study. The TEA CO_2 laser used in this work is a Shibuya SQ-2000, which was developed and constructed by the Shibuya com-

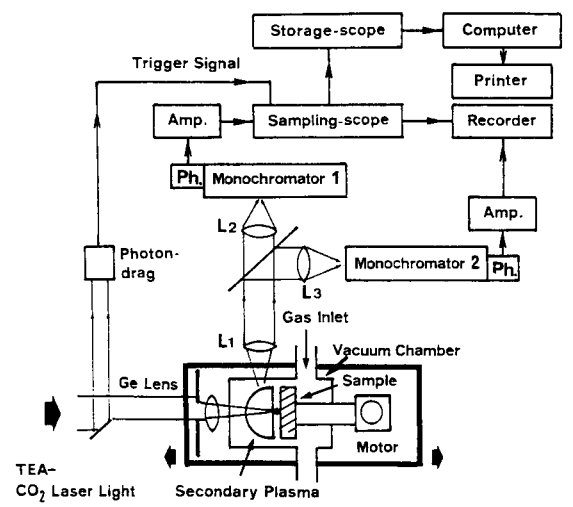

Fig. 1. Schematic representation of the experimental set-up used for emission spectrometric analysis using a TEA CO_2 laser-induced shock wave plasma.

pany for laser marking. The laser was operated at 5 Hz with characteristics of 3 J pulse energy, 100 ns pulse width in half and 30×30 mm beam area. The laser beam was transmitted through a ZnSe window and focused on the sample surface with a Ge lens of 100 mm focal length. The focused energy of the laser pulse was changed with variable apertures placed in front of the Ge lens. The pulse energy of 700 mJ was used for steel samples and 300 mJ for glass samples. The shot-to-shot fluctuation of the laser pulses was about 3%. The sample was set in a vacuum-tight metal chamber in which the pressure was regulated at 200 Pa with air.

To provide an internal standard method for the emission spectrometric analysis, two monochromators were used. The image of the secondary plasma was formed on the entrance slit of two monochromators (M1, M2) with the aid of quartz lenses (L1, L2, L3), with a focal length of 150 mm, and a beam splitter. The radiation of the secondary plasma 7 mm above the surface of the sample was sent into the entrance slits of the monochromators. The position of the entrance slits was set carefully so that the same region of the secondary plasma could be observed by the two monochromators. The adjustment was guaranteed by observing the linear correlation between the two signals, which were measured with different photomultiplier tubes attached to the two monochromators, on one emission line of the host element of the sample. The slit width of the monochromator M1 (Jobin Yvon HRS-2) was usually set at 30 μm, and that of M2 (Nikon P-250) was set at 25 μm. The slit height of both monochromators was set at 15 mm. In order to adjust the intensity level of the emission lines to be measured, a filter of known transmittance was placed in front of the monochromators as needed.

The intensity of the atomic emission lines was measured by means of a time-integrated method. For this purpose, a high resistance of 50 kΩ was connected to a photomultiplier tube (Hamamatsu R331) which was attached to the monochromator M1. The electrical signal from the photomultiplier tube was sent into a sampling oscilloscope (Iwatsu, SAS 601-B), which has a similar function to a boxcar integrator. The trigger signal of the sampling oscilloscope was obtained from a part of the laser light using a photon drag detector (Instruments, 7410). The time axis of the sampling oscilloscope was fixed at 10 μs at which the signal reaches maximum intensity. The output signal of the sampling oscilloscope was fed into a two-pen chart recorder or into a computer after once stored in a digital storage scope (Kikusui, DSS 6522). The use of the sampling oscilloscope is very effective for improving the signal-to-noise (S/N) ratio in the measurement of the intensity of atomic emission lines because of its gate function. The output from the photomultiplier tube (Hamamatsu, R1104) attached to M2, which was used for monitoring the emission line intensity of the host element in the sample, was sent directly to the two-pen chart recorder after passing through a time-integrated circuit.

The standard samples used for quantitative analysis were of low-alloy steel (JSS 150, Iron and Steel Institute of Japan).

3. Results and discussion

3.1. Application to steel samples

We have already reported that by the use of the LISPS method emission spectrometric analysis can successfully be made on steel samples using a N_2 laser (6 mJ) [8] or XeCl excimer laser (50 mJ) [15]. In those experiments the samples were rotated at ca. 1 rpm under repeated bombardments of the laser pulses (5 Hz) to produce a groove with a diameter of ca. 1 cm, which made the shape and the emission intensity of the secondary plasma almost constant for about 1 h. However, in the case of the TEA CO_2 laser, the same technique cannot be employed because the secondary plasma fluctuates in size and in emission intensity. This is probably due to lack of power density of TEA CO_2 laser light on the surface of the steel samples. The spot size of the focused beam of the TEA CO_2 laser is ca. 0.5 mm in diameter and the estimated laser power density is 3.6×10^9 W/cm^2; in contrast, the diameter is <100 μm for the N_2 laser and the laser power density is about 10^{11} W/cm^2. In order to overcome this fluctuation problem, laser bombardment was performed with the sample held in a fixed position, without rotating. By this method the fluctuation of the secondary plasma can be decreased remarkably.

Fig. 2 shows the time-course of the intensity of the Cr 425.4 nm and Fe 406.4 nm emission lines, taken from one of the standard samples of low alloy steel containing 0.5% Cr in weight. The wavelength of mo-

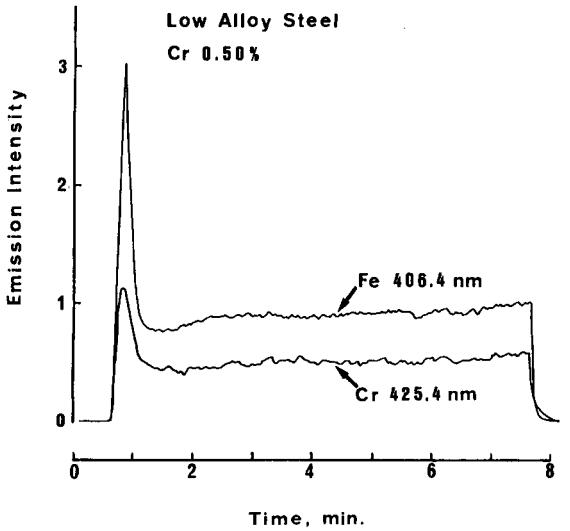

Fig. 2. Time course of the emission intensities of the Cr 425.4 nm and Fe 406.4 nm emission lines. Irradiation of laser light was made with the sample in a fixed position. The low-alloy standard steel sample contained 0.5 wt.% Cr.

nochromator 1 was fixed at 425.4 nm, and 406.4 nm for monochromator 2. The emission intensity reaches a maximum, after which it drastically decreases and finally is stabilized within about 1 min. At the beginning of the irradiation, the secondary plasma is about 2.5 cm in radius, which finally is decreased to ca. 1.5 cm. This phenomenon closely depends on the form and depth of the crater that is produced by the repeated bombardment by the laser. For convenience, in this paper the point at which emission intensity has the maximum value is called A and B stands for the plateau region.

It was observed that the intensity of the Cr emission line at A varies from experiment to experiment to some extent. The relative standard deviation (R.S.D.) of the intensity of the emission lines was obtained at A. As a result, the R.S.D. for Cr 425.4 nm was 9.8%, while that of the emission intensities of Cr 425.4 nm divided by the intensity of the Fe 406.4 nm emission line was 3.6%. Therefore, it can be said that quantitative analysis is possible at A provided that the internal standard method is used. It should be noted that this ratio is almost constant in region B. This implies that a constitution change does not take place in this sample during the successive bombardments on the same position of the sample. Therefore, region B can also be used for quantitative analysis.

In order to make calibration graphs from the results of the standard steel samples, the following preparation was made. A small block with dimensions of ca. $7 \times 5 \times 3$ mm was cut out from each of six samples. The six pieces were arranged around the center of the disk. The disk was mounted in the chamber. Using the same method employed in the experiment in Fig. 2, the relative intensity of the Cr 425.4 nm line compared with that of the Fe 406.4 nm line was obtained in the two regions (A and B in Fig. 2) by changing the samples. Measurements were repeated three times on each sample by changing the position. In region B, the emission intensity was read out at five different randomly chosen points.

Fig. 3 shows the resultant analytical curves for Cr. Plot A was obtained at the peak signal and plot B in the plateau region. It should be noted that the plot is linear in both cases. Such a linear relationship was already observed in the TEA CO_2 laser-induced shock wave plasma in food samples on the emission intensity of Ca 422.67 nm [17]. In contrast, there is no linear relation-

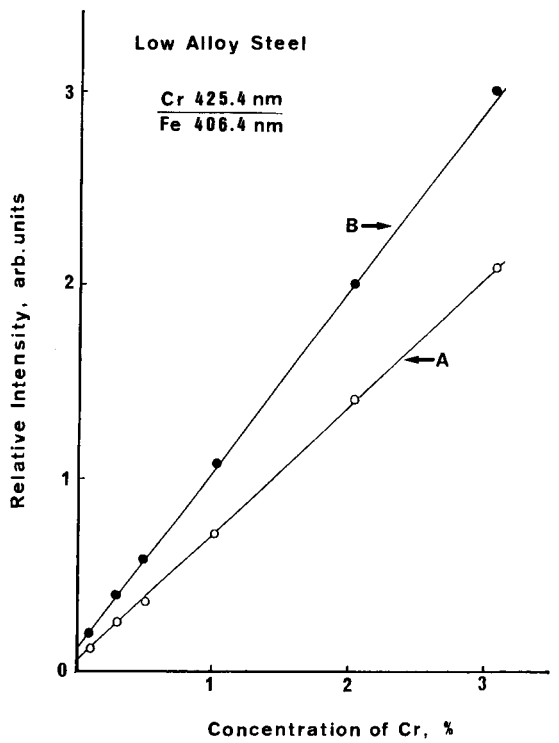

Fig. 3. Plot of the relative intensity of the Cr 425.4 nm line to that of the Fe 406.4 nm line against the Cr content of low-alloy standard steel samples. Curve A was obtained from the peak intensity and B from the plateau region.

ship for conventional LAESA, owing to the self-absorption taking place as resonance transitions in Cr atoms [18]. In the present case self-absorption is negligible. This probably arises because the secondary plasma has a thin shell structure seemingly like the inductively coupled plasma (ICP). This shell structure has already been proved in our previous experiments using a time-resolved spectroscopic technique [10,11,15]. As shown in Fig. 3, the slopes of the lines are different, probably because the temperature of the secondary plasma is different. The excitation energy of the Cr 425.4 nm line is 2.9 eV and that of the Fe 406.4 nm line is 4.6 eV. Different plasma temperature will give different intensity ratios.

From the intercepts of the lines on the ordinate in Fig. 3, the background equivalent concentration (BEC) was estimated to be ca. 0.06%. This value is high, but the BEC can be reduced by a factor of 10 or more by means of setting the entrance slit of the monochromator 12 mm from the sample surface. The BEC in the TEA CO_2 laser-induced shock wave plasma is higher than that for excimer laser-induced shock wave plasma. We already proved in the experiment using XeCl excimer laser that the BEC of the Cr 425.4 nm is as low as 0.0012% in the same low-alloy steel sample [15].

The calibration graph for Ni in the standard sample of the low-alloy steel is linear up to at least 4% Ni. The Ni emission intensity was less stable for Cr. This problem was solved by the use of helium (3000 Pa) as the surrounding gas; the emission intensity was read in the plateau region.

Measurements were also made on standard samples of high-speed steels. In contrast to the low-alloy steels, some problems were observed. In particular, it is surprising that emission lines due to W atoms could not be detected in spite of the fact that the sample contained ca. 10% of tungsten, and the emission lines for Fe are very strong; only in a limited region near the primary plasma could the emission of W be observed. In contrast, even for LISPS using a N_2 laser (pulse energy of 6 mJ) a good calibration for the W 400.9 nm emission line was obtained for high-speed steel samples [8]. It seems likely that the differences arise because in high-speed steel samples selective vaporization takes place because the boiling point of high-speed steels is higher than that of low-alloy steels. It is assumed that the vaporization of W atoms is delayed compared to the Fe atoms. As proposed in previous papers, a secondary plasma is produced through the adiabatic compression due to the atoms gushing from the primary plasma at supersonic speed [12,14,15]. Therefore, atoms are excited in the limited, thin-shell regions just behind the shock waves. If W atoms are delayed by the selective vaporization, the atoms cannot reach the excitation region and emission does not take place. However, such selective vaporization becomes negligible when the pulse duration is sufficiently short and the power density on the surface of the sample is sufficiently high. This is the case for the N_2 and XeCl excimer laser.

3.2. Application to glass samples

The LISPS method using a TEA CO_2 laser is especially suitable for glass samples. One advantage is the low threshold energy of plasma production. A very stable secondary plasma was produced under the successive bombardment of the laser light even when the sample was rotated. Another advantage of applying the TEA CO_2 laser is that a glass sample never emits fluorescence during irradiation. In contrast, for UV lasers such as the N_2 and XeCl excimer lasers, a glass sample fluoresces, thus raising the background level in the spectral measurement.

Fig. 4a shows the qualitative spectral profile obtained on the glass sample containing about a few percent of boron. In order to obtain this spectrum, the wavelength of the monochromator was scanned at 15 nm/min in the wavelength range from 245 to 258 nm and the signal from the sampling oscilloscope was fed into a digital storage oscilloscope (sweep time of 5 s/div). One spectrum was taken in 50 s. The measurements were repeated thrice and the signals were averaged in the computer. The sample was rotated at 1 rpm during the laser irradiation. The pulse energy of the laser was fixed at 300 mJ. Fig. 4b shows the result obtained from ordinary transparent glass containing no boron. Comparing these two spectra, it is seen that boron can easily be detected. This method has considerable promise for the rapid quantitative analysis of such light elements.

Fig. 4c shows how the emission intensity of the secondary plasma is stable for a glass sample. In this case the wavelength of the monochromator was fixed at 251.9 nm, one of the strong emission lines of Si. It should be noted that this curve is almost constant with little signal fluctuation, though it was obtained directly

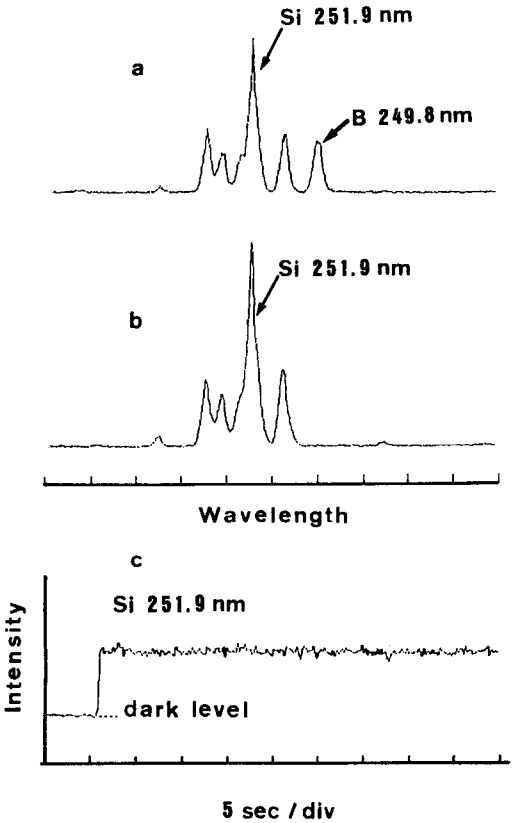

Fig. 4. Emission spectra obtained on the glass sample. (a) Glass containing a few percent of boron, (b) glass containing no boron. (c) Time variation of the emission intensity of the Si 251.9 nm line obtained in glass samples. Samples were rotated at 1 rpm under repeated irradiation of the TEA CO_2 laser with 5 Hz.

from the output of the sampling oscilloscope without passing through any smoothing circuit. This good stability of emission intensity endorses the possibility of high precision analysis.

In order to estimate the attainable detection limit due to this LISPS method, a glass sample containing 3% Mg was used. By comparing the emission intensity of the Mg 383.8 nm line with the background emission intensity taken near the tail of the emission line, the BEC was estimated to be about 0.005%. This value may be decreased in the near future.

In the LISPS method, the laser pulse energy and the height of the observation position above the surface of the sample are key factors for realizing high sensitivity analysis. As described in a previous paper, the primary plasma is the source of the shock wave [12]. In order to produce the primary plasma, the laser power density must be higher than about 10^9 W/cm^2. On the other hand, the laser pulse energy closely relates to the total amount of gushed atoms from the sample and determines their total kinetic energy. The kinetic energies of these atoms are mainly consumed in the initial explosion energy for producing the blast wave, the shock wave induced by a point explosion.

Sedov [19] derived, for a blast wave, a theoretical relationship between the propagation time, t, and the distance of the front from the position of the source of explosion, r, as follows:

$$r = (E_o/\alpha\rho)^{1/5} t^{2/5} \quad (1)$$

where E_0 is the initial explosion energy, ρ is the density of the surrounding gas, and α is a constant. From this equation the following equation can easily be derived.

$$v = (2/5)(E_0/\alpha\rho)^{1/2} r^{-3/2} \quad (2)$$

where v is the velocity of the shock front.

On the other hand, the temperature just behind the shock front, T, can be expressed as follows [20,21].

$$T/T_0 = [2\tau M^2/(\tau+1) - (\tau-1)/(\tau+1)][(\tau-1)/(\tau+1) + 2/(\tau+1)M^2] \quad (3)$$

where T_0 is the room temperature, τ is the ratio of the specific heat of the gas and M is the Mach number of the shock wave.

These equations are useful in order to understand qualitatively the characteristics of the plasma. From these equations, it is seen that the temperature just behind the shock front increases with E_0. This was proved in our experiment using Zn as the target. Thus, with increasing the energy of the laser pulse the speed of the luminous front of the plasma increases and plasma temperature also increases. When the plasma temperature is as high as 10,000 K, the background emission intensities become high. Therefore, high power laser pulses do not always bring high sensitivity analysis, although the total amount of gushed atoms become large. For spectrometric analysis, it is essential to enhance the ratio of the analytical emission line to that of the background. For this reason, suitable pulse energy of the laser light should be employed. At this stage, a laser pulse of 300 mJ was used for glass samples to obtain a sufficiently intense analytical emission line. In this case, the amount of sample needed to perform sufficient analyses is about 1 mg. If we employ an

improved detection system such as optical multi-channel analysis (OMA) or a polychromator, however, the pulse energy can be decreased and the sensitivity of the analysis will be improved. Also, in such conditions the minimum sample needed will be decreased to ca. 100 ng.

Eqs. 2 and 3 can also explain the experimental fact that the background emission intensity decreases with the distance from the surface of the sample because the intensity of the continuum emission of the plasma decreases with decreasing temperature. Taking the spatial distribution of the emission intensity of the analytical line and that of background spectrum into account, the best position for the observation area must be chosen so that the ratio of the analytical emission line to that of the background emission has the maximum value.

4. Conclusions

It has been proved that a commercial TEA CO_2 laser, which is usually used for laser marking, can be employed as the excitation source for a laser-induced shock wave plasma, with limited application. A good analytical calibration graph was obtained for low-alloy steel standard samples. However, for high-speed steel samples selective vaporization takes place, which makes it impossible to determine tungsten, mainly due to lack of energy density of the focusing laser light. Therefore, the development of a new TEA CO_2 laser is proposed that meets the requirement for LISPS as the exciting source for shock wave plasma. For this purpose a TEA CO_2 laser with a nearly-single mode oscillation and with shorter pulse duration is desirable. If such a TEA CO_2 laser is developed the analytical method presented here will be applicable to any all metal samples.

For glass samples, this LISPS method is quite successful with a promise of high sensitivity analysis. It can be expected that by combining this TEA CO_2 laser-induced plasma with a polychromator, equipment for simultaneous multi-element analysis can be constructed and rapid quantitative analysis of glass samples can be made in the $\mu g\ g^{-1}$ level.

References

[1] E.H. Piepmeier, in E.H. Piepmeier (Ed.), Analytical Application of Lasers, Wiley, New York, 1986, p. 627.
[2] K. Laqua, in N.O. Omenetto (Ed.), Analytical Laser Spectroscopy, Wiley, New York, 1979, p.47.
[3] D.A. Cremers and L.I. Radziemski, in R.W. Solarz and J.A. Poisner (Eds.), Laser Spectroscopy and Its Application, Marcel Dekker, New York, 1987, p.351.
[4] N.G. Basov, O.N. Krokhin and G.V. Skizkov, JETP Lett., 6 (1967) 168.
[5] T.P. Hughes, Plasma and Laser Light, Adam Hilger, Bristol, 1975, p. 435.
[6] K. Kagawa and S. Yokoi, Spectrochim. Acta B, 37 (1982) 789.
[7] K. Kagawa, M. Ohtani, S. Yokoi and S. Nakajima, Spectrochim. Acta B, 39 (1984) 525.
[8] K. Kagawa, S. Yanagihara and S. Yokoi, J. Spectrosc. Soc. Jpn., 34 (1985) 306.
[9] K. Kagawa, Y. Matsuda, S. Yokoi and S. Nakajima, J. Anal. At. Spectrom., 3 (1988) p.415.
[10] K. Kagawa, Y. Manda, M. Ueda and Z. Li, J. Spectrosc. Soc. Jpn., 40 (1991) 150.
[11] K. Kagawa and H. Kurniawan, in H. Honma (Ed.), Proceedings of the International Work Shop on Strong Shock Waves, Chiba University, Japan, 1992, p. 97.
[12] H. Kurniawan, T. Kobayashi, S. Nakajima and K. Kagawa, Jpn. J. Appl. Phys., 31 (1992) 1213.
[13] H. Kurniawan, T. Kobayashi and K. Kagawa, Appl. Spectrosc., 46 (1992) 581.
[14] M. Tani, H. Kurniawan, H. Ueda, H. Mizukami and K. Kagawa, Jpn. J. Appl. Phys., 32 (1993) 3838.
[15] K. Kagawa, K. Kawai, M. Tani and T. Kobayashi, Appl. Spectrosc., 48 (1994) 198.
[16] A.F. Gibson, T.P. Hughes and L.M. Ireland, Phys. D, 4 (1971) 1527.
[17] K. Kagawa, Y. Deguchi, A. Ogata, H. Kurniawan, N. Ikeda and Y. Takagi, Jpn. J. Appl. Phys., 30 (1991) 1899.
[18] S.D. Rasberry, B.F. Scribner and M. Margoshes, Appl. Opt., 6 (1967) 87.
[19] L.I. Sedov, Similarity and Dimensional Methods in Mechanics, Academic Press, New York, London, 1959, p. 213.
[20] M.J. Zucrow and J.D. Hoffman, Gas Dynamics, Wiley, Chichester, New York, 1976, p. 346.
[21] H. Kurniawan, N. Ikeda, T. Kobayashi and K. Kagawa, J. Spectrosc. Soc. Jpn., 41 (1992) 21.

ELSEVIER

Analytica Chimica Acta 299 (1995) 401–405

ANALYTICA CHIMICA ACTA

Determination of colloidal iron in water by laser-induced breakdown spectroscopy

Yoshiro Ito *, Osamu Ueki, Susumu Nakamura

Department of Mechanical Engineering, Nagaoka University of Technology, 1603-1, Kamitomioka, Nagaoka, Niigata 940-21, Japan

Received 19 October 1993; revised manuscript received 14 February 1994

Abstract

Laser-induced breakdown spectroscopy was applied to the determination of FeO(OH) in water and successfully determined the concentration of the turbid solution down to a few ppm (μg ml^{-1}). A Q-switched Nd:YAG laser, which delivered 8 ns pulses, was used as an excitation source. Cell-less measurement was achieved using a coaxial nozzle flow system which allowed to study the effect of ambient gas on emission intensity and decay lifetime of the breakdown plasma. Using helium gas and with a proper timing gate, the FeO(OH) concentration in water was determined in the ppm range.

Keywords: Laser-induced breakdown spectroscopy; Colloidal iron; Iron

1. Introduction

In a thermo-electric power plant, the control of boiler water quality is very important for the protection of turbine blades rotating at very high speed. Even a small particle suspended in the water can damage the turbine blades severely and, therefore, highly cleaned, de-ionized pure water is supplied for the boiler. Particles from pipes and valves inevitably contaminate the water, especially when the plant is started up.

The water quality is monitored by off-line chemical analysis techniques and the total amounts of iron and silica are checked. The analysis takes some tens of minutes and a very large amount of flushing water is consumed during this period. To monitor the water condition during the flushing process, an on-line measuring technique for total iron, most of which is in the form of suspended solids and/or colloids, is greatly needed.

Laser-induced breakdown spectroscopy (LIBS) would become one of these techniques for it is expected to have the following advantages.

(1) The emission intensity of an element would be independent of its chemical form if the temperature of the breakdown plasma was high enough to atomize, excite and ionize all species. No sample preparation procedure would be required.

(2) The threshold power density of laser-induced breakdown for solids is reported to be lower than that for liquids or gases. Solid suspensions in water, therefore, would cause breakdown at a power density lower than that of the threshold of water [1]. At such power density, it would be possible to induce selective breakdown and achieve selective analysis of particulate impurities.

LIBS and laser-induced plasma spectroscopy have been applied to analytical measurement of gases [2], aerosols [3], metal ions in solution [4] and a solid metal [5]. Detection limits depended on target ele-

* Corresponding author.

SSDI 0003-2670(94)00313-0

ments and ranged from some ppb (ng ml^{-1}) to hundreds of ppm (μg ml^{-1}). For suspended particulate entities, only the qualitative measurement for turbid solutions of $CaCO_3$ has been reported [6]. We tried to apply LIBS to the quantitative analysis of FeO(OH) particles in water and could determine its concentration at a few ppm.

2. Experimental

A Q-switched Nd:YAG laser which delivered 8 ns pulses of up to 900 mJ was used. The laser was operated in its fundamental wavelength (1064 nm) at 10 Hz and was focused by a quartz lens of 50 mm focal length. Pulse energy was changed between 100 to 400 mJ/pulse but in most cases it was 100 mJ/pulse. Pulse to pulse fluctuation of laser output was measured by a photodiode and found to be less than 5%. We therefore measured and adjusted the laser pulse energy to be a certain value at the beginning of a measurement and neglected the fluctuation of it afterward.

Luminescence spectra from laser-induced breakdown sparks were picked up by a single core optical fiber and were recorded by a multichannel photodetector (SMA, Princeton Inc.) mounted on a 32-cm polychromator with a grating of 1200 G/mm. A nominal wavelength resolution of the system was 1 nm. The SMA was operated in a gate mode and data were accumulated for 50 to 1000 laser pulses.

Commercially available FeO(OH) of special reagent grade was "dissolved" in de-ionized and doubly distilled water.

3. Results and discussion

In the early stage of our research, the sample solution was transferred into a rectangular quartz cell of 10 mm optical pathlength and placed at the focus of the lens. The use of such a small cell, however, proved inappropriate to laser breakdown spectroscopic measurements because bubbles formed in the cell by a preceding laser pulse interfered to the subsequent measurement at 10 Hz or even lower repetition rates. In addition, the cell's wall tended to be contaminated and the laser radiation began to be absorbed at the cell wall after a few measurements.

We employed, therefore, the coaxial nozzle configuration shown in Fig. 1. Sample solution flowed down the central nozzle at a constant flow and ambient gas flowed through the outer shroud. The stream of water was irradiated by a laser pulse and luminescence spectra were taken from the direction perpendicular to both the water flow and the laser beam. A flow rate achieved by free fall of the water was high enough to carry down the previously irradiated section so as to be outside the focal region of the subsequent laser pulses. Furthermore, the nozzle allowed us to study the effects of an ambient gas on the laser-induced breakdown plasma by changing the outer gas which formed a sheath of gas around the stream of the sample solution.

The luminescence spectrum in the near-UV region recorded for 10 ppm FeO(OH) solution is shown in Fig. 2. It was taken from 400 to 3400 ns after a laser pulse in air, i.e., recorded without outer gas flow, and accumulated for 50 pulses. The laser pulse energy was 100 mJ. We could identify atomic emissions of Fe at 260, 261, 268, 299 and 301 nm and ionic emissions around 274 nm in addition to broad and continuous emissions. These lines coincide with the values in wavelength tables of Fe emissions in arc and/or discharge analyses [7] within our spectral resolution. In addition, the same spectral lines were obtained when

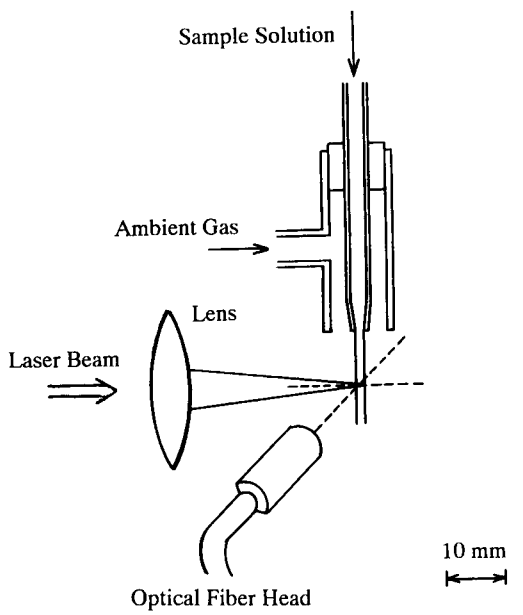

Fig. 1. Schematic drawing of a coaxial nozzle and geometry of measurement.

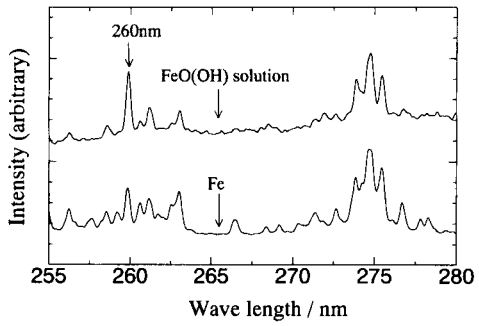

Fig. 2. Luminescence spectrum obtained for 10 ppm FeO(OH) solution (upper trace) and for bulk iron (lower trace). Both were recorded in air under irradiation of 100 mJ pulse energy and accumulated for 50 pulses.

we irradiated a bulk steel or compacted Fe powder in air with the YAG laser. The Balmer series of the H atom were also identified in the spectra observed in the longer wavelength region. Fe has some intense emission lines in the shorter wavelength region but we did not observe these lines because of absorption by the optical fiber.

To increase the intensity ratio of Fe emission lines to the background emission (S/B ratio), we examined the effect of outer gas flow. Fig. 3 shows spectra recorded under the same condition of Fig. 2 but with argon (Ar) or helium (He) gas flowing through the outer nozzle. The intensity of the emission varied with the gas: Ar gas greatly enhanced the intensity and He suppressed it. In the contrast to total emission intensity, however, the S/B ratio was largest in He, next in air and the lowest in Ar. We observed some lines assigned to the He atom in the spectra recorded with a He gas flow. Thus the breakdown plasma involves species originated from FeO(OH), water and ambient gas molecules.

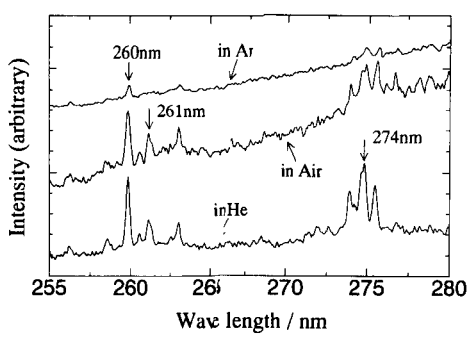

Fig. 3. Luminescence spectrun obtained for 10 ppm FeO(OH) solution with Ar gas flow (upper race), in air (middle trace) and with He gas flow (lower trace) masured under the same conditions.

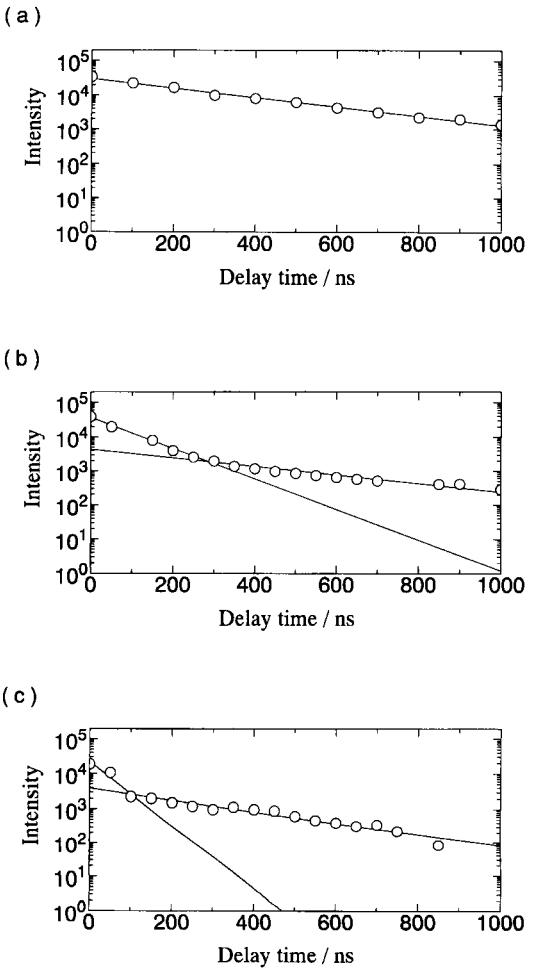

Fig. 4. Temporal change of the luminescence intensity at 260 nm: (a) with Ar gas flow, (b) in air and (c) with He gas flow.

The temporal changes of the luminescence intensity were measured in these three cases. The results are presented in Fig. 4. The SMA was operated with a 50 ns gate width and the gate delay times varied with a 50 ns interval. The spectra were accumulated for 50 shots at each delay time and the emission intensity at 260 nm, which corresponded to one of the Fe emission lines, was plotted. Temporal changes of the emission in He and in air consisted of a fast and a slow component. The lifetimes of these components were 50 ns and 240 ns in He (Fig. 4c) and 60 ns and 380 ns in air (Fig. 4b), respectively. Fig. 5 shows the emission spectrum in air recorded immediately after the laser pulse for up to 400 ns (the upper trace in Fig. 5), in which the fast component should dominate, and that recorded from

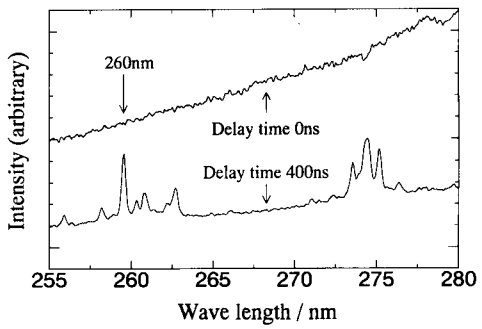

Fig. 5. Spectrum of the fast component recorded between immediately after the laser pulse to 400 ns (upper trace) and that of the slow component recorded from 400 ns after the pulse through 1900 ns (lower trace) for 100 ppm FeO(OH) in air. Laser pulse energy was 100 mJ.

400 ns through 1900 ns after the pulse (the lower trace in the Fig. 5), in which the slow component appeared. The emission lines of Fe dominated in the slow component spectrum while only a broad, futureless emission was observed in the fast component spectrum. The slow components have significantly longer lifetimes than the fast ones in both He and air and considered to be effective emission lifetimes of Fe in those gases. In Ar, however, a single component decay of 320 ns lifetime was observed (Fig. 4a). The lifetime of the background emission in Ar, which should correspond to the fast component in He and air, would happen to be nearly the same to those of slow components in He and air and thus the single component decay might be observed. In fact, the decay lifetime measured for off-line background of the spectrum in Ar was the same to that at 260 nm. Therefore, the fast components had lifetimes dependent upon atmospheric gases which varied from 50 ns in He to 320 ns in Ar.

The broad background emission caused by the fast component would be due to the black body radiation and/or the radiative recombination of the breakdown plasma. Thermal processes are considered to be responsible for evolution of the breakdown plasma [8]. It is evident that the ambient gas molecules were involved in the plasma. Thus the temperature and the lifetime of the plasma should depend on thermal properties and ionization potentials of environmental gas molecules. Molecules with a lower ionization potential would be ionized more easily and result in higher density plasma. The temperature of the plasma would be kept high for a longer period in a gas of lower thermal conductivity than in a gas of higher thermal conductivity. Both sequences of ionization potentials and thermal conductivities of gas molecules listed in Table 1 are in good agreement with our results. The fast component had the shortest lifetime in He which has the highest ionization potential and the largest thermal conductivity. It had the longest lifetime in Ar which has the lowest ionization energy and the smallest thermal conductivity. Similar effects of gas atmospheres on the emissions from a laser-induced plasma at solid metal surfaces have been reported [9] and interpreted in terms of the densities and the thermal properties of the atmospheric gases [10].

To observe the Fe emissions with a good S/B ratio, the measuring conditions were determined to be as follows: He gas environment, delay time of 400 ns, gate width of 3000 ns. The data were accumulated for 50 to 1000 pulses to get better spectra.

The Fe concentration was determined using the emission peak observed at 260 nm. This peak was reasonably separated from other lines and thus its intensity could easily be measured. The peak might consist of an atomic line at 259.96 nm and ionic lines of 259.84 and 259.94 nm, both of which were known to be strong lines in inductively coupled plasma spectrometry [11]. These lines were not separated by the present detection system partly due to broadening of the spectral line by the Stark effect expected to occur in the plasma [4].

The peak intensity was estimated by two different methods: one was a peak height from background level and another was peak area above the background level. The background level was estimated from a linear extrapolation from shorter and longer wavelength region data selected on a computer display using a program developed for this purpose. The center of the peak was determined as the zero-cross point of its first derivatives and the height was calculated. Then the peak area was calculated by the trapezoidal method.

Table 1
Thermal conductivity and ionization potential of gases

Gas	Thermal conductivity[12] (at 0°C) / 10^{-2} W m^{-1} K^{-1}	Ionization potential (eV)
Ar	1.63	15.76[13]
Air	2.41	–
N_2	2.40	15.6[14]
O_2	2.45	12[15]
He	14.22	24.59[13]

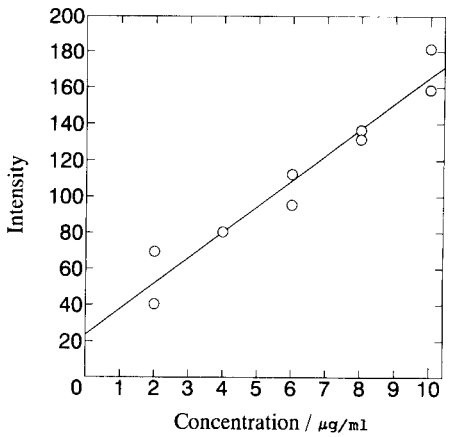

Fig. 6. Correlation of the peak height at 260 nm with FeO(OH) concentration.

Fig. 6 shows the correlation of the peak height with FeO(OH) concentration. A good linear correlation was obtained in the ppm range. The peak area data also show a similarly good correlation. The detection limit, estimated from the figure as the concentration where the signal-to-noise ratio (S/N) equals unity, is 0.6 ppm. Here N, the noise level, was estimated from the root mean square (σ) of the noise on the off-line background and was set to be 2σ. The σ value was estimated by the program. The root mean square variation of the data presented in the figure was nearly equal to, but slightly less than, the N estimated above. Thus the concentration of FeO(OH) in water in the ppm range was detectable by the LIBS measurement using the coaxial flow nozzle with helium gas and with the proper timing gate for spectral measurement.

This cell-less flow method has the following advantages for the LIBS of liquids.

(1) It is possible to control the environment of the laser-induced plasma and to increase the sensitivity by selecting an appropriate gas.

(2) Fresh sample liquid is continuously supplied to be measured and thus the on-line measurement would easily be achieved.

(3) It is free from interferences from bubbles accompanied by laser-induced breakdown.

(4) It is free from a cell or window which tends to be obscured and frequently damaged by intense laser radiations.

Acknowledgements

This work was supported by a joint research program of Tohoku Electric Power Co., Inc. and Applied Laser Engineering Research Institute (ALERI). We are grateful to K. Sone and M. Sato for their help during the experiments and for programming.

References

[1] T. Kitamori, K. Yokose, K. Suzuki, T. Sawada and Y. Gohshi, Jpn. J. Appl. Phys., 27 (1988) L983.
[2] D.A. Cremers and L.J. Radjiemski, Anal. Chem., 55 (1983) 1252.
[3] L.J. Radjiemski, T.R. Loree, D.A. Cremers and N.M. Hoffman, Anal. Chem., 55 (1983) 1246.
[4] D.A. Cremers, L.J. Radjiemski and T.R. Loree, Appl. Spectrosc., 38 (1984) 721.
[5] K. Kagawa and S. Yokoi, Spectrochim. Acta, 37B (1982) 789.
[6] T. Kitamori, T. Matsui, M. Sakagami and T. Sawada, Chem. Lett., (1989) 2205.
[7] S. Murayama and T. Takahashi (Eds.), Purazuma Hakkouhou (Plasma Emission Method for Analysis of Solid Samples), Gakkai Shuppan Center, Tokyo, 1982 (in Japanese).
[8] D.C. Smith, J. Appl. Phys., 48 (1977) 2217.
[9] M. Kuzuya, H. Matsumoto, H. Takechi and O. Mikami, J. Spectrosc. Soc. Jpn., 41 (1992) 327; and references cited therein.
[10] Y. Iida, Spectrochim. Acta, 45B (1990) 1353.
[11] T. Takahashi and S. Murayama (Eds.), Ekitai Shiryouno Hakkoubunseki (Emission Spectroscopic Analysis of Liquid Samples), Gakkai Shuppan Center, Tokyo, 1983 (in Japanese).
[12] Tokyo Astronomical Observatory, Chronological Scientific Tables, Maruzen, Tokyo, 1985, p. 474.
[13] Tokyo Astronomical Observatory, Chronological Scientific Tables, Maruzen, Tokyo, 1985, p. 534.
[14] J.H.D. Eland, Photoelectron Spectroscopy, 2nd edn., Butterworths, London, 1984, p. 8.
[15] J.H.D. Eland, Photoelectron Spectroscopy, 2nd edn., Butterworths, London, 1984, p. 11.

ELSEVIER

Analytica Chimica Acta 299 (1995) 407–410

ANALYTICA CHIMICA ACTA

Author Index

PUBLICATION SCHEDULE FOR 1995

	O'94	N'94	D'94	J	F	M	A	M	J	J	A	S
Anal. Chim. Acta	296/2 296/3 297/1–2	297/3 298/1 298/2	298/3 299/1 299/2	299/3 300/1–3 301/1–3	302/1 302/2–3 303/1							
Vib. Spec.		8/1		8/2		8/3		9/1		9/2		9/3

INFORMATION FOR AUTHORS

Detailed "Instructions to Authors" for *Analytica Chimica Acta* was published in Volume 289, No. 3, pp. 381–384. Free reprints of the "Instructions to Authors" of *Analytica Chimica Acta* and *Vibrational Spectroscopy* are available from the Editors or from: Elsevier Science B.V., P.O. Box 330, 1000 AH Amsterdam, The Netherlands. Telefax: (+31-20) 4852 459.

Manuscripts. The language of the journal is English. English linguistic improvement is provided as part of the normal editorial processing. Authors should submit three copies of the manuscript in clear double-spaced typing on one side of the paper only. *Vibrational Spectroscopy* also accepts papers in English only.

Rapid publication letters. *Letters* are short papers that describe innovative research. Criteria for letters are novelty, quality, significance, urgency and brevity. Submission data: max. of 2 printed pages (incl. Figs., Tables, Abstr., Refs.); short abstract (e.g., 3 lines); *no* proofs will be sent to the authors; submission on floppy disc; *no* revision will be possible.

Abstract. All papers, reviews and letters begin with an Abstract (50–250 words) which should comprise a factual account of the contents of the paper, with emphasis on new information.

Figures. Figures should be suitable for direct reproduction and as rich in contrast as possible. One original (or sharp glossy print) and two photostat (or other) copies are required. Attention should be given to line thickness, lettering (which should be kept to a minimum) and spacing on axes of graphs, to ensure suitability for reduction in size on printing. Axes of a graph should be clearly labelled, along the axes, outside the graph itself.

All figures should be numbered with Arabic numerals, and require descriptive legends which should be typed on a separate sheet of paper. Simple straight-line graphs are not acceptable, because they can readily be described in the text by means of an equation or a sentence. Claims of linearity should be supported by regression data that include slope, intercept, standard deviations of the slope and intercept, standard error and the number of data points; correlation coefficients are optional.

Photographs should be glossy prints and be as rich in contrast as possible; colour photographs cannot be accepted. Line diagrams are generally preferred to photographs of equipment. Computer outputs for reproduction as figures must be good quality on blank paper, and should preferably be submitted as glossy prints.

Nomenclature, abbreviations and symbols. In general, the recommendations of IUPAC should be followed, and attention should be given to the recommendations of the Analytical Chemistry Division in the journal *Pure and Applied Chemistry* (see also *IUPAC Compendium of Analytical Nomenclature, Definitive Rules*, 1987).

References. The references should be collected at the end of the paper, numbered in the order of their appearance in the text (*not* alphabetically) and typed on a separate sheet.

Reprints. Fifty reprints will be supplied free of charge. Additional reprints (minimum 100) can be ordered. An order form containing price quotations will be sent to the authors together with the proofs of their article.

Papers dealing with vibrational spectroscopy should be sent to: Dr J.G. Grasselli, 150 Greentree Road, Chagrin Falls, OH 44022, U.S.A. Telefax: (+1-216) 2473360 (Americas, Canada, Australia and New Zealand) or Dr J.H. van der Maas, Department of Analytical Molecular Spectrometry, Faculty of Chemistry, University of Utrecht, P.O. Box 80083, 3508 TB Utrecht, The Netherlands. Telefax: (+31-30) 518219 (all other countries).

0003-2670/95/$09.50